ornl

OAK RIDGE NATIONAL LABORATORY

UNION CARBIDE

NUREG/CR-2751
Volume 1
ORNL/TM-8369/V1

Heavy-Section Steel Technology Program Quarterly Progress Report for January–March 1982

G. D. Whitman R. H. Bryan

Prepared for the U.S. Nuclear Regulatory Commission
Office of Nuclear Regulatory Research
Under Interagency Agreements DOE 40-551-75 and 40-552-75

OPERATED BY
UNION CARBIDE CORPORATION
FOR THE UNITED STATES

Printed in the United States of America. Available from
National Technical Information Service
U.S. Department of Commerce
5285 Port Royal Road, Springfield, Virginia 22161

Available from
GPO Sales Program
Division of Technical Information and Document Control
U.S. Nuclear Regulatory Commission
Washington, D.C. 20555

NUREG/CR-2751
Volume 1
ORNL/TM-8369/V1
Dist. Category RF

Contract No. W-7405-eng-26

Engineering Technology Division

HEAVY-SECTION STEEL TECHNOLOGY PROGRAM QUARTERLY PROGRESS REPORT FOR JANUARY-MARCH 1982

G. D. Whitman R. H. Bryan

Manuscript Completed - July 12, 1982
Date Published - August 1982

Prepared for the
U.S. Nuclear Regulatory Commission
Office of Nuclear Regulatory Research
Under Interagency Agreements DOE 40-551-75 and 40-552-75

NRC FIN No. B0119

Prepared by the
OAK RIDGE NATIONAL LABORATORY
Oak Ridge, Tennessee 37830
operated by
UNION CARBIDE CORPORATION
for the
DEPARTMENT OF ENERGY

CONTENTS

PREFACE

The Heavy-Section Steel Technology (HSST) Program, which is sponsored by the Nuclear Regulatory Commission, is an engineering research activity devoted to extending and developing the technology for assessing the margin of safety against fracture of the thick-walled steel pressure vessels used in light-water-cooled nuclear power reactors. The program is being carried out in close cooperation with the nuclear power industry. This report covers HSST work performed in January–March 1982. The work performed by Oak Ridge National Laboratory (ORNL) and by subcontractors is managed by the Engineering Technology Division. Major tasks at ORNL are carried out by the Engineering Technology Division and the Metals and Ceramics Division. Prior progress reports on this program are ORNL-4176, ORNL-4315, ORNL-4377, ORNL-4463, ORNL-4512, ORNL-4590, ORNL-4653, ORNL-4681, ORNL-4764, ORNL-4816, ORNL-4855, ORNL-4918, ORNL-4971, ORNL/TM-4655 (Vol. II), ORNL/TM-4729 (Vol. II), ORNL/TM-4805 (Vol. II), ORNL/TM-4914 (Vol. II), ORNL/TM-5021 (Vol. II), ORNL/TM-5170, ORNL/NUREG/[illegible]3, ORNL/NUREG/TM-28, ORNL/NUREG/TM-49, ORNL/NUREG/TM-64, ORNL/NUREG/TM-94, ORNL/NUREG/TM-120, ORNL/NUREG/TM-147, ORNL/NUREG/TM-166, ORNL/NUREG/TM-194, ORNL/NUREG/TM-209, ORNL/NUREG/TM-239, NUREG/CR-0476 (ORNL/NUREG/TM-275), NUREG/CR-0656 (ORNL/NUREG/TM-298), NUREG/CR-0818 (ORNL/NUREG/TM-324), NUREG/CR-0980 (ORNL/NUREG/TM-347), NUREG/CR-1197 (ORNL/NUREG/TM-370), NUREG/CR-1305 (ORNL/NUREG/TM-380), NUREG/CR-1477 (ORNL/NUREG/TM-393), NUREG/CR-1627 (ORNL/NUREG/TM-401), NUREG/CR-1806 (ORNL/NUREG/TM-419), NUREG/CR-1941 (ORNL/NUREG/TM-437), NUREG/CR-2141/Vol. 1 (ORNL/TM-7822), NUREG/CR-2141, Vol. 2 (ORNL/TM-7955), NUREG/CR-2141, Vol. 3 (ORNL/TM-8145), and NUREG/CR-2141, Vol. 4 (ORNL/TM-8252).

SUMMARY

1. PROGRAM ADMINISTRATION AND PROCUREMENT

The Heavy-Section Steel Technology (HSST) Program is an engineering research activity conducted by the Oak Ridge National Laboratory (ORNL) for the Nuclear Regulatory Commission in coordination with other research sponsored by the federal government and private organizations. The program comprises studies related to all areas of the technology of materials fabricated into thick-section primary-coolant containment systems of light-water-cooled nuclear power reactors. The principal area of investigation is the behavior and structural integrity of steel pressure vessels containing crack-like flaws. Current work is organized into the following tasks: (1) program administration and procurement, (2) fracture mechanics analyses and investigations, (3) investigations of irradiated materials, (4) thermal-shock investigations, (5) pressure vessel investigations, and (6) stainless steel cladding investigations.

The work performed under the existing research and development subcontracts is included in this report.

During the quarter, 18 program briefings, reviews, or presentations were made.

2. FRACTURE MECHANICS ANALYSES AND INVESTIGATIONS

A deformation plasticity material model was implemented into the ADINA-ORVIRT system, a set of programs using finite-element methods to calculate J_I for cylinders under combined thermal and mechanical loads. This system attained excellent agreement with the known solution of a nonlinear problem and has also been applied to a cylindrical vessel.

Battelle Columbus Laboratories in its HSST support program performed posttest analyses of thermal-shock experiment TSE-6, investigated the effect of crack-tip morphology on K_{Ic}, and continued work on developing a standard procedure for crack-arrest toughness testing.

3. INVESTIGATION OF IRRADIATED MATERIALS

In the Fourth HSST Irradiation Series, the irradiation of the third capsule was completed, and the capsule was disassembled. Preliminary test matrices were prepared, and a 110-kip MTS testing machine was installed in a hot cell.

Plans are being made to measure the irradiation-induced shift of K_{Ic} of nuclear pressure vessel steels. Also, a study of the effects of irradiation on the fracture toughness of stainless steel cladding was initiated. Specimens are being prepared.

4. THERMAL-SHOCK INVESTIGATIONS

A comparison was made of toughness data obtained for thermal-shock experiments TSE-5, -5A, and -6 with ASME Section XI toughness curves, indicating that the curves are conservative. Preliminary calculations for experiment TSE-8 were made. A parametric analysis of overcooling accidents was completed. The OCA-I code was modified to include effects of cladding. Investigation of effects of azimuthal variations in temperature on K_I was initiated. Toughness characterization of material from the cylinder used in experiment TSE-6 was completed.

5. PRESSURE VESSEL INVESTIGATIONS

Preparations for testing intermediate test vessel V-8A are continuing. In this test, the fracture behavior of low-upper-shelf weld metal will be observed, and the application of theories of elastic-plastic fracture mechanics will be investigated. During the quarter the vessel was flawed, and installation of instrumentation was initiated. Elastic-plastic fracture and stress analyses were performed for determining the flaw size.

Studies of pressurized-thermal-shock tests of thick-walled vessels and final design of a test facility continued. Additional thermal-hydraulic analysis of the test tank, which must function both as the preheater and as a coolant shroud, resulted in modifying dimensional details and confirming the necessity of stringent dimensional tolerances.

The test cells to be used for the V-8A test and pressurized-thermal-shock tests were reevaluated with respect to safety for higher test temperatures than those for which the cells were originally designed. They were determined to be adequate to withstand the potential missiles and pressures generated in the tests.

6. STAINLESS STEEL CLADDING INVESTIGATIONS

Equipment for testing bare and clad plates with flaws in pure bending was prepared. Stainless steel weld wire was procured, welding procedures were developed, and several specimens were fabricated.

HEAVY-SECTION STEEL TECHNOLOGY PROGRAM QUARTERLY PROGRESS REPORT FOR JANUARY–MARCH 1982*

G. D. Whitman   R. H. Bryan

ABSTRACT

The Heavy-Section Steel Technology Program is an engineering research activity conducted by the Oak Ridge National Laboratory for the Nuclear Regulatory Commission. The program comprises studies related to all areas of the technology of materials fabricated into thick-section primary-coolant containment systems of light-water-cooled nuclear power reactors. The investigation focuses on the behavior and structural integrity of steel pressure vessels containing crack-like flaws. Current work is organized into six tasks: (1) program administration and procurement, (2) fracture mechanics analyses and investigations, (3) investigations of irradiated materials, (4) thermal-shock investigations, (5) pressure vessel investigations, and (6) stainless steel cladding investigations.

The three-dimensional finite-element program for elastic-plastic fracture mechanics was used with a deformation plasticity model on test vessel analysis. Subcontractors analyzed the last thermal-shock experiment and continued development of a standard procedure for crack-arrest toughness testing and investigation of transition from cleavage to fibrous fracture. Work progressed toward initial testing of specimens in the Fourth HSST Irradiation Series. Parametric analysis of overcooling accidents was completed, and improvements to the OCA-I code were made. Intermediate test vessel V-8A was flawed and is in preparation for testing. A major part of the design of a pressurized-thermal-shock test facility was completed. Test equipment and specimens were prepared for clad plate fracture tests.

1. PROGRAM ADMINISTRATION AND PROCUREMENT

G. D. Whitman

The Heavy-Section Steel Technology (HSST) Program, a major safety program sponsored by the Nuclear Regulatory Commission (NRC) at the Oak Ridge National Laboratory (ORNL), is concerned with the structural integrity of the primary systems [particularly the reactor pressure vessels (RPVs)] of light-water-cooled nuclear power reactors. The structural integrity of these vessels is ensured by (1) designing and fabricating them

---

*Conversions from SI to English units for all SI quantities are listed on a foldout page at the end of this report.

according to standards set by the code for nuclear pressure vessels, (2) detecting flaws of significant size that occur during fabrication and in service, and (3) developing methods of producing quantitative estimates of conditions under which fracture could occur. The program is concerned mainly with developing pertinent fracture technology, including knowledge of (1) the material used in these thick-walled vessels, (2) the flaw growth rate, and (3) the combination of flaw size and load that would cause fracture and thus limit the life and/or operating conditions of this type of reactor plant.

The program is coordinated with other government agencies and with the manufacturing and utility sectors of the nuclear power industry in the United States and abroad. The overall objective is a quantification of safety assessments for regulatory agencies, for professional code-writing bodies, and for the nuclear power industry. Several activities are conducted under subcontracts by research facilities in the United States and through informal cooperative effort on an international basis. Two research and development subcontracts are currently in force.

Administratively, the program is organized into six tasks, as reflected in this report: (1) program administration and procurement, (2) fracture mechanics (FM) analyses and investigations, (3) investigations of irradiated material, (4) thermal-shock investigations, (5) pressure vessel investigations, and (6) stainless steel cladding investigations.

During this quarter, 18 program briefings, reviews, or presentations were made by the HSST staff at technical meetings and at program reviews for the NRC staff or visitors.

2. FRACTURE MECHANICS ANALYSES AND INVESTIGATIONS

2.1 Computational Methods for 3-D Nonlinear Fracture Mechanics

B. R. Bass* R. H. Bryan
J. W. Bryson J. G. Merkle

2.1.1 Introduction

In the previous report period,[1] a thermal loading capability was introduced into both ORJINT-2D and ORVIRT-3D and two thermoelastic applications were presented. This quarter's work focused on implementing[2] a deformation plasticity material model into the ADINA-ORVIRT system. The resulting thermomechanical formulation is strictly valid for hyperelastic materials where unloading and severe departure from proportional loading are restricted to a small region of the structure. The deformation plasticity approach has distinct advantages over the more common incremental flow theory, namely, computational economy and numerical stability.

A brief discussion of the deformation plasticity approach is given in the next section. This is followed by a nonlinear validation problem (thick-walled cylinder under internal pressure) for which excellent agreement is obtained with a known solution. A recent nonlinear application of the ADINA-ORVIRT system to the analysis of a part-through crack in intermediate test vessel (ITV) V-8A is described in Sect. 5.1.

2.1.2 Deformation plasticity material model

In incremental plasticity theory, the Prandtl-Reuss relations[3]

$$d\varepsilon_{\alpha\beta}^{p} = \frac{3}{2} \frac{S_{\alpha\beta}}{\sigma_e} d\varepsilon_p , \tag{1}$$

$$S_{\alpha\beta} = \sigma_{\alpha\beta} - \frac{1}{3} \sigma_{\gamma\gamma} \delta_{\alpha\beta} , \tag{2}$$

and

$$\sigma_e^2 = \frac{3}{2} S_{\alpha\beta} S_{\alpha\beta} , \tag{3}$$

---

*Computer Sciences Division, Union Carbide Corporation-Nuclear Division (UCC-ND).

represent the flow rule associated with the von Mises yield condition. Here, $S_{\alpha\beta}$ are the deviatoric components of the stress tensor, σ_e is the effective stress, $d\varepsilon^p_{\alpha\beta}$ is the plastic strain increment, and $d\varepsilon_p$ is the increment in effective plastic strain,

$$d\varepsilon_p = \left(\frac{2}{3}\, d\varepsilon^p_{\alpha\beta}\, d\varepsilon^p_{\alpha\beta}\right)^{1/2} .$$

The total plastic strain components $\varepsilon^p_{\alpha\beta}$ are determined by integrating these equations over the entire loading path. Deformation plasticity theory is based on the proposal of Hencky[4] that the total strain components are related to the current stresses, implying that Eq. (1) can be replaced with

$$\varepsilon^p_{\alpha\beta} = \frac{3}{2}\, S_{\alpha\beta}\, \frac{\varepsilon_p}{\sigma_e} . \tag{4}$$

Thus, the plastic strains are independent of the loading history in deformation theory. It can be shown[3] that for the case of radial or proportional loading in which all stresses increase in the same ratio, incremental theory and deformation theory give identical results.

In deformation theory, the total mechanical strains can be written as the sum of the elastic and plastic contributions,

$$\varepsilon_{\alpha\beta} = \frac{1+\nu}{E}\, S_{\alpha\beta} + \frac{1-2\nu}{3E}\, \sigma_{\gamma\gamma}\, \delta_{\alpha\beta} + \frac{3}{2}\, \frac{S_{\alpha\beta}}{\sigma_e}\, \varepsilon_p . \tag{5}$$

The deviatoric strain $e_{\alpha\beta}$ and the effective strain e_e, given by

$$e_{\alpha\beta} = \varepsilon_{\alpha\beta} - \frac{1}{3}\, \varepsilon_{\gamma\gamma}\, \delta_{\alpha\beta} , \tag{6}$$

and

$$e_e^2 = \frac{2}{3}\, e_{\alpha\beta}\, e_{\alpha\beta} , \tag{7}$$

can be combined with Eq. (5) to obtain the scalar relation

$$e_e = \frac{2}{3}\left(\frac{1+\nu}{E}\right)\sigma_e + \varepsilon_p . \tag{8}$$

In addition, Eqs. (2) and (3) and (5)–(8) can be manipulated to give

$$\sigma_{\alpha\beta} = \frac{E}{1+\nu} e_{\alpha\beta} + \frac{E}{3\,(1-2\nu)} \varepsilon_{\gamma\gamma}\,\delta_{\alpha\beta} - \left(\frac{E}{1+\nu} - \frac{2}{3}\frac{\sigma_e}{e_e}\right) e_{\alpha\beta} \,, \qquad (9)$$

where the last term on the right side of Eq. (9) represents the plastic strain contribution. When Eqs. (8) and (9) are combined with an effective stress-effective plastic strain curve, the stress components are determined uniquely from the strain components.

In applications, the relation between σ_e and ε_p is usually taken from a uniaxial tensile stress–plastic strain curve. The slope of the curve is given by $H = d\sigma_e/d\varepsilon_p$. For a bilinear stress-strain curve, the constant slope H can be determined from the uniaxial relation

$$\begin{aligned} \varepsilon &= \frac{\sigma}{E} + \varepsilon_p \\ &= \frac{\sigma}{E} + \frac{(\sigma - \sigma_y)}{H} \,, \end{aligned} \qquad (10)$$

where (σ, ε) is a point on the strain-hardening curve. When the relation

$$\varepsilon_p = \frac{(\sigma_e - \sigma_y)}{H} \qquad (11)$$

is combined with Eq. (8), the effective stress σ_e is determined from the effective strain e_e. The calculation is generalized in a straightforward manner to accommodate a multilinear stress-strain relation.

2.1.3 Thick-walled cylinder under internal pressure

One of the more accessible plasticity problems is the thick-walled cylinder under internal pressure. Reference 5 gives a quantitative comparison of flow and deformation theories of plasticity for an elastic perfectly plastic analysis of a thick-walled cylinder having $b/a = 2$, $\nu = 0.3$, $k/G = 0.003$, where b is outside radius, a is inside radius, ν is Poisson's ratio, k is yield stress in pure shear, and G is modulus of rigidity.

This thick-walled cylinder was analyzed with the ADINA-ORVIRT system using the newly implemented deformation plasticity material model. A Ramberg-Osgood power law was used to represent the stress-strain behavior, $\varepsilon/\varepsilon_o = \sigma/\sigma_o + \alpha(\sigma/\sigma_o)^n$. Figure 2.1 compares a load vs outside surface displacement curve for the ADINA-ORVIRT analysis (present study) with curve A from Ref. 5. Curve A represents a Prandtl-Reuss flow rule and a

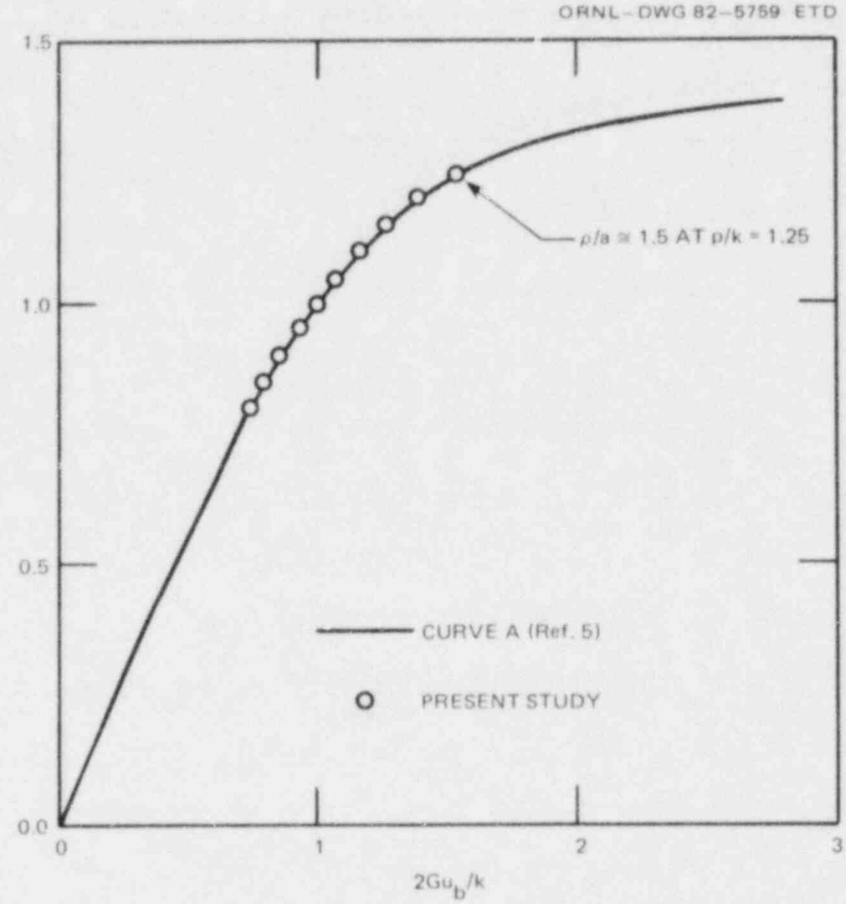

Fig. 2.1. Load vs outside surface displacement (u_b) for elastic-perfectly plastic analyses of thick-walled cylinder under internal pressure.

von Mises yield condition. Both analyses assume zero axial strain (ε_z = 0).

Figures 2.2–2.4 show comparisons between the flow theory (curve A) and the ADINA-ORVIRT deformation plasticity theory for each of the three stress components. The loading ($P/k = 1.25$) is such that the elastic-plastic boundary is at the midthickness of the cylinder, that is, $\rho/a = 1.5$ where $r = \rho$ is the elastic-plastic boundary. It can be seen that excellent agreement is obtained between the two theories.

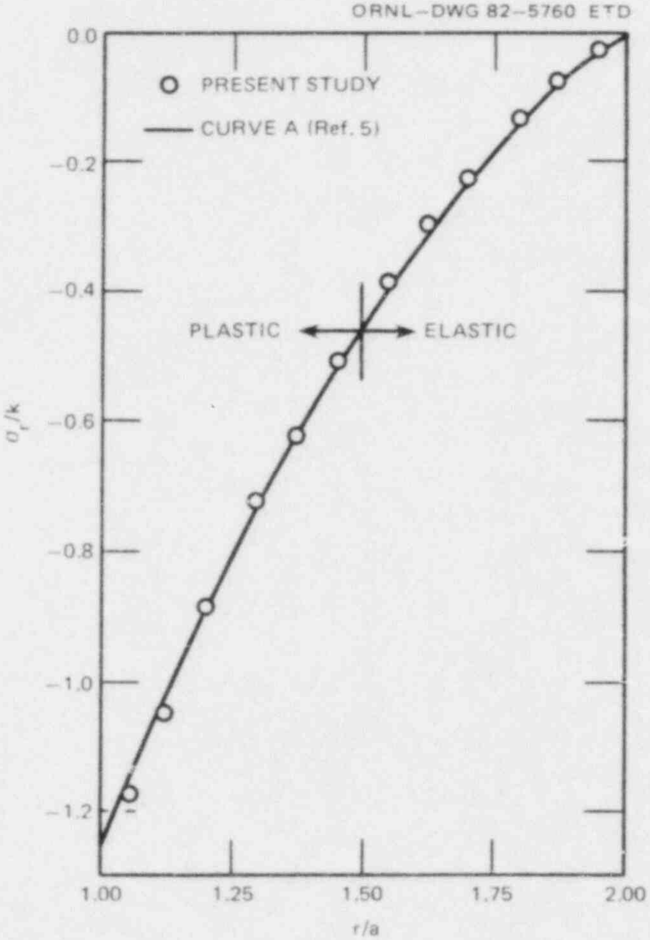

Fig. 2.2. Radial stress distribution in thick-walled cylinder for $\rho/a = 1.5$, where $r = \rho$ is the elastic-plastic boundary.

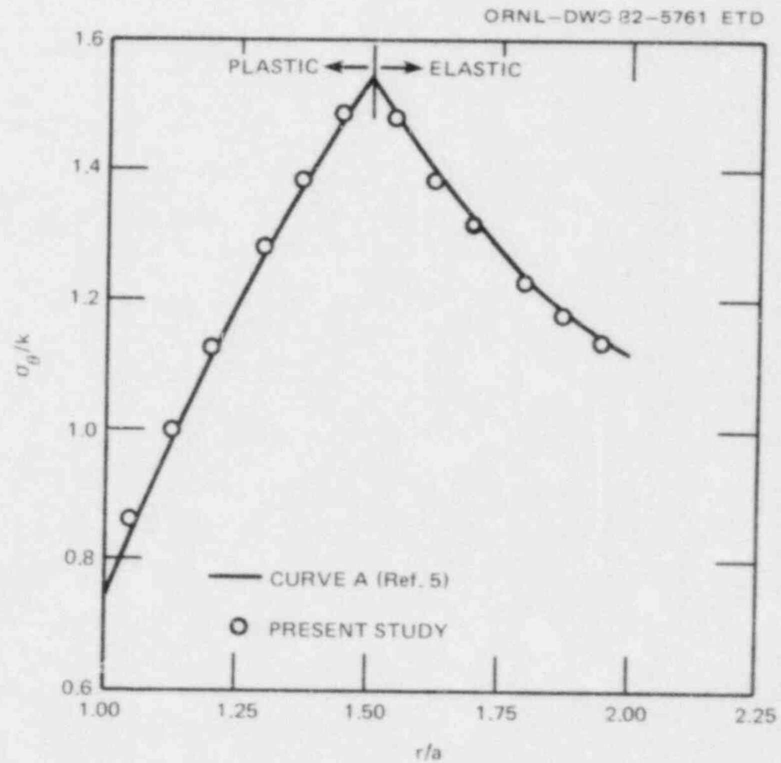

Fig. 2.3. Circumferential stress distribution in thick-walled cylinder for $\rho/a = 1.5$, where $r = \rho$ is the elasticplastic boundary.

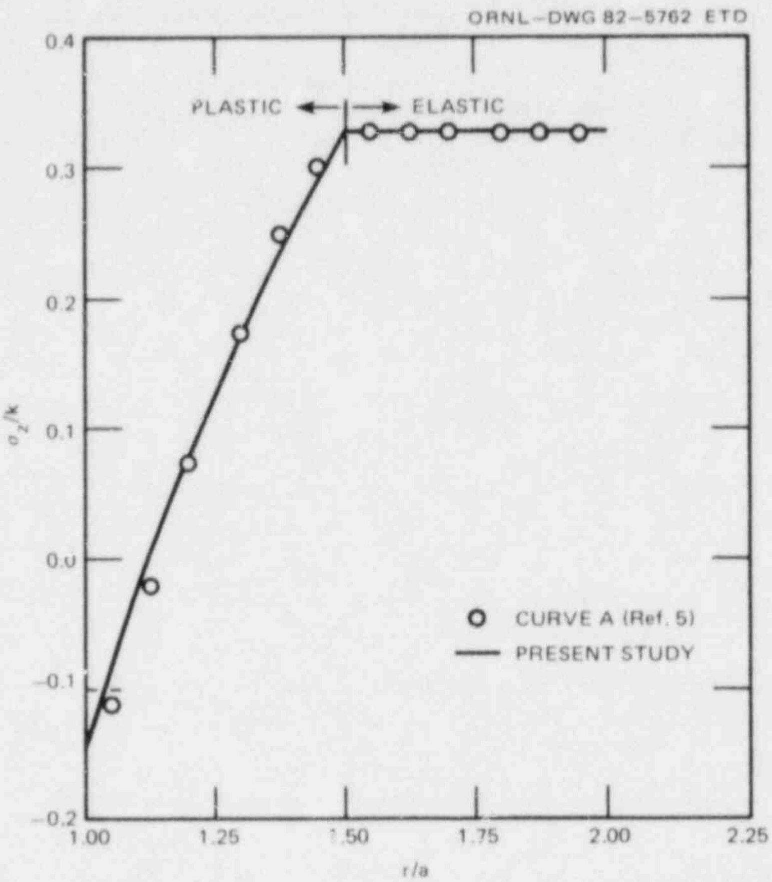

Fig. 2.4. Axial stress distribution in thick-walled cylinder for $\rho/a = 1.5$, where $r = \rho$ is the elastic-plastic boundary.

2.2 BCL HSST Support Program*

A. R. Rosenfield† C. W. Marschall†
D. K. Shetty† P. N. Mincer†
V. Papaspyropoulus†

2.2.1 Task 1: Administration – introduction and summary

The objective of the Battelle-Columbus Laboratory (BCL) HSST Support Program is to provide analytical and experimental research relevant to the fracture of steel cylinders subject to thermal shock. Particular attention is focused on analyzing crack initiation, propagation, and arrest using appropriate material-property data. The program consists of three

*Work sponsored by HSST Program under UCC-ND Subcontract 85B-13876C between UCC-ND and BCL.

†Battelle-Columbus Laboratories, Columbus, Ohio.

research tasks:

Task 2: Thermal-Shock-Project Support
Task 3: Crack Initiation
Task 4: Crack Arrest.

The research on Task 2 consisted mainly of posttest analysis of ORNL Experiment TSE-6. The lower limits of the BCL crack-initiation data approached both the cylinder data and the ASME Section XI curve, particularly when the available-energy method was used to analyze the results. However, the rapid-loading K_{Ic} values did not seem to reduce the data scatter for K_{Ic}, based on the limited number of experiments that were performed. Fractographic analysis suggested that the reason was that cleavage initiation was controlled by widely dispersed weak spots and that the scatter reflected this material inhomogeneity. In contrast to crack initiation, the crack-arrest data of TSE-6 were well described by the statistical analysis of the temperature dependence of K_a reported previously. The proper value of K_{ID} also is not clear. Dynamic analysis of TSE-6 underpredicted the arrest length of jump 1, indicating the use of too large a toughness value. However, it was not possible to model this jump perfectly because of uncertainties in the material data and in the residual stresses at the origin location in the TSE-6 cylinder. These latter effects may have dominated.

Specimen preparation was completed for Task 3, in which the effect of crack-tip morphology on K_{Ic} will be investigated. Specifically, crack-arrest specimens have been machined from the steel used in TSE-5A. These specimens will be wedge loaded to provide arrested cracks that subsequently will be reinitiated using suitable gaging.

Task 4 involves crack-arrest-test-procedure development and standardization. Size-effect studies were carried out on specimens of TSE-5A tested at 0°C. The minimum-size criteria suggested in the last quarterly report were verified. In addition, preliminary experiments were carried out on miniature specimens (50.8 x 50.8 x 12.7 mm) that have about the face dimension of a 1T compact specimen and are one-half as thick. Values of K_a obtained for these specimens were slightly low compared with the values obtained for the larger specimens. It is suggested that this behavior is associated with the unbroken ligaments that often are observed on the fracture surfaces of crack-arrest specimens.

2.2.2 Task 2: Thermal-shock experiments

The objective of Task 2 is to provide material-property data and analysis of the ORNL thermal-shock experiments. The crack-initiation and crack-arrest data for TSE-6 that were obtained at BCL were reported prior to the ORNL experiment.[6,7] This report compares the BCL and ORNL results and describes some additional K_c data obtained at high loading rates. In addition, the Charpy V-notch impact data for this steel were reevaluated in light of additional measurements at ORNL, and the 30-ft·lb (41.5-J) temperature was revised to 40°C.

<u>Crack initiation</u>. Side-grooved 1T compact specimens were loaded to unstable failure by cleavage. The total energy under the load/displacement curve at maximum load was measured and converted to a K_c value using the J-integral method. A second value of K_c was obtained by the available-energy method,[8,9] in which an elastic value of K_c is calculated from the load and crack length at the point of conversion from ductile (dimpled) rupture to cleavage. Both of these methods attempt to obtain lower-bound-toughness estimates for specimens in which lower-bound behavior is not observed. In turn, lower-bound behavior in the transition region may be defined as cleavage failure occurring without any stable crack growth via the dimpled-rupture mechanism.

Preliminary rapid-load crack-initiation data were obtained by using an MTS tensile machine loaded at the highest rate obtainable. Loading times to failure were about 1.5 ms. Displacements in this series of experiments were measured using a linear variable differential transformer (LVDT) attached to the loading pins.

The results are given in Figs. 2.5 and 2.6 and in Table 2.1. The figures compare the BCL compact-specimen data with both the ORNL compact-specimen data and with the cylinder result of TSE-6 (Ref. 10). Figure 2.5 contains the maximum-load crack-initiation toughness K_J. A considerable

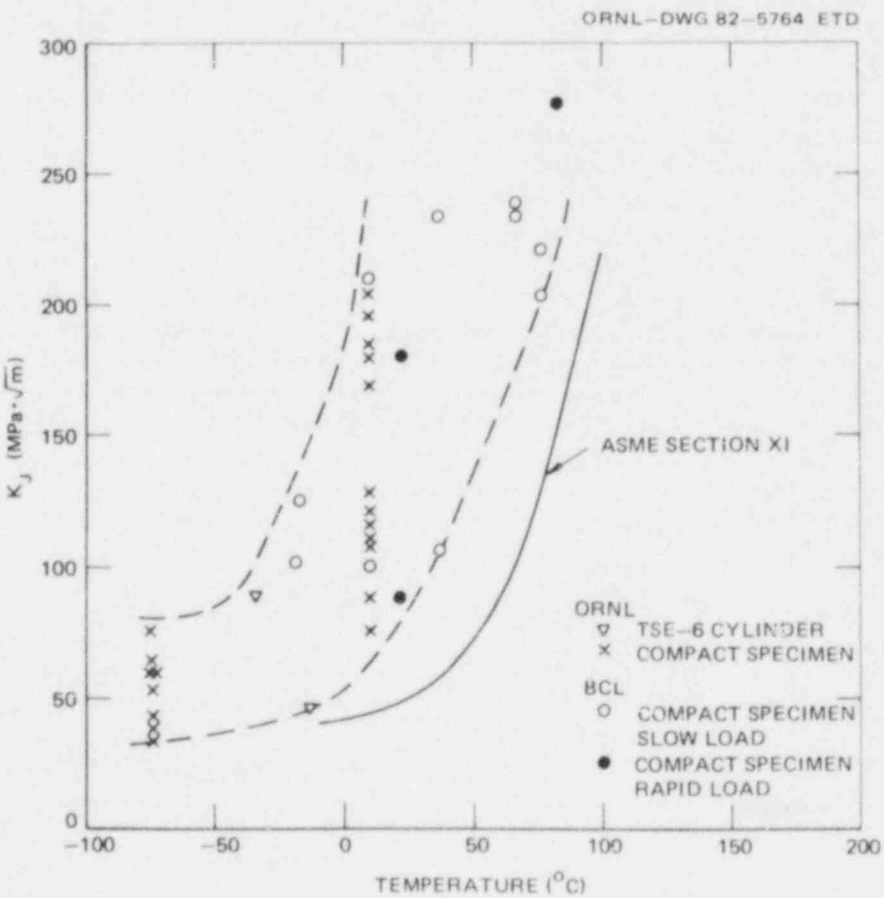

Fig. 2.5. Effect of temperature on crack initiation for TSE-6.

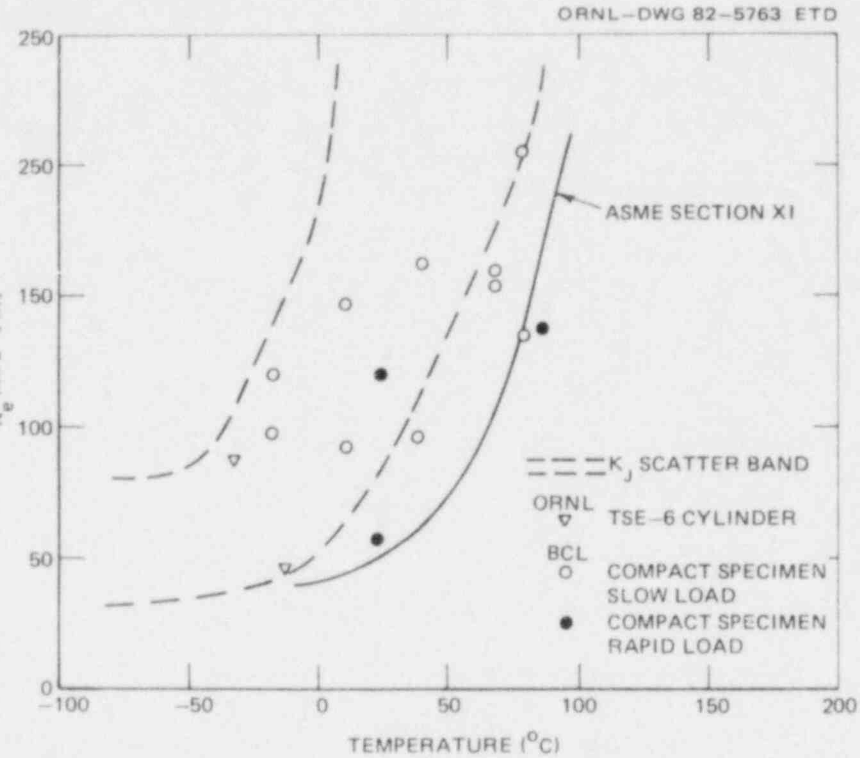

Fig. 2.6. Effect of temperature on crack initiation for TSE-6 steel.

amount of scatter is noted, with the upper and lower limits forming a band 65 to 85°C wide. Even though one of the cylinder results (jump 1) helps to define the lower limit, this value may be unusually low because of residual-stress effects.[10] The other jump, which initiated at a lower temperature, is much closer to the corresponding BCL data point. It is also noted that the BCL slow-loading points at 10°C lie within the range of ORNL data. The ASME Section XI lower bound also is indicated in Fig. 2.5. With the exception of the aforementioned jump 1, the curve appears to be conservative.

There is a tendency for the high-rate tests to result in less stable-crack growth, but, because of the scatter, it is not clear that a definite conclusion can be reached on this point yet. It is clear from Fig. 2.5 that the initial rapid-loading results were only partially successful in finding a lower bound for K_J.

The available-energy data, denoted K_e, are given in Fig. 2.6. Table 2.1 shows that for about one-half of the specimens, $K_e \approx K_J$, whereas for all but one of the rest, $K_e \approx 2/3\ K_J$. For the other specimen, tested under high-temperature rapid-load conditions, $K_e \approx 1/2\ K_J$. As a result, the major effect of adopting the available-energy technique is to shift a number of experimental points below the K_J scatter band of Fig. 2.5. In particular, the smaller rapid-loading value at 22°C has been shifted downward by 31 MPa$\cdot\sqrt{m}$ so that it is now comparable with the very low initation

Table 2.1. Crack-initiation data for steel from TSE-6

Specimen No.	Temperature (°C)	Loading rate (mm/s)	Stable-crack growth (mm)	K_c (MPa·$\sqrt{m}$)	
				Maximum-load energy	Available energy
60R-84-2	−18	0.085	0.0	125	120
60R-86-2	−18	0.085	0.0	100	99
60R-83-1	10	0.085	0.22	209	145
60R-83-2	10	0.085	0.0	99	92
60R-90-2	22	760	0.0	180	120
60R-86-1	22	760	0.0	86	55
60R-80-1	38	0.085	1.65	231	162
60R-80-2	37	0.085	0.0	106	94
60R-81-1	66	0.085	2.26	231	159
60R-81-2	66	0.085	1.60	237	154
60R-82-1	79	0.085	15.44	220	202
60R-82-2	79	0.085	0.26	201	135
60R-90-1	83	760	0.04	276	139

K_I value for jump 1 in TSE-6. Since, as stated previously, the jump 1 value may be nonrepresentative, this result may be fortuitous. The jump 2 agreement was not improved by using the available-energy method. However, when the available-energy technique is used, the Section XI curve appears to be a lower bound, although the data are insufficient to make a definite conclusion.

Fractographic examinations. The two rapidly loaded K_{IC} test specimens, 60R-90-2 and 60R-86-1, were studied fractographically. These specimens were selected for fractographic examinations because they exhibited widely differing fracture-toughness values, even though they were tested under indentical conditions and stable-crack growth prior to unstable-cleavage fracture was nearly zero in both the specimens.

The macroscopic features of the fracture surfaces of the two specimens are shown in the optical fractographs of Figs. 2.7(a and b). Specimen 60R-90-2, which had a higher K_J value (K_J = 180 MPa·$\sqrt{m}$), exhibited a rough and uneven fracture surface with significant tearing associated with the junctions of the cleavage surfaces. In contrast, Specimen 60R-86-1, which exhibited a low K_J value (K_J = 86 MPa·$\sqrt{m}$), had a very flat and even cleavage-fracture surface. The fracture surface of each specimen was examined in detail in a scanning electron microscope (SEM). The objective

ORNL–PHOTO 1902–82

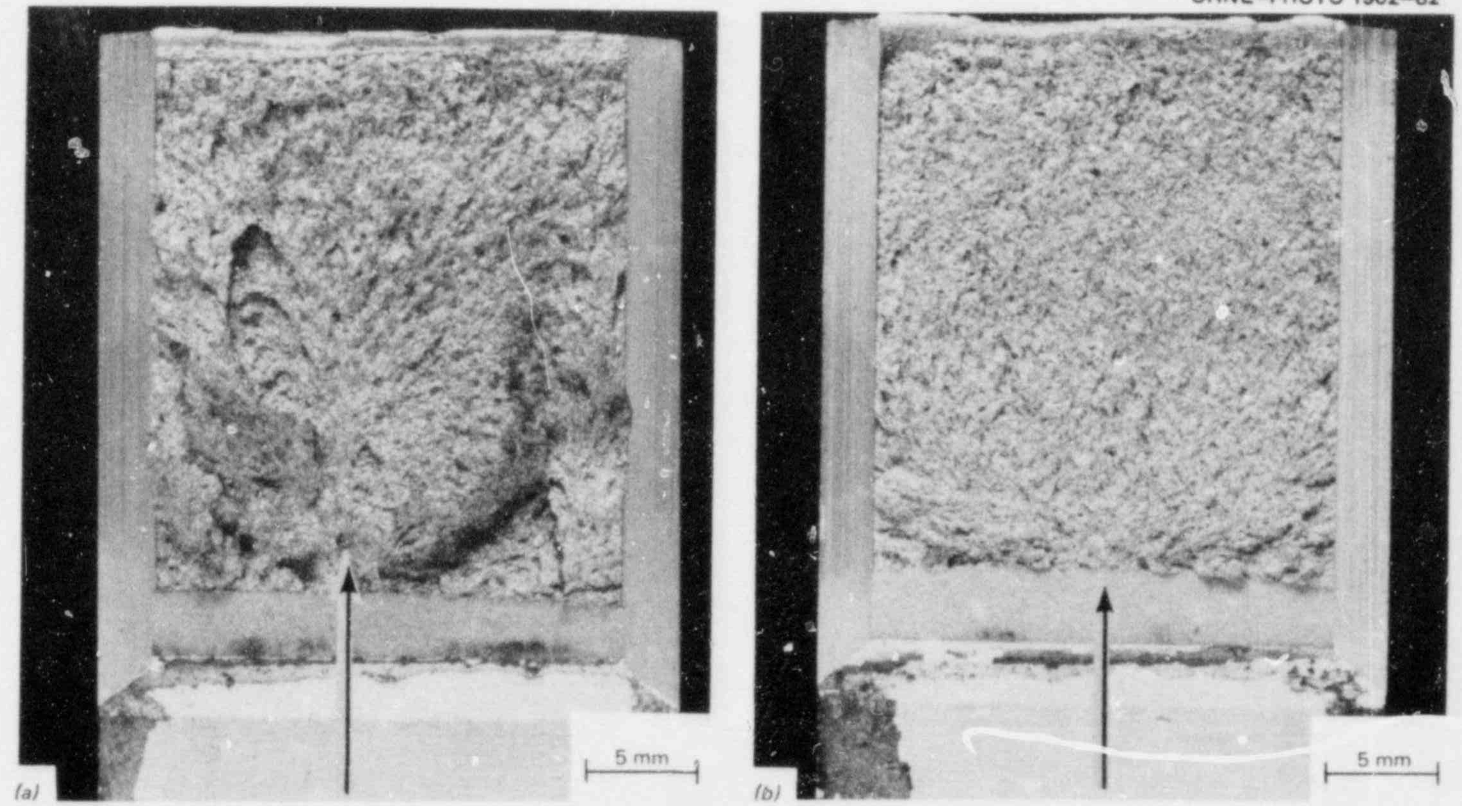

Fig. 2.7. Fracture surfaces of the two specimens: (a) specimen 60R-90-2; (b) specimen 60R-86-1. Arrow indicates general location of fracture origin.

of these examinations was to seek an explanation for the difference in the measured values of K_J in two nominally identical test specimens tested under identical experimental conditions. To achieve this objective, the examinations (1) located the origins of unstable, brittle-cleavage fracture; (2) identified any unusual microstructural features that may have been associated with the triggering of the brittle-cleavage fracture; and (3) documented the separation distance of the brittle-cleavage-fracture origin from the ductile, dimple-rupture crack front. The two specimens of interest here, however, exhibited negligible crack extension by the dimpled-rupture mechanism. The separation distances were measured essentially with respect to the fatigue-crack front.

Specimen 60R-90-2. Figures 2.8(a-c) show the fracture surface of Specimen 60R-90-2 (K_J = 180 MPa·$\sqrt{m}$) in the vicinity of the cleavage-fracture origin at increasing magnification. The cleavage-fracture origin was found to be located at the center of the indicated circle in Fig. 2.8(a) after examining the fracture surface with the aid of stereo scanning fractographs. The origin was very clearly defined in this specimen and was located by the radial pattern of tear ridges, as seen in Fig. 2.8(b). The cleavage-fracture initiating site was characterized by cleavage facets in adjacent ferrite grains that were nearly coplanar and parallel to the fatigue-crack plane. This is shown in Fig. 2.8(c), which is a higher magnification view of the boxed region in Fig. 2.8(b). The appearance is consistent with the observations of Fourney,[11] who describes it as a cluster of ferrite grains with the near-identical orientation probably originating in a single prior-austenite grain. The microstructural feature that acts as a "weak spot" and triggers the cleavage fracture in this steel may well be a favorably and similarly oriented group of ferrite grains within by the same original austenite grain. This characterization of the cleavage-initiating spots in this steel is consistent with the fractographic and metallographic observations of Fourney.[11] A suspected site for a cleavage-initiating carbide particle also is shown in Fig. 2.8(c). The cleavage-fracture origin in Specimen 60R-90-2 was located 1.74 mm from the ductile-rupture crack front.

Figure 2.8(d) shows the transition region near the fatigue crack front in Specimen 60R-90-2. Crack extension by dimpled rupture was limited in this specimen to a zone no greater than 100 μm wide.

Specimen 60R-86-1. Figures 2.9(a-d) show the fracture surface of Specimen 60R-86-1 (K_J = 86 MPa·$\sqrt{m}$) in the vicinity of the cleavage-fracture origin at increasing magnifications. In contrast to Specimen 60R-90-2, the cleavage origin in the specimen was located very close to the fatigue-crack front. The circle in Fig. 2.9(a) and the boxed regions in Figs. 2.9(b and c) locate the cleavage-initiating site, shown at higher magnification in the fractograph of Fig. 2.9(d). The "weak spot" in this specimen appears to have been located directly ahead of the fatigue-crack front. Also, there was no crack extension by dimpled rupture prior to the unstable-cleavage fracture. The separation distance of the cleavage-fracture origin in this specimen, measured from the fatigue-crack front, was of the order of 20 to 50 μm. The relative error in the measured separation distance would be very high for this specimen because of the small absolute value of the separation distance.

Summary of the fractographic observations. The identification of the cleavage-fracture origins in Specimens 60R-90-2 and 60R-86-1 provides at

ORNL-PHOTO 1903-82 (PART A)

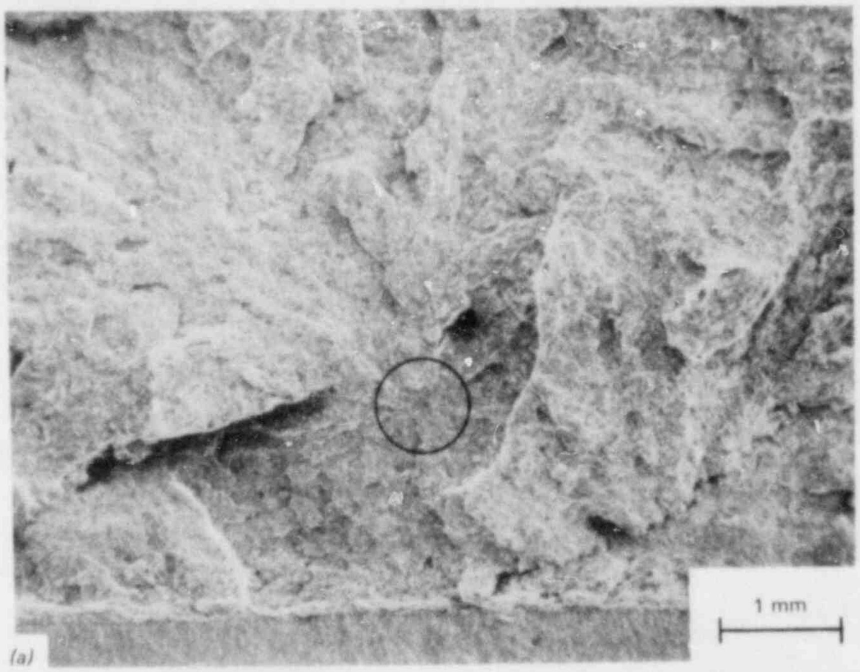

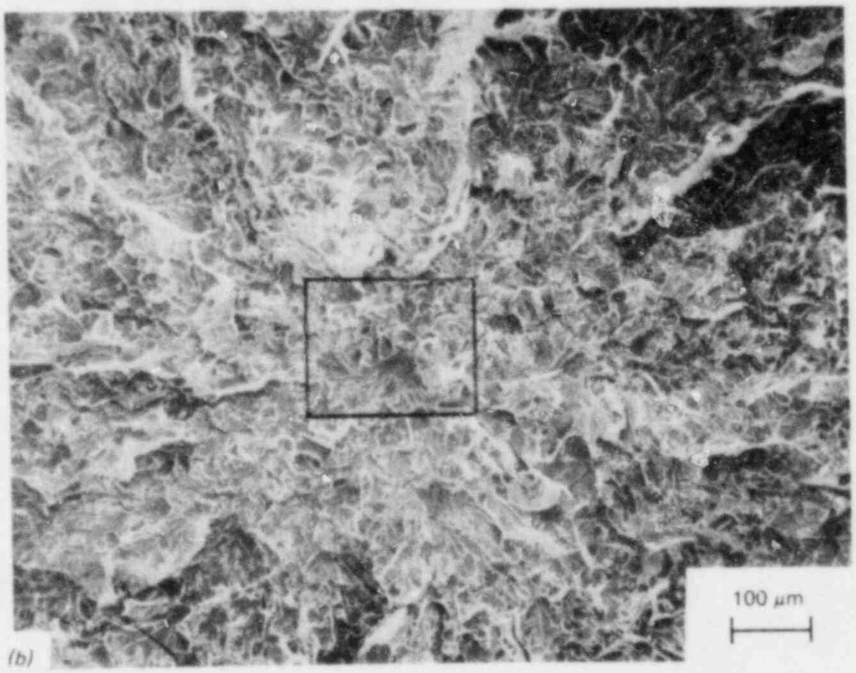

Fig. 2.8. Scanning electron micrographs of the cleavage-fracture-origin region in specimen 60R-90-2: (a) vicinity of fracture origin (center of circle); (b) origin of brittle-cleavage fracture at higher magnification (inside rectangle); (c) b at higher magnification (point C is suspected site for cleavage-initiating carbide particle); (d) fatigue crack/dimpled rupture/cleavage transition region.

ORNL–PHOTO 1903–82 (PART B)

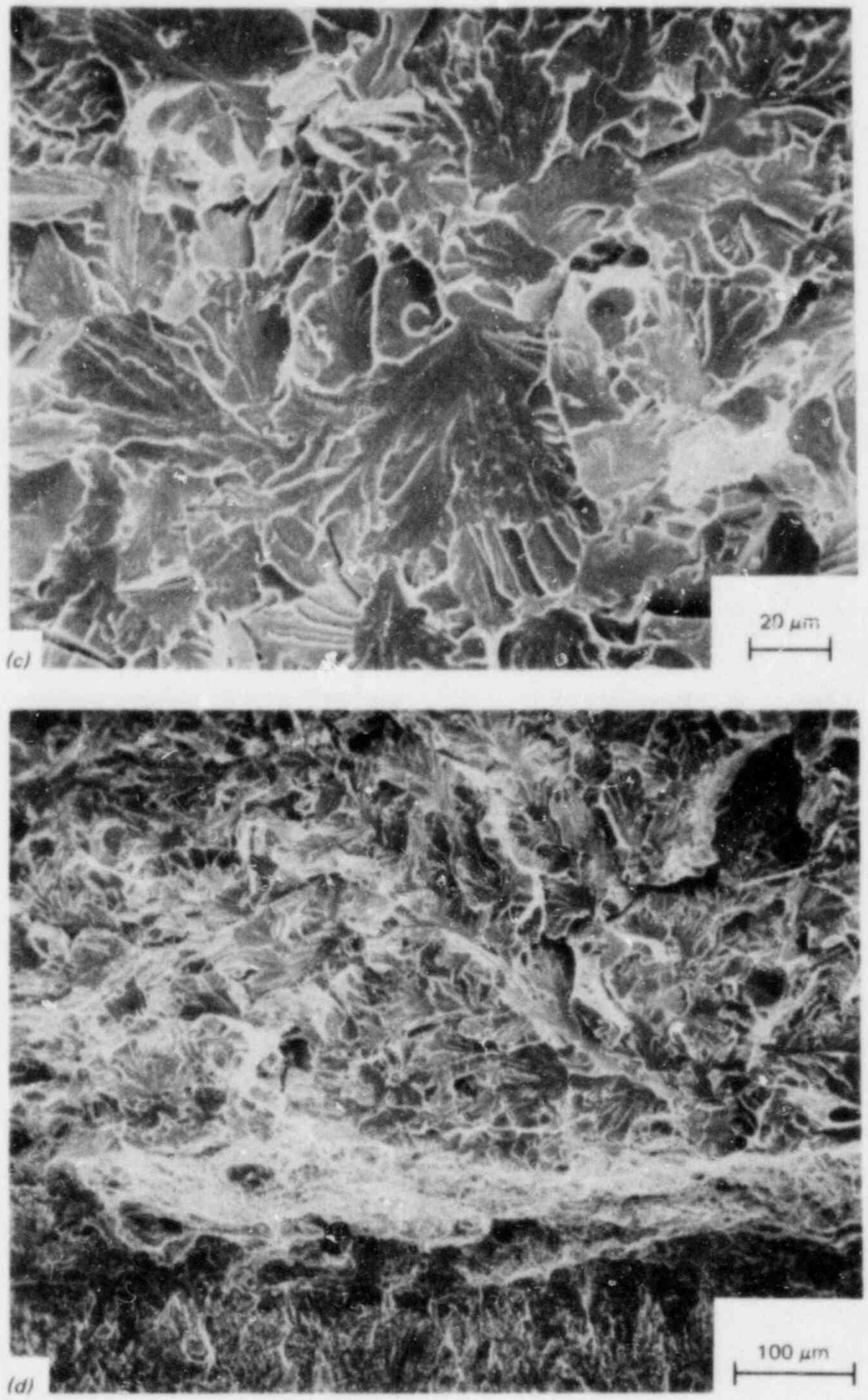

Fig. 2.8 (continued)

ORNL–PHOTO 1904–82 (PART A)

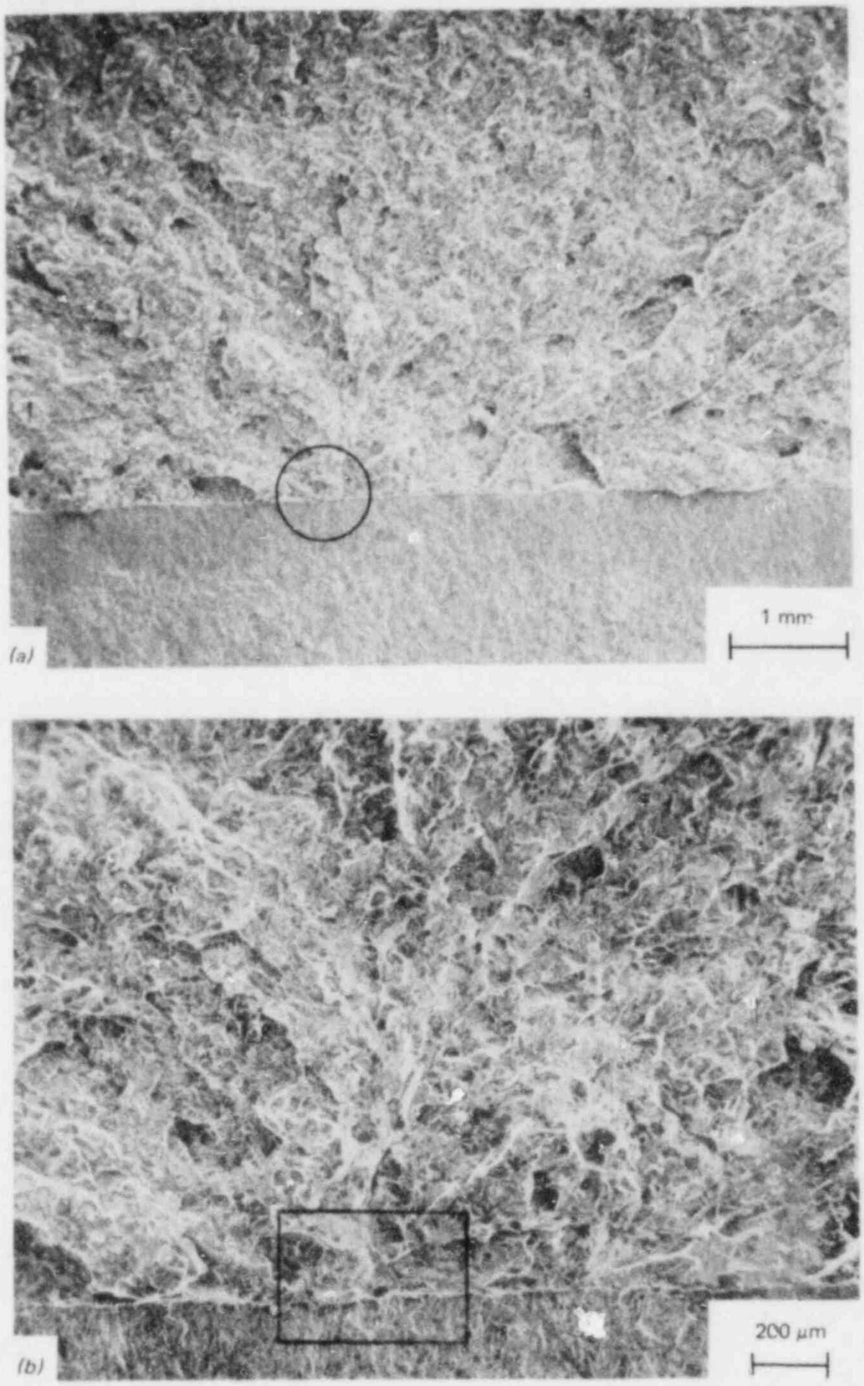

Fig. 2.9. Scanning electron micrographs of the cleavage-fracture-origin region in specimen 60R-86-1: (a) vicinity of fracture origin (center of circle); (b) origin of brittle-cleavage fracture at higher magnification (inside rectangle); (c) b at higher magnification (initiating point inside rectangle); (d) cleavage-fracture initiating site showing suspected site for cleavage-initiating carbide particle (point C).

ORNL–PHOTO 1904–82 (PART B)

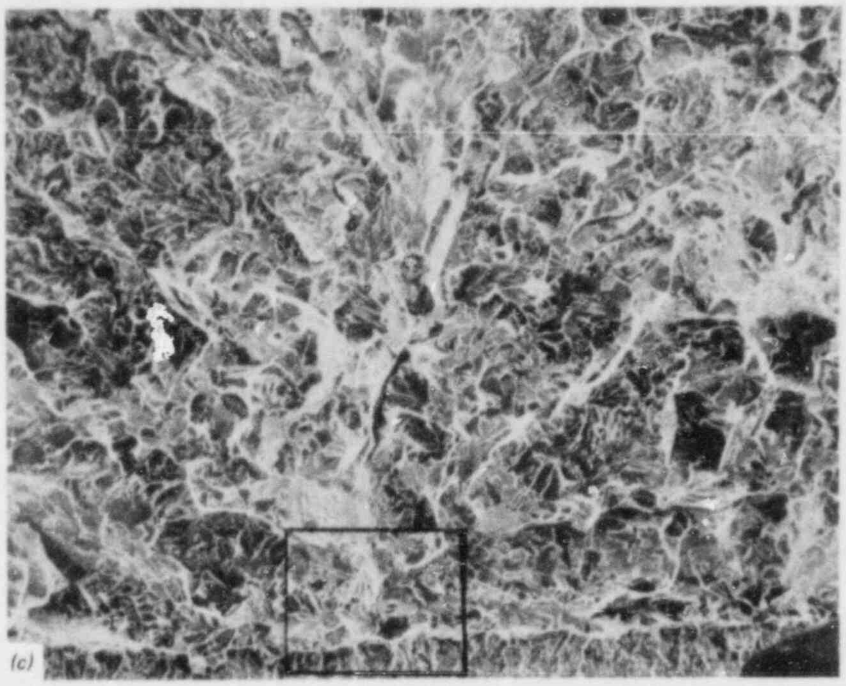

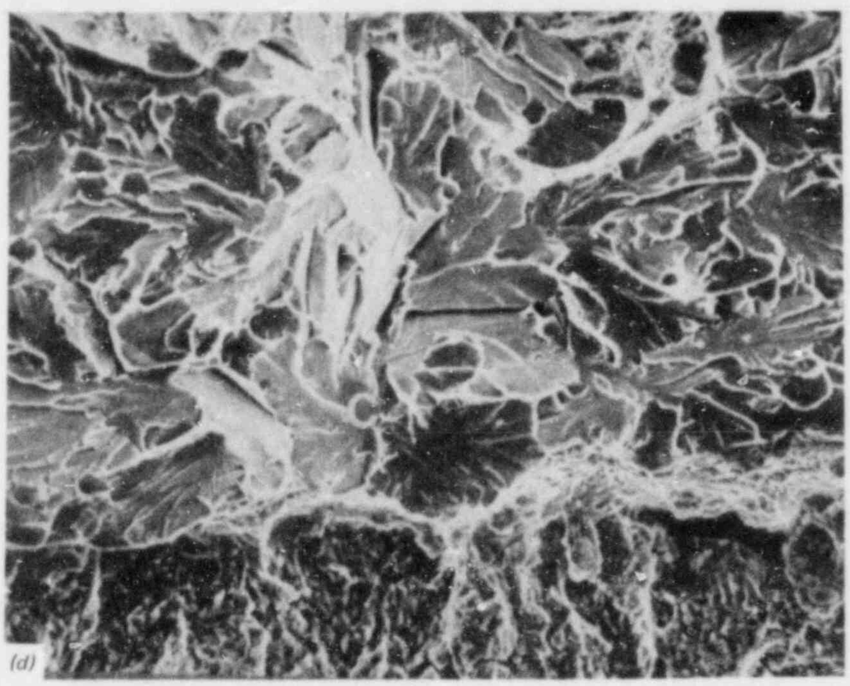

Fig. 2.9 (continued)

least a qualitative rationale for the difference in the K_I values measured in these two specimens. The difference in the measured fracture-toughness values appears to be related to the location of the cleavage-initiating weak spots with respect to the original fatigue-crack front. In Specimen 60R-90-2, the weak spot was located well ahead of the fatigue-crack front and, therefore, the applied load and, hence, K_1 had to be high before a critical stress was attained at the weak spot. By contrast, a low applied load and, hence, low value of K_I was adequate to initiate cleavage in Specimen 60R-86-1 because the weak spot was located right at the fatigue-crack front. The variation of the separation distances of weak spots from the fatigue-crack fronts (or the dimpled-rupture crack front in the more general case) causes a variation in K_{Ic} for unstable-cleavage fracture.

The characteristics of the weak spots include coplanar cleavage-grain facets in adjacent ferrite grains. The size of the weak spot cannot be measured easily. However, it may be related to the prior-austenite grain size, as was suggested by the recent observations of Fourney.[11]

<u>Crack arrest</u>. The crack-arrest-toughness (K_{Ia}) data that were obtained at BCL using compact specimens have been reported by Rosenfield et al.[6] The data (Table 2.2)* are unusual because there appears to be no temperature dependence. The reasons for this behavior are not clear. Of the two jumps in Experiment TSE-6 (Ref. 10), the second arrested about 5.2 mm from the outer wall. Thus, there are two sources of error in the reported K_{Ia} value for that jump: a rapidly varying elastic K_I vs crack length curve and the possibility of plasticity extending through the remaining ligament. To examine the latter point, the remaining-ligament criterion developed for compact specimens was applied to the cylinder, for size-independent toughness:[7]

$$\frac{w-a}{(K_a/\sigma_{yD})^2} = \beta \geq 1.27 \ , \qquad (12)$$

where w−a is the remaining ligament and σ_{yD} is the dynamic yield strength (estimated at 875 MPa for TSE-6). Because the actual value of the right side of Eq. (12) is 0.37, it would appear that a significant plasticity correction is needed.

Figure 2.10 is the prediction for TSE-6 from the previous report,[6] shown as the solid line, with the dispersion represented by dashed lines. The actual results are shown as open points. The agreement between the compact-specimen data and the lower temperature TSE-6 jump is excellent.

---

*Subsequent to the issuance of that report, the ASTM Task Group on Crack Arrest recommended a slightly different slip-gage-displacement/stress-intensity relation than the one that had been used at BCL. The effect of the change was to lower the previously reported K_a value of Specimen 82 by 4 $MPa\cdot\sqrt{m}$ and to lower the other K_a values by no more than 2 $MPa\cdot\sqrt{m}$. Although the K_D values were more substantially affected, in no case was the change greater than 5 $MPa\cdot\sqrt{m}$.

Table 2.2. Crack-arrest toughness values of ORNL TSE-6 steel[a]

Compact specimen No.	Test temperature (°C)	K_o (MPa·$\sqrt{m}$)	K_{ID} (MPa·$\sqrt{m}$)	K_a (MPa·$\sqrt{m}$)
60R-85	11	82	70	71
60R-88	9	105	71	62
60R-82	39	136	99	74
60R-80	39	131	87	51[b]
60R-83	66	155	106	68
60R-86	66	177	127	87
60R-81	78	1[illegible]2	112	69
60R-89	79	1[illegible]4	119	70
60R-84	79	158	109	72
Cylinder				
Jump 1	32			63
Jump 2	63			104[b]

[a]The compact-specimen data have been revised to incorporate computational methods agreed upon by the ASTM Task Group on Crack Arrest.

[b]Value uncertain due to excessively small remaining ligament.

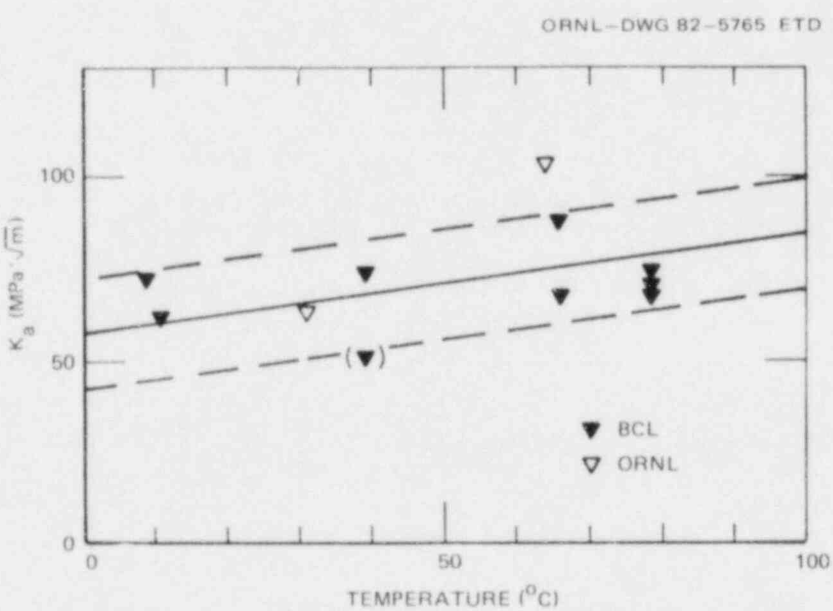

Fig. 2.10. Crack arrest of TSE-6 steel.

Note, however, that one of the compact specimens (No. 80 at 39°C) exhibited a slightly low value of K_a. That specimen also had the smallest remaining ligament (0.145 w). Even so, it still satisfied the remaining-ligament criterion of Eq. (12) (β = 4.80). While this single result may not be of significance, the same phenomenon was observed in the Task 4 studies reported in a subsequent section of this report and is discussed further in connection with those results.

The data in Fig. 2.10 bring to 10 the number of jumps in ORNL thermal-shock experiments for which small-specimen crack-arrest data have been measured. Cheverton et al.[12] have pointed out that the cylinder crack-arrest data all lie above the ASME Section XI K_{Ia} curve. Their observation reinforces the conclusion of Rosenfield et al.[7] that the curve does provide a conservative description of the available data. The degree of conservatism may be estimated from the analysis of Rosenfield et al., that showed that the previous TSE data can be described by

$$K_{Ia} = K_{Ia}(CV30) + 4.89 + 0.47(T-CV30) , \qquad (13)$$

where K_{Ia} is the cylinder result in MPa·$\sqrt{m}$, K_{Ia}(CV30) is the mean value of K_{Ia} for compact specimens at the 41-J Charpy temperature, and T is the temperature of the TSE in degrees Celsius. The standard deviation of Eq. (13) is 16 MPa·$\sqrt{m}$. Table 2.3 is an updated listing of the material parameters in Eq. (13) generated using compact specimens. Note that the toughness levels in the right-hand column are considerably higher than the value used in Section XI (K_{Ia} at CV30 = 44 MPa·$\sqrt{m}$). Figure 2.11 is an update of the earlier test of Eq. (13). The lines denoted "A" and "B" in the figure are lower levels based on the statistical analysis of material properties used in aerospace applications.[7] All of the TSE data are seen to lie above the B line, giving confidence in Eq. (13) and the statistical analysis. This result suggests that measurement of K_{Ia} using compact specimens at CV30 will provide a means of conservatively predicting vessel

Table 2.3. Crack-arrest-toughness parameters for steels used in thermal-shock experiments

Experimental steel	CV30 (°C)	K_{Ia} (CV30) (MPa·$\sqrt{m}$)
TSE-4	60	97
TSE-5	40	72
TSE-5A	-7	66
TSE-6	40	68

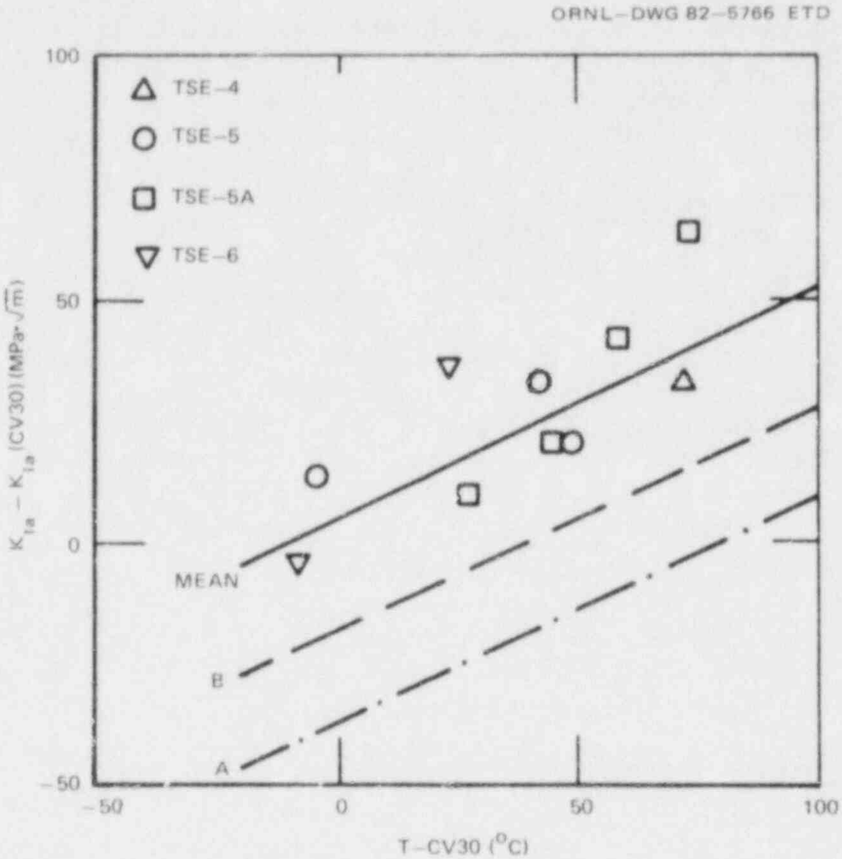

Fig. 2.11. Comparison between predicted and measured K_{Ia} values for the ORNL-TSE data.

behavior between about (CV30 − 10) and (CV30 + 75). A consequence of only needing compact-specimen data at CV30 is that smaller specimens can be used than have been used previously. The further work on size effects listed in a subsequent section of this report is aimed toward this goal.

Analysis of crack initiation and arrest in ORNL thermal-shock experiment TSE-6. Background. During this report period, an "application-phase" analysis of the first of the two crack-initiation-and-arrest events detected during Thermal-Shock Experiment TSE-6 was performed using BCL's dynamic-finite-element code FRACTDYN. Starting with an initial crack length of 7.6 mm, crack propagation and arrest were modeled by forcing the crack to follow an experimentally established dynamic-fracture-toughness relation in which K_{ID} is both temperature and crack-velocity dependent. The test conditions and geometry of the TSE-6 cylinder are shown in Table 2.4. The finite-element mesh used in the analysis is shown in Fig. 2.12. The temperature distribution used in the analysis was determined from the ORNL-measured radial temperature profile[10] that corresponded to 1.17 min in the TSE-6 transient and is shown in Fig. 2.13.

Preliminary comments. The static-finite-element-analysis results contained in the Quick Look Report of TSE-6 (Ref. 10) indicated that the

Table 2.4. Test conditions for TSE-6

Parameter	Value
Test specimen	TSC-3
Test-specimen dimensions, m	
OD	0.001
ID	0.838
Length	1.22
Test-specimen material	A508, Class-2 composition
Test-specimen heat treatment	Tempered at 613°C for 4 h
K_{Ic} and K_{Ia} curves used in design	K_{Ic} and K_{Ia} curves deduced from TSE-5
Flaw	Long, axial sharp crack, a = 7.6 mm
Temperatures, °C	
Wall (initial)	96
Sink	−196
Coolant	LN_2
Flow conditions	Natural convection
Coating on quenched surface	Rubber cement (3M-NF34)
Coating surface density, g/m²	241

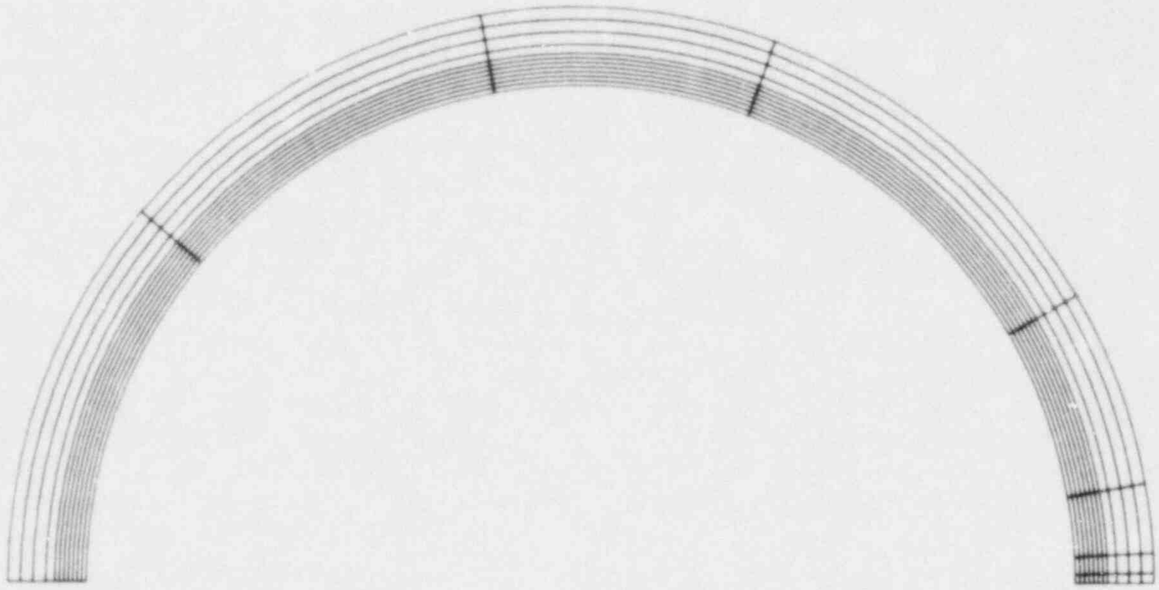

Fig. 2.12. Finite-element mesh used for TSE-6 analysis.

ORNL-DWG 82-5768 ETD

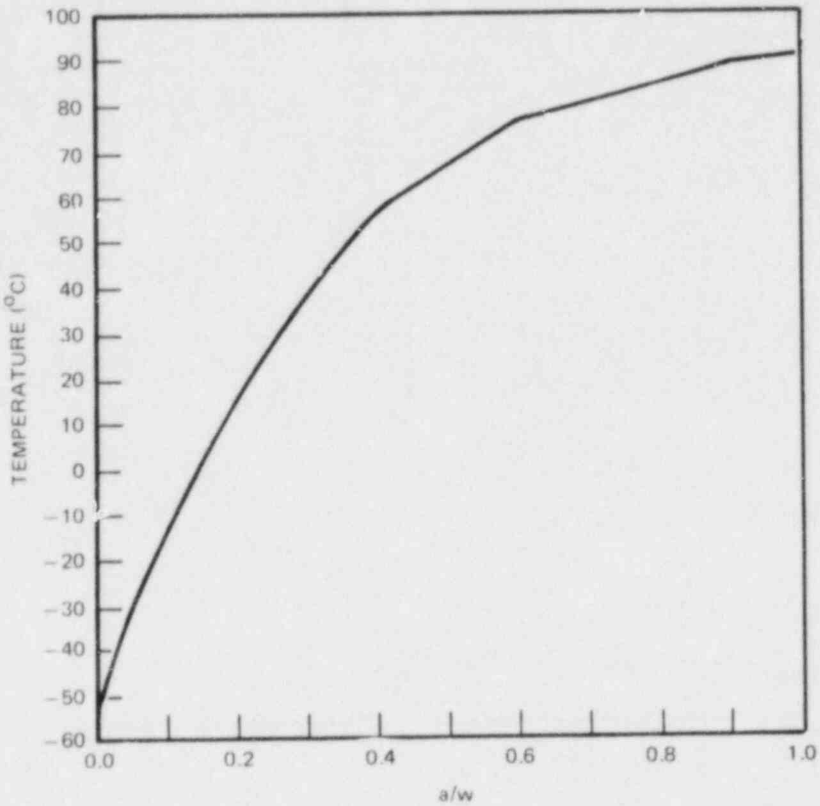

Fig. 2.13. Measured radial temperature distribution at 1.17 min in TSE-6 transient.

given temperature distribution does not produce a sufficiently high static-stress-intensity factor for the initial crack length to initiate. Inasmuch as crack initiation did indeed occur during the actual experiment, this discrepancy was attributed to (1) possible tensile residual stresses and (2) possible local reduction in the fracture toughness of the material near the tip of the initial crack. Neither of these two possible effects were characterized with adequate precision so that they could be included in the analysis.

To verify the static K_I result for the initial crack length reported in ORNL Quick Look Report, a static-finite-element analysis was first performed. The static-stress-intensity factor was calculated from the J-integral relation, and a value of $K_I = 47.4$ MPa·$\sqrt{m}$ was obtained. This compared quite well with the K_I value of 46 MPa·$\sqrt{m}$ given in the Quick Look Report.

Dynamic analysis. Because the initiation toughness is 53 MPa·$\sqrt{m}$, it is clear from the static analysis that the use of the average K_D vs temperature relation for TSE-6 will not result in crack initiation. This relation was represented by the following equation:

$$K_{ID} = (57.1 + 0.275T)\left[1 + \left(\frac{\dot{a}}{620}\right)^2 + \left(\frac{\dot{a}}{1240}\right)^3\right] , \qquad (14)$$

where

K_{ID} = dynamic fracture toughness, $MPa\cdot\sqrt{m}$;
T = temperature, °C;
$\dot{a}$ = crack velocity, m/s.

To initiate the crack, three possibilities existed:

1. account for reduction in local toughness,
2. apply a residual stress distribution, and
3. use a different K_{ID} relation.

The first two alternatives were discarded on the ground that, in the absence of precise quantitative experimental measurements for either a local reduction in toughness or the residual stress distribution, the adjustment would have to be rather arbitrary. Instead, knowing that there is a typical scatter of ± 15 $MPa\cdot\sqrt{m}$ in the experimental data on which Eq. (14) is based,[7] the following K_{ID} relation was employed:

$$K_{ID} = (49 + 0.275T)\left[1 + \left(\frac{\dot{a}}{620}\right)^2 + \left(\frac{\dot{a}}{1240}\right)^3\right] . \tag{15}$$

Equation (15) was chosen so that the zero-velocity value of K_{ID} is sufficiently low to allow for crack initiation in the computation.

Results and discussion. The result of the dynamic analysis is that arrest occurred when K_a = 46.7 $MPa\cdot\sqrt{m}$. Crack initiation occurred at K_I = 47.4 $MPa\cdot\sqrt{m}$. The crack jump was 5.7 mm, giving a total penetration at the first arrest of 13.3 mm, with the arrest time equal to 57.5 μs.

The analysis underestimated the experimentally found crack depth at first arrest by about 35%. Three of the reasons for this discrepancy are:

1. inaccuracy induced by not accounting for possible local variations in toughness,
2. inaccuracies induced as a result of ignoring the presence of residual stresses, and
3. uncertainty regarding the functional dependence of K_{ID} on crack velocity.

While not much can be accomplished regarding the first two possible reasons in the absence of precise experimental measurements, the third possibility could be explored further. It may be worthwhile to attempt at least one more analysis where a different K_{ID} relation is used. Such an exercise is not only expected to give better agreement with experimental results, but it also will provide a further understanding of the proper velocity dependence that can be used. If, for example, a velocity-independent K_{ID} relation provides an overprediction of crack-jump length, then at least a bound on the K_{ID} relation can be found.

2.2.3 Task 3: Crack initiation

The objective of Task 3 is to determine the effect of crack-tip morphology on K_{IC}. Particular attention is to be focused on reinitiation of an arrested cleavage crack.

During the current quarter, crack-arrest specimens were machined from TSE-5A steel. It is planned that the arrest cleavage crack tip will be produced by Battelle's usual wedge-loading procedures. The specimens then will be reloaded to failure using a double-displacement measurement technique as close as possible to that of ASTM E561.

2.2.4 Task 4: Crack arrest

The objective of Task 4 is to improve crack-arrest test procedures. Efforts during the current quarter focused on completing the specimen-miniaturization experiments initiated in the previous quarter.

The early development of crack-arrest testing involved very large specimens. For example, the smaller of the specimen designs used in the ASTM Cooperative Test Program[13] was 200 x 200 x 50 mm. Clearly, there are many situations where this size is prohibitively large. One of the most important is the study of irradiated steels, because space is at a premium within a reactor.

The only data that can be used to design smaller specimens are those of Marschall et al.;[14] this was the only systemmatic study of the size effect in crack-arrest testing. Steel from the Cooperative Test Program was tested at the same temperatures used in that program, and it was found that halving the dimensions cited previously did not change the K_{Ia} values. Further analysis of those data by Rosenfield et al.[6] resulted in the recommended size limitations as follows:

$$B \Big/ \left(\frac{K_a}{\sigma_{yd}}\right)^2 \geq \alpha \geq \frac{4}{\pi} = 1.27 ,$$

$$\frac{(w-a)}{\left(\dfrac{K_a}{\sigma_{yd}}\right)^2} \geq \beta \geq \frac{4}{\pi} = 1.27 ,$$

$$\frac{2H}{\left(\dfrac{K_o}{\sigma_{ys}}\right)^2} \geq \gamma = 1.00^* .$$

---

*Limits yielding on loading to K_o.

These same size limitations are likely to emerge from the ASTM Task Group on Crack Arrest, although Rosenfield et al.[6] found evidence of size-independent toughness for still smaller specimens. Note that the dynamic yield strength is used because crack propagation and arrest are dynamic events. The dynamic yield strength is approximated by adding 200 MPa to the static yield strength.[15]

The present series of experiments was undertaken to verify the results reported by Marschall et al.[14] and to determine whether even smaller specimens could be used. Specimens of several sizes were machined from a prolong of the ASTM A508-2 steel cylinder used in ORNL Thermal-Shock Experiment TSE-5A.[16] It was tested at 0°C, a temperature at which BCL compact-specimen data are consistent with the trend of the large-cylinder data.[6] The specimens, which had starting-notch root radii of 0.25 mm, were of the design used by Marschall et al.[14] with two exceptions:

1. Two of the three 6.3-mm-thick specimens exhibited extreme tunneling, with crack travel being considerably less at the roots of the side grooves than at the midplane. Marschall et al. did not have this problem in the specimen of this thickness that they tested. To resolve the problem in the current tests, 40% side-groove depth was used in a second set of 6.3-mm-thick specimens instead of the usual 25%. Data for the 25% side-groove specimens are listed in Table 2.5 but are not plotted in figures presented here.

2. As is shown in Fig. 2.14, specimens with the smallest face dimension required modification of the starting-notch tip and of the displacement-measurement point. Because the usual welding rod used for notch-tip embrittlement (Hardex N) was too wide to fit a notch of usual proportions, the tungsten inert gas (TIG) process was used instead to harden the notch-tip region without depositing a weld bead. In addition, the clip gage was placed 0.33 w behind the load line instead of at the usual 0.25 w position. To correct for this difference, the displacement behind the load line was considered to vary linearly with position in accord with the calculations of Newman[17] and of Saxena and Hudak.[18] As a result, the measured displacement was multiplied by 0.93 for calculation of stress intensity via the stress-intensity relation of Ripling.[19] The cyclic-load test procedure[14] was used to produce unstable fracture. Values of K_a were calculated using the displacement at crack arrest.

The results are given in Tables 2.5 and 2.6.* With the exception of the smallest-face-dimension specimens, the data were quite consistent. These small specimens not only had significantly lower K_a values than did the balance of the specimens, but they had significantly lower K_o (stress intensity at initiation) values. Although the lower K_o values were likely due to the TIG weld, this factor should not invalidate the K_a data.

The effect of thickness on K_a is shown in Fig. 2.15. The horizontal scatter band represents one standard deviation around the mean for typical crack-arrest data.[7] The 12.7-mm-thick specimens at the lower edge of the band are those with the smallest face dimension. The one positive K_a deviation from the scatter band is for one of the thinnest specimens used.

---

*The K_o and K_a values previously reported[6] have been recalculated using the ASTM Task Group relation. This increased K_a for Specimen 97 by 10%. The other specimens changed by <5%.

Table 2.5. Crack arrest data (TSE-5A steel tested at °C)

Specimen No.	Specimen dimensions[a] (mm)					Crack length (mm)		Cycles to failure	Displacement (2δ) (mm)	
	2H	W	B	Bn	N	Initiation	Arrest		Initiation	Arrest
5A-91	152.4	127.0	50.9	38.1	10.67	53.1	103.2	16	1.17	1.31
92	152.4	127.0	50.9	38.1	10.67	51.3	107.7	14	1.13	1.18
93	101.6	84.68	25.3	18.92	7.62	29.97	67.1	10	0.74	0.83
94	101.6	84.58	25.3	19.30	7.62	33.3	72.1	19	1.02	1.09
95	101.6	84.58	25.3	18.80	7.62	33.0	70.6	16	0.94	1.08
96	101.6	84.68	12.6	9.27	7.62	33.6	73.0	17	1.08	1.19
97	101.6	84.84	12.7	9.53	7.62	29.72	72.9	15	0.98	1.06
98	101.6	84.71	12.6	9.27	7.62	35.4	71.25	10	1.00	1.07
99	101.6	84.84	6.31	4.70	7.62	31.66	46.39[b] 57.14[c]	16	1.03	1.06
100	101.6	84.58	6.31	4.70	7.62	29.97	46.0[b] 52.5[c]	13	0.86	0.89
101	101.6	84.71	6.31	4.70	7.62	29.72	69.09	16	0.92	0.94
102	101.6	84.71	6.31	3.81	7.62	29.3	67.8	8	0.71	0.82
103	101.6	84.71	6.31	3.81	7.62	29.3	70.2	10	0.74	0.85
104	101.6	84.58	6.37	3.56	7.62	29.7	62.0	10	0.70	0.77
45	152.4	127.0	26.7	20.57	10.67	44.2	91.4	21	0.88	0.96
55	152.4	127.0	26.7	20.32	10.67	45.1	99.4	17	0.93	1.02
1	50.8	42.29	12.7	9.65	3.81	16.89	35.69	9	0.47	0.55
2	50.8	42.29	12.7	9.65	3.81	16.89	35.50	11	0.60	0.61
3	50.8	42.29	12.7	9.65	3.81	16.89	36.60	15	0.57	0.67

[a]Terminology of Marschall et al. (Ref. 14).

[b]Average length.

[c]Greatest extent.

Table 2.6. Crack-arrest toughness
(TSE-5A steel tested at 0°C)

Specimen No.	Stress intensity and toughness ($MPa \cdot \sqrt{m}$)		
	K_o	K_D	K_a
5A-91	173.9	120.9	82.7
92	172.0	113.9	65.7
93	149.7	100.0	68.6
94	191.6	126.1	72.4
95	179.8	119.0	77.7
96	205.4	133.1	77.1
97	198.7	123.8	69.0
98	183.8	124.4	75.6
99[a]	202.3	171.6[b]	154.1[b]
		153.3[c]	119.0[c]
100[a]	175.0	146.7[b]	130.0[b]
		136.5[c]	111.7[c]
101	187.2	121.7	72.1
102	162.5	106.4	73.8
103	169.4	108.1	69.6
104	164.6	115.5	86.6
45	144.4	102.8	77.6
55	151.9	102.1	70.1
1	123.1	81.5	53.4
2	158.3	105.4	60.3
3	150.4	97.5	59.8

[a]Data invalid and crack not straight (tunneled); not plotted in Figs. 2.15 and 2.16.

[b]Based on average crack length.

[c]Based on greatest extent of crack growth.

ORNL-DW 82-5769 ETD

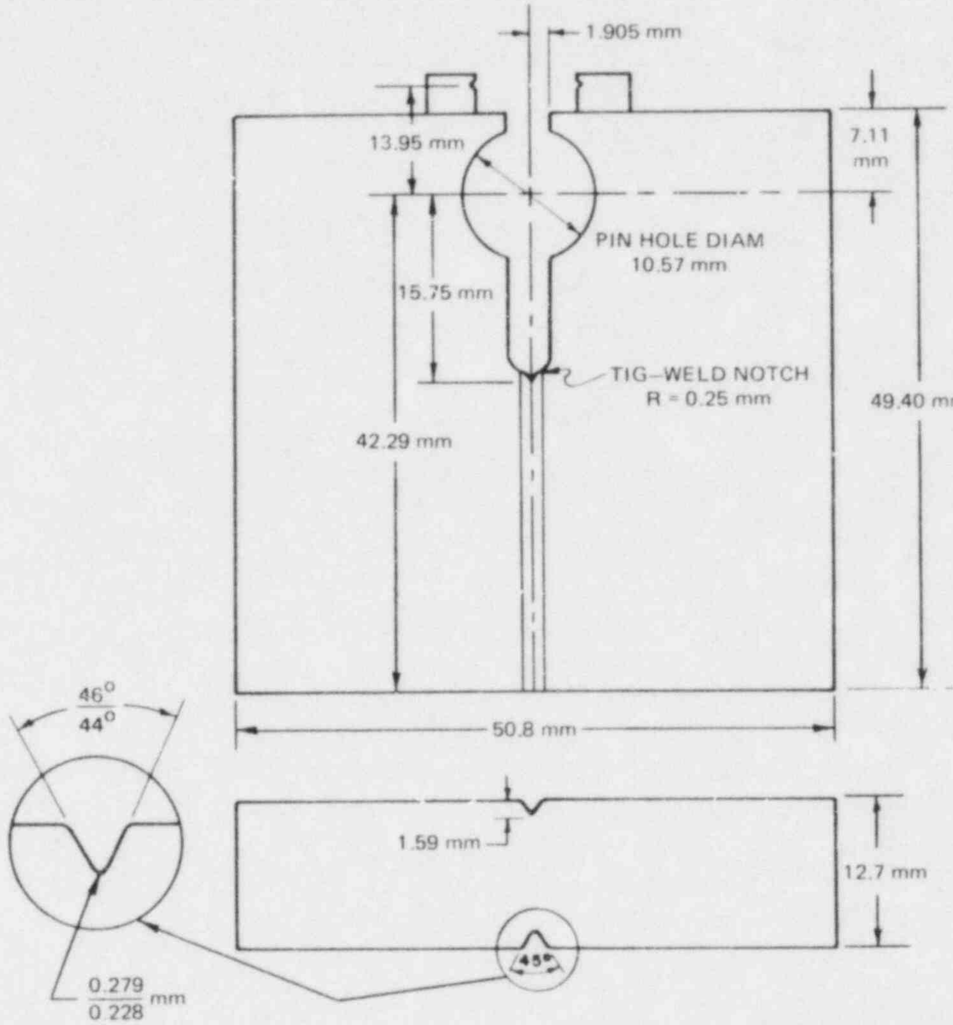

Fig. 2.14. Miniature crack-arrest specimen.

The dashed line represents the likely ASTM size limit, which is seen to be conservative.

When the data are ordered according to the length of the remaining ligament (Fig. 2.16), the difference in the smallest-face-size specimens becomes more evident. Even so, these specimens do not raise the apparent toughness, but lower it. This is, of course, in contrast to typical small-specimen behavior, where plasticity causes increased toughness. The cause of the low K_a values for these small remaining ligaments is not completely clear. As noted in the Cooperative Test Program Report,[13] there is a tendency for K_a to decrease with increasing crack-jump length (Δa). However, the miniature specimens experienced relatively short jumps (i.e., low Δa values) due to their small size. There is a slight tendency in the K_a data of Table 2.6 to decrease with relative jump length $\Delta a/w$, and this would be consistent with the Cooperative Test Program result. However, the significance of this observation is not clear.

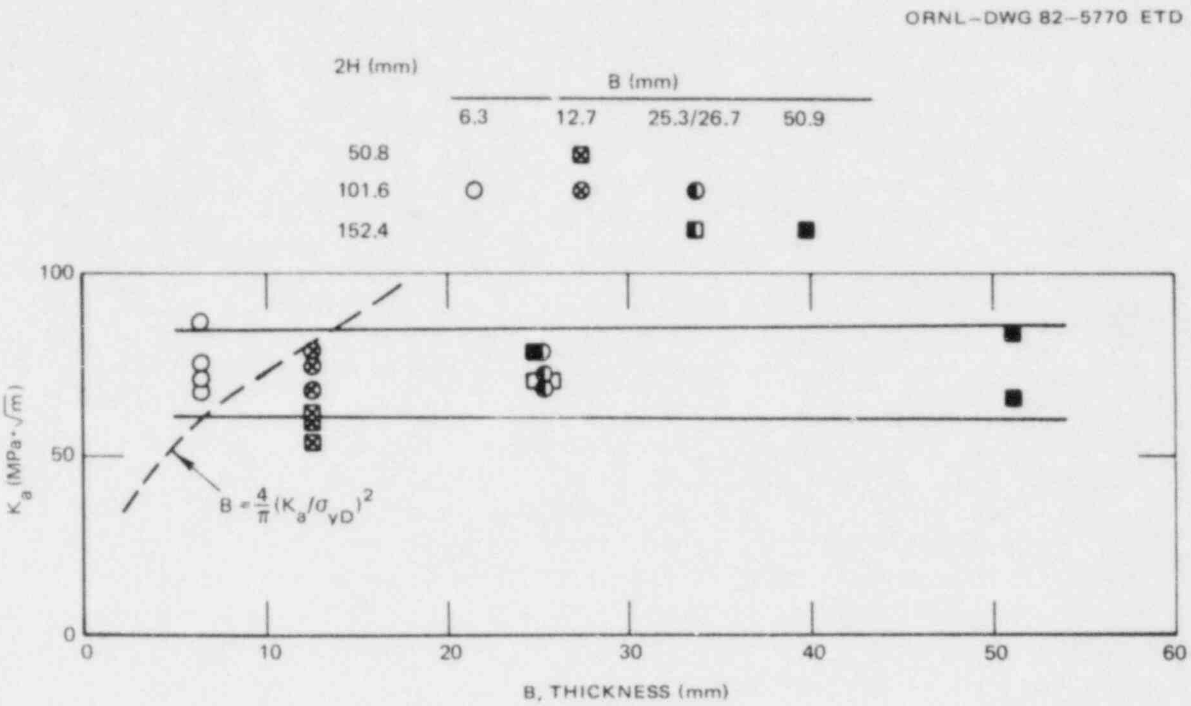

Fig. 2.15. Effect of thickness on K_a. Data are for TSE-5A steel tested at 0°C.

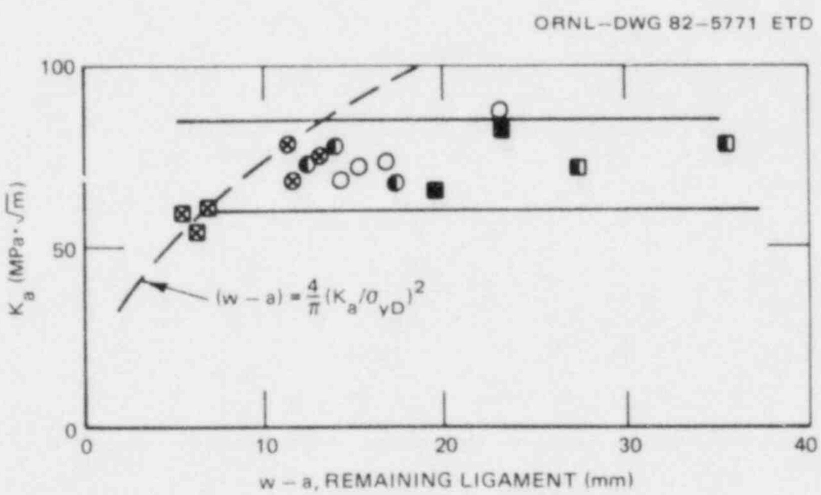

Fig. 2.16. Effect of the length of the remaining ligament on K_a. Data are for TSE-5A steel tested at 0°C. See Fig. 2.15 for legend.

A possible explanation for the size independence of K_a can be found with the aid of fracture-surface observations. Figure 2.17 shows specimen surfaces. Note that, for the specimens of the largest size, the one with the larger K_a value (5A-91) shows an extreme example of unbroken ligaments of the kind reported by Hahn et al.[20] These ligaments are believed to be nucleated when the advancing crack encounters a tough region in the steel. As was suggested by Hahn et al., the crack front develops a step to bypass the tough region. As the step advances, it leaves behind a layer of unbroken material that serves as a line of pinching forces imposing a retarding contribution to the crack-tip stress intensity and raising the apparent value of K_a. Actually, visual observation underestimates the ligamentation, since on a microscopic scale, many fine ligaments are observed. Further visual observation of specimens of any given size shows that the higher K_a values are associated with more prominent ligaments. In addition, the tendency for visual ligamentation decreases with decreasing thickness (Fig. 2.18).

Assuming that the density of ligament-nucleating tough regions is low, thinner specimens would be less likely to contain one and, therefore, would exhibit longer crack travel and lower K_a values. Counteracting this trend would be an increase of K_a with decreasing thickness due to plasticity. Apparently the two trends compensate for one another, resulting in an apparent size independence of K_a.

Finally, no trend is apparent in the relation between K_a and normalized initiation stress intensity (Fig. 2.19). These data also confirm the validity of the suggested requirements in Sect. 2.2.4.

In practical terms, the use of small-face-dimension, thin specimens (51 x 51 x 13 mm) provides several advantages. As seen in Fig. 2.18,

ORNL–PHOTO 1905–82

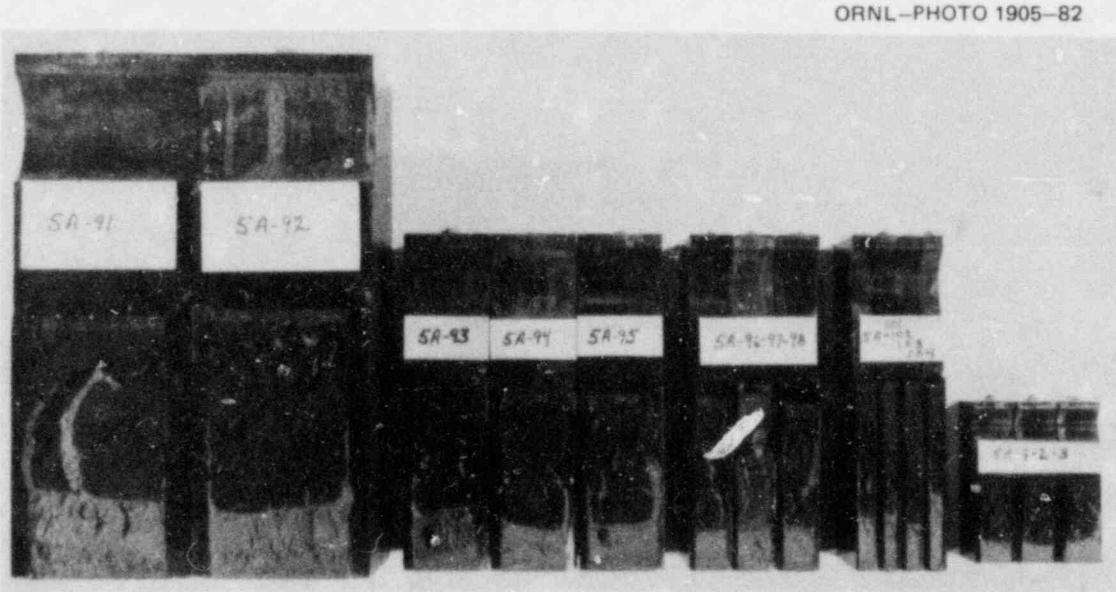

Fig. 2.17. Fracture surfaces of crack-arrest specimens of TSE-5A steel tested at 0°C.

ORNL-PHOTO 1906-82

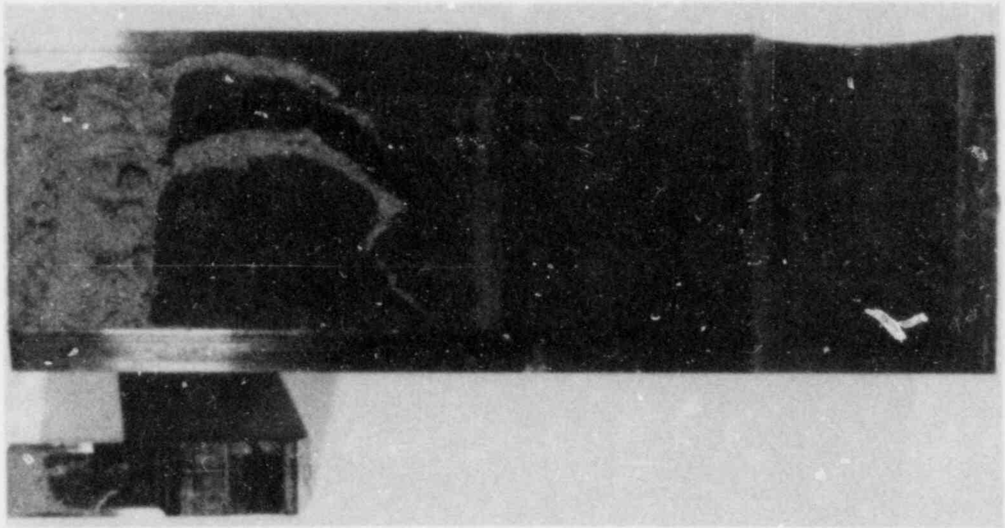

Fig. 2.18. Comparison of largest and smallest specimens used in the size-effect study.

ORNL-DWG 82-5772 ETD

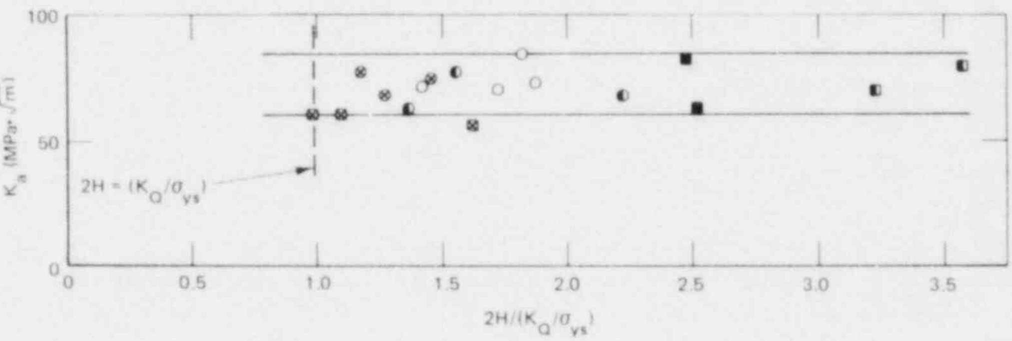

Fig. 2.19. Effect of face dimensions on K_a. Data are for TSE-5A steel at 0°C. See Fig. 2.15 for legend.

their volume is 1/64 of the smaller of the two Cooperative Test Program samples. Therefore, they present a significant advantage for radiation-embrittlement studies. At the same time, if the results of this study are confirmed, such specimens can provide a lower-bound K_a value for much larger specimens, such as those used in the ORNL thermal-shock experiments. Cheverton[10] has already noted that 150 x 150 x 25-mm specimens tend to understate the toughness of the large cylinders used in those experiments. Because the cylinders are likely to have more ligamentation, his observation is consistent with the tough-region hypothesis. The degree of conservatism with respect to reactor pressure vessels might be even larger and calls for further investigation of very small specimens.

References

1. B. R. Bass and J. W. Bryson, "Computational Methods for Combined Thermo-Mechanical Loading," *Heavy-Section Steel Technology Program Quart. Prog. Rep. October–December 1981*, NUREG/CR-2141.

2. H. G. deLorenzi and C. F. Shih, *Finite Element Implementation of the Deformation Theory of Plasticity*, General Electric TIS Report 80CRD058 (April 1980).

3. A. Mendelson, *Plasticity: Theory and Application*, Macmillan, New York, 1968.

4. H. Hencky, "Zur Theorie Plastischer Deformationen und der hierdurch im Material hervorgerufenen Nachspannungen," *Z. Angew. Math. Mech.* 4, 323–344 (1924).

5. P. G. Hodge and G. N. White, "A Quantitative Comparison of Flow and Deformation Theories of Plasticity," *J. Appl. Mech.* 17, 180–184 (1950).

6. A. R. Rosenfield et al., *Quarterly Report on Battelle-Columbus HSST Support Program, October–November, 1981.*

7. A. R. Rosenfield et al., *Quarterly Report on Battelle-Columbus HSST Support Program, June–September, 1981.*

8. A. R. Rosenfield and D. K. Shetty, "Lower-Bound Fracture Toughness of a Reactor-Pressure-Vessel Steel," *Eng. Fract. Mech.* 14, 833–842 (1981).

9. A. R. Rosenfield and D. K. Shetty, "Cleavage Fracture of Steel in the Upper Ductile-Brittle Transition Region," *Eng. Fract. Mech.* (in press).

10. R. D. Cheverton, "HSST Thermal-Shock Program Quick-Look Report for TSE-6," ORNL/TSP-1008 (1981).

11. W. L. Fourney, "Investigation of Damping and of the Cleavage Fibrous Transition in Reactor Grade Steel," *Quarterly Report to ORNL*, University of Maryland, Dec. 31, 1981.

12. R. D. Cheverton et al., "Fracture Mechanics Data Deduced from Thermal Shock and Related Experiments with LWR Pressure Vessel Material" to be presented at ASME Pressure Vessel Design Symposium, Orlando, Florida, 1982.

13. P. B. Crosley et al., "Final Report on Cooperative Test Program on Crack Arrest Toughness Measurement," to be published by NRC in 1982.

14. C. W. Marschall, P. N. Mincer, and A. R. Rosenfield, "Subsize Specimens for Crack-Arrest Testing," presented at the 14th National Symposium on Fracture Mechanics, Los Angeles, California, 1981.

15. G. T. Hahn and A. R. Rosenfield, "Numerical Descriptions of the Ambient, Low-Temperature, and High Strain Rate Flow and Fracture Behavior of Plain Carbon Steel," *Trans. Am. Soc. Met.* 59, 962–980 (1966).

16. R. D. Cheverton, "Experimental Verification of Behavior of Surface Flaws in Thick-Wall Cylinders During Thermal Shock: TSE-5 and TSE-5A," presented at Eighth Water Reactor Safety Research Information Meeting, Gaithersburg, Maryland, October 30, 1980.

17. J. C. Newman, Jr., *Stress Analysis of the Compact Specimen Including the Effects of Pin Loading*, ASTM STP 560, pp. 105–121 (1974).

18. A. Saxena and S. J. Hudak, Jr., "Review and Extension of Compliance Information for Common Crack Growth Specimens," *Int. J. Fract.* 14, 453–468 (1978).

19. E. J. Ripling, "Proposed Test Method for Crack Arrest Fracture Toughness of Metallic Materials," unpublished.

20. G. T. Hahn et al., "Fast Fracture Toughness and Crack Arrest Toughness of Reactor Pressure Vessel Steel," pp. 289–320 in *Crack Arrest Methodology and Applications: A Symposium*, ASTM STP 711 (1980).

3. INVESTIGATION OF IRRADIATED MATERIALS

3.1 Fourth HSST Irradiation Series

R. G. Berggren T. N. Jones
W. R. Corwin J. W. Woods
R. K. Nanstad

Irradiation of the third capsule of this series was completed, and the capsule was disassembled. Dosimeter analysis is in progress. Irradiation of the fourth capsule in this series continued through the quarter with completion of the irradiation expected about the end of June 1982. Fast neutron fluence analyses for the first and second capsules were completed with exposures given in terms of dpa (displacements per atom) and neutrons of energies >1 and 0.1 MeV. For capsule A (A-533 grade B class 1 plate steel), the fast neutron fluences ranged from 7.9 to 27.3 x 10^{18} neutrons/cm^2 (E > 1 MeV) for the 1T compact specimens and from 7.5 to 23.0 x 10^{18} neutrons/cm^2 (E > 1 MeV) for Charpy V-notch specimens. For capsule B (submerged-arc weld metal), the fast neutron fluences ranged from 5.5 to 19.0 x 10^{18} neutrons/cm^2 (E > 1 MeV) and from 5.5 to 16.9 x 10^{18} neutrons/cm^2 (E > 1 MeV), respectively. A detailed test matrix for specimens from the first capsule and preliminary test matrices for specimens from the second and third capsules were prepared. The testing of specimens from these capsules will be divided between Engineering Systems Associates (ENSA) and ORNL.

A 110-kip MTS machine was installed in our hot cell and preparations for operation are in progress. Preparation of the Charpy impact test machine for reinstallation in our hot cell is in progress.

3.2 Irradiation-Induced K_{Ic} Curve Shift

R. G. Berggren R. K. Nanstad

The primary objective of this newly initiated program is to obtain valid fracture toughness for two nuclear pressure vessel materials, submerged-arc welds, irradiated at 288°C. The target radiation-induced transition temperature shift (ΔNDTT) is 85 K. The largest irradiated fracture toughness specimens will be 100 mm thick, permitting measurement of fracture toughness levels of 110 to 143 MPa$\cdot\sqrt{m}$. Smaller specimens, 50 and 25 mm thick will be used for lower toughness levels of the curve. Supporting the primary objective will be Charpy V-notch impact tests, tensile tests, K_J tests, and drop-weight tests.

Several options regarding materials, specimen types, and irradiation facilities are being considered on both technical and economic bases.

3.3 Irradiated Stainless Steel Cladding

R. G. Berggren R. K. Nanstad
W. R. Corwin

Specimen preparation is in progress for a study of irradiation effects on fracture toughness of stainless steel cladding. Types 309 and 308 weld overlay cladding have been deposited on the pressure vessel plate by the single-wire oscillating submerged-arc process. Three layers of weld deposit (one layer of type 309, followed by two layers of 308) were deposited to provide sufficient cladding thickness to fabricate Charpy V-notch, tensile, and 0.5T compact specimens from the cladding. This cladding is the same as that being used in part of the clad plate fracture program and accompanying cladding evaluation program.

We plan to irradiate cladding specimens at 288°C to fast neutron fluences of 1, 2, and 5 x 10^{19} neutrons/cm^2 (E > 1 MeV).

4. THERMAL-SHOCK INVESTIGATIONS

R. D. Cheverton S. K. Iskander
D. G. Ball Art Sauter

During this report period for the Thermal-Shock Program, a comparison was made of the TSE-5, -5A, and -6 toughness data and the American Society of Mechanical Engineers (ASME) Section XI toughness curves; preliminary thermal and fracture-mechanics calculations were made for TSE-8; a parametric analysis for overcooling accidents (OCAs) was completed; the effects of cladding on long flaws was included in the OCA-I code; and an investigation of the effects of azimuthal variations in temperature on K_I for long axial flaws was commenced.

4.1 Comparison of TSE-5, -5A, and -6 Toughness Data With the ASME Section XI K_{Ic} and K_{Ia} Curves

In Ref. 1 temperature-dependent curves representing the lower bound of 1T and 2T-CS K_J data and the average of lab K_{Ia} data obtained for the TSE-5, -5A, and -6 test cylinders and/or their prolongations were compared with the ASME Section XI K_{Ic} and K_{Ia} curves. This comparison showed that when normalized with T-RTNDT, the test-cylinder lab curves fell to the left of the ASME curves, indicating that the latter curves are conservative; that is, the ASME curves predict lower values of fracture toughness. However, not all of the lab K_J data represented by the lower-bound curves were valid in accordance with American Society for Testing and Materials (ASTM) E399 (Ref. 2) (the curves for TSE-5 and -6 were valid but not that for TSE-6). Another comparison can be made in which all of the data are valid, and this is done in Fig. 4.1, which compares the K_{Ic} and K_{Ia} values deduced from TSE-5, -5A, and -6 with the ASME Section XI K_{Ic} and K_{Ia} curves. Once again all of the experimental data fall to the left of the ASME curves.

4.2 Design of TSE-8

The purpose of thermal-shock experiment TSE-8 is to determine the effect of cladding on the behavior of a finite-length flaw that extends through the cladding into the base material. There is analytical and experimental evidence[3] indicating that in the absence of cladding and under thermal-shock loading conditions, a short flaw will extend along the surface to effectively become a long flaw, which has a greater potential than a short flaw for penetrating deep into the wall. The presence of the cladding tends to increase the stress-intensity factor, but the cladding material may have sufficient tearing resistance to prevent surface extension of the flaw.

Test conditions during TSE-5 were such that a very short and shallow flaw extended to become a long flaw and in the process penetrated 40% of

ORNL-DWG 82-4631 ETD

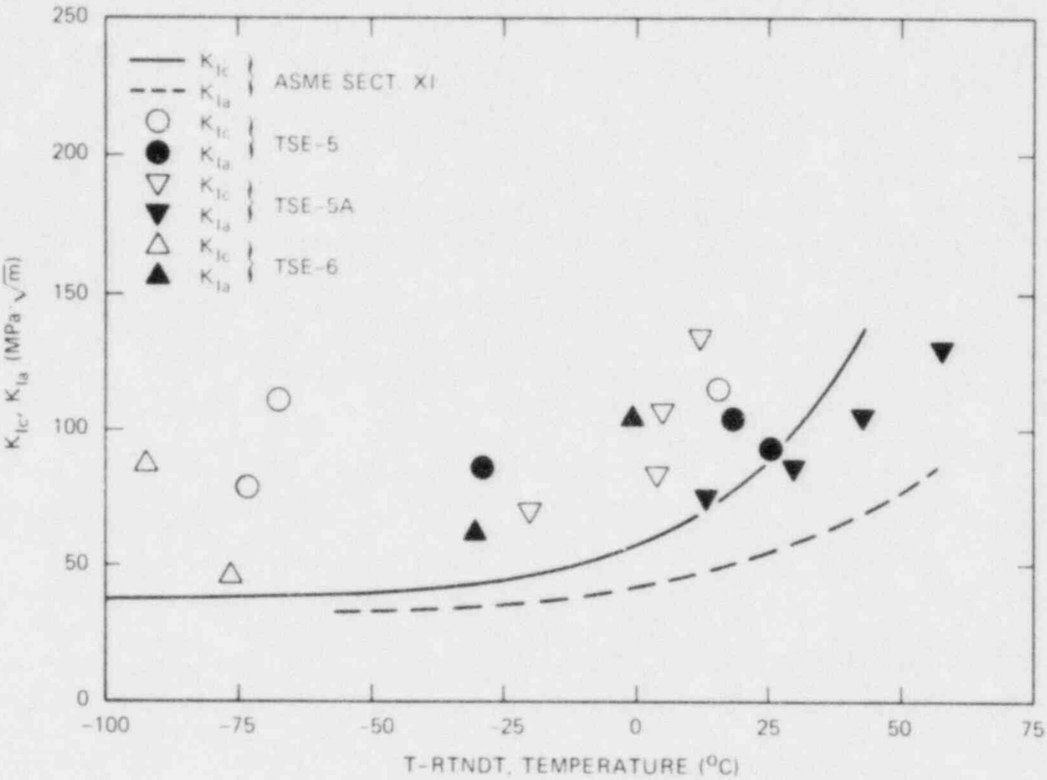

Fig. 4.1. Comparison of K_{Ic} and K_{Ia} data deduced from TSE-5, -5A, and -6 with the ASME Section XI K_{Ic} and K_{Ia} vs T-RTNDT curves.

the wall.[3] However, the addition of cladding to the inner surface of the test cylinder would reduce the heat transfer rate from the cylinder to the coolant and thus also would reduce the thermal stresses, introducing the possibility of not being able to achieve a sufficient potential for crack propagation. To investigate this possibility, thermal and fracture-mechanics calculations were made with and without cladding, using the temperature-dependent fluid-film heat transfer coefficient and fracture toughness data deduced from TSE-5. Both the K_I and K_I/K_{Ic} values for shallow ($a/w < 0.2$), long axial flaws were slightly greater for the cylinder with cladding and were only slightly less for deeper flaws. Thus, the enhancement in K_I due to the difference in the coefficient of thermal expansion between the cladding and base material more than offsets the decrease in K_I/K_{Ic} due to the reduced severity of the thermal shock that is brought about by the addition of the cladding. Based on this information, the tentative conclusion is that TSE-8 can be conducted satisfactorily.

4.3 Overcooling Accident Parametric Study

A parametric study of OCAs was discussed in Ref. 4. This study has been completed and is summarized herein; a complete account of the study will be published soon.[5]

The purpose of the parametric study is to provide a handbook assessment capability for estimating permissible vessel lifetimes for specified primary-system thermal-pressure transients, assuming long axial inner-surface flaws to exist.

The transients included in the analysis consist of an exponential decay of the primary-system coolant temperature, a constant heat transfer coefficient for the fluid film at the coolant-vessel interface, and a constant primary-system pressure. The coolant temperature transient is described mathematically as

$$T_B = T_f + (T_i - T_f)\, e^{-nt} , \tag{1}$$

where

T_B = temperature of primary-system coolant in downcomer,
T_f = final (asymptotic) temperature of primary-system coolant in downcomer,
T_i = initial temperature of primary-system coolant in downcomer,
t = time in transient,
n = exponential decay constant.

The six exponential decay constants for the thermal transients range from 1.5×10^{-2} to 1.5×10^{-1} min^{-1}; there are two asymptotic temperatures (66 and 121°C) and a single initial temperature (288°C) for the coolant and vessel. Graphical representations of these thermal transients are shown in Figs. 4.2 and 4.3.

The heat transfer coefficient (1870 $W \cdot m^{-2} \cdot K^{-1}$) includes the thermal resistance of the cladding as well as that of the fluid film, and the latter resistance corresponds to a flow rate that is achieved with the main coolant pumps running. The time-independent pressures included in the analysis range from zero to 17.2 MPa in 1.72-MPa increments.

In addition to this range of transients, the pressurized-water reactor loss-of-coolant accident (PWR LOCA) transient is also included. For this case the exponential decay constant for the coolant temperature is infinity (step change in coolant temperatures), the initial and final temperatures are 288 and 21°C, respectively, and the heat transfer coefficient is 1140 $W \cdot m^{-2} \cdot K^{-1}$, which corresponds to the emergency-core-cooling system (ECCS) flow rate (main pumps off). Although it may not be of any practical significance, the LOCA case was calculated using the same range of constant pressures as for the other transients.

Other basic input to the analysis includes a single value of the initial RTNDT (4°C), three copper concentrations (0.10, 0.20, and 0.35%), and twelve values of the inner-surface fluence ranging from 0.25 to 5.0×10^{19} neutrons/cm^2. For all cases calculations were made for the first 2 h of the transient. All parameters included in the analysis are

ORNL-DWG 82-5773 ETD

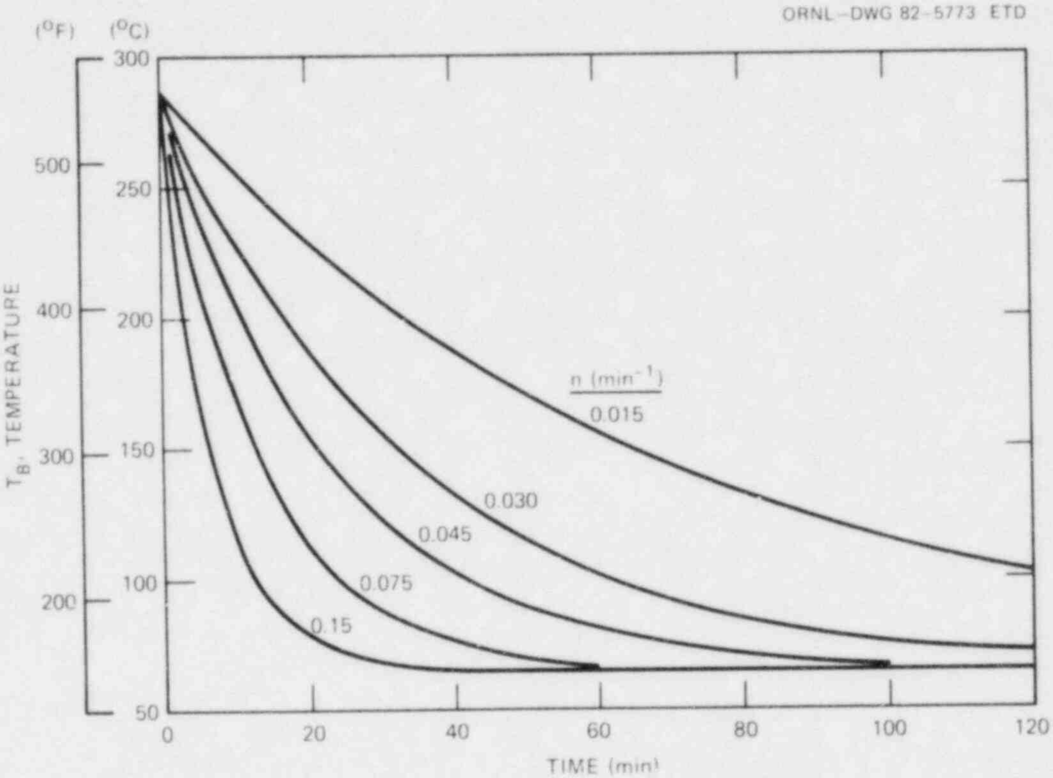

Fig. 4.2. Exponential temperature transients with T_f = 65.6°C.

ORNL-DWG 82-5774 ETD

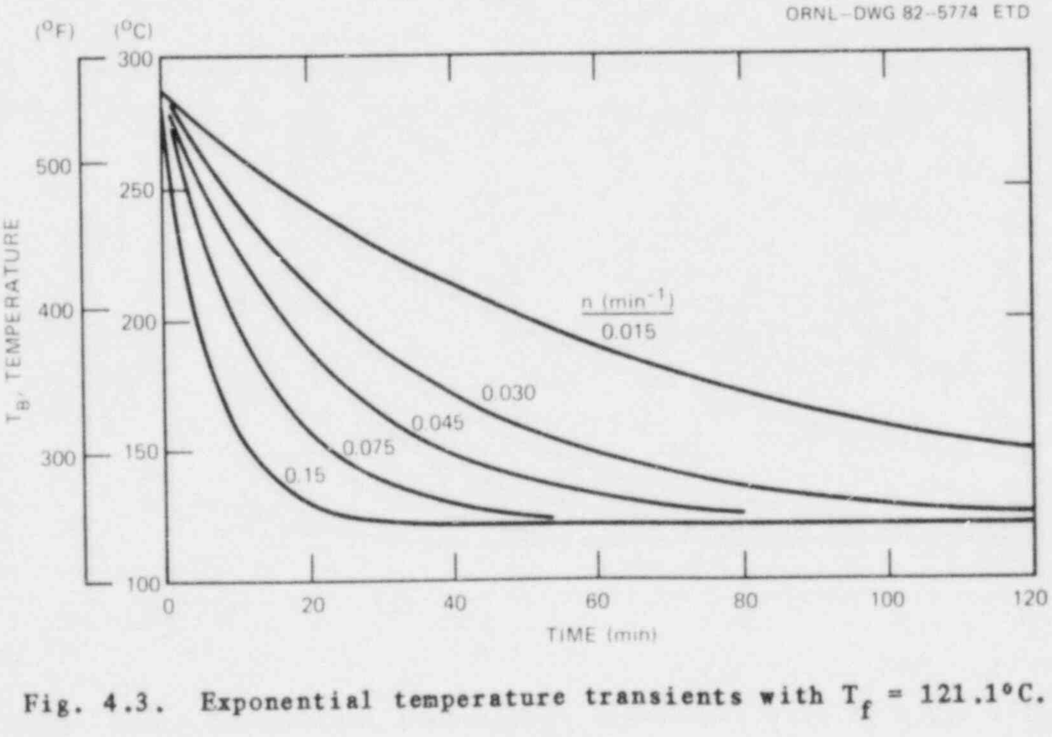

Fig. 4.3. Exponential temperature transients with T_f = 121.1°C.

summarized in Table 4.1, and a summary description of the calculational model is included in Table 4.2 (Refs. 6–8).

The integrity of the vessel during the OCA is evaluated on the basis of the calculated behavior of a long axial inner-surface flaw, using linear-elastic fracture mechanics and ignoring the effects of cladding other than its thermal resistance. The effect of cladding, aside from

Table 4.1. Parameters and values thereof included in the OCA parametric analysis

Parameter	Value
T_b (coolant temperature)[a]	$T_b = T_f + (T_i - T_f)e^{-nt}$
T_i (initial temperature),[a] °C	288
T_f (final temperature),[a] °C	21,[b] 66, 121
n, min^{-1}	∞,[b] 1.5×10^{-2} to 1.5×10^{-1}
t (max), h	2
h (surface conductance), $W \cdot m^{-2} \cdot K^{-1}$	1140,[b] 300
p (primary-systems pressure), MPa	17.2
F (fast-neutron fluence), neutrons/cm^2	0.25 to 5.0×10^{19}
$RTNDT_o$, °C	4
Copper concentrations, wt %	0.10, 0.20, 0.35

[a]Temperatures are of coolant in reactor-vessel downcomer.
[b]These values apply to the large-break LOCA only.

Table 4.2. Summary description of OCA calculational model

Parameter	Value
Vessel dimensions, m	
Outside diameter	4.80
Inside diameter	4.37
Flaw	Long, axial, inner-surface
Flaw depth, fraction of wall (a/w)	0.02–0.95
Fracture-mechanics analysis	LEFM (OCA-I) (Ref. 6)
K_{Ic} and K_{Ia} (source)	ASME Section XI (Ref. 7)
ΔRTNDT (source)	Regulatory Guide 1.99 (Ref. 8)

its thermal resistance and assuming the flaw to extend through the cladding, is to increase K_I somewhat, particularly for shallow flaws.[9]

Results of analysis. For many of the cases calculated crack arrest did not take place before the tip of the crack encountered upper shelf temperature. Thus, as indicated in Fig. 4.4, the fracture mode presumably would change from cleavage to ductile tearing as the flaw propagated into the wall, and for arrest to take place the tearing resistance of the material would have to be sufficient. For the purpose of this report it was assumed that crack arrest would not take place if $K_I \geq 220$ MPa·$\sqrt{m}$ before $K_I = K_{Ia}$.

To summarize some of the data in graphical form the fluences corresponding to incipient initiation and incipient failure, assuming warm prestressing (WPS) to be effective, were plotted as a function of primary-system pressure (see Figs. 4.5–4.9) failure. Figure 4.5 corresponds to the LOCA, while each of the other figures summarizes results related to

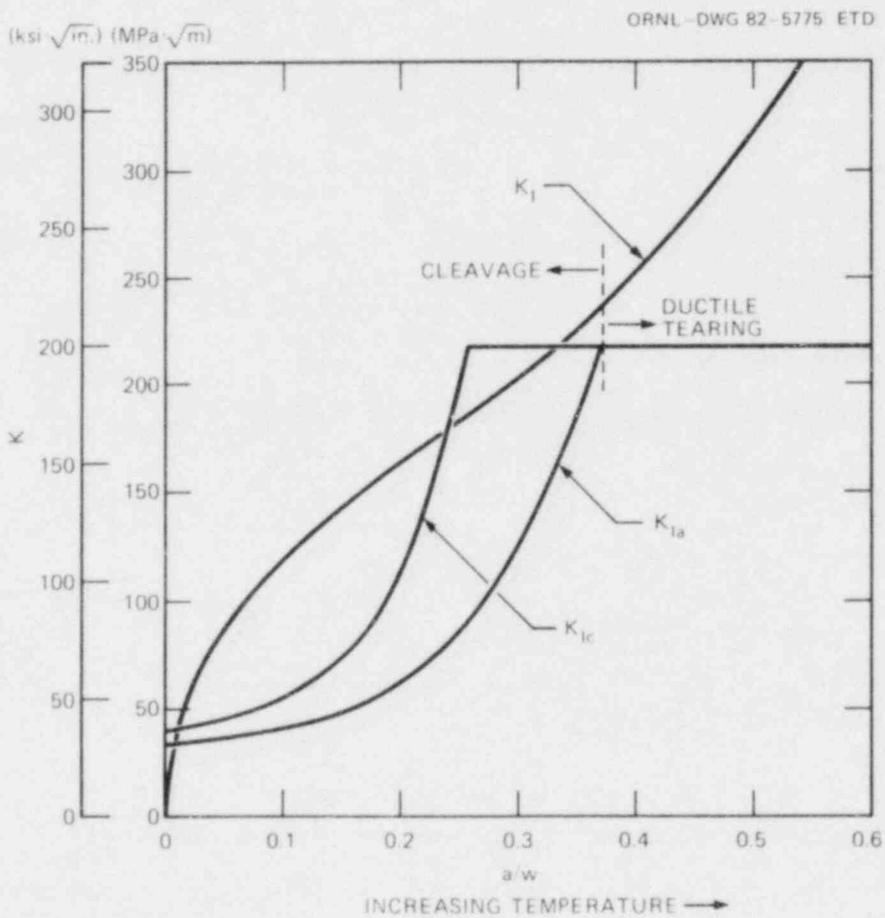

Fig. 4.4. K_I, K_{Ic}, K_{Ia} vs a/w for $n = 15 \times 10^{-3}$ mm^{-1}, $T_f = 65.6°C$, p = 6.89 MPa, Cu = 0.35%, $F_o = 1 \times 10$ neutrons·cm^{-2}, t = 16 min.

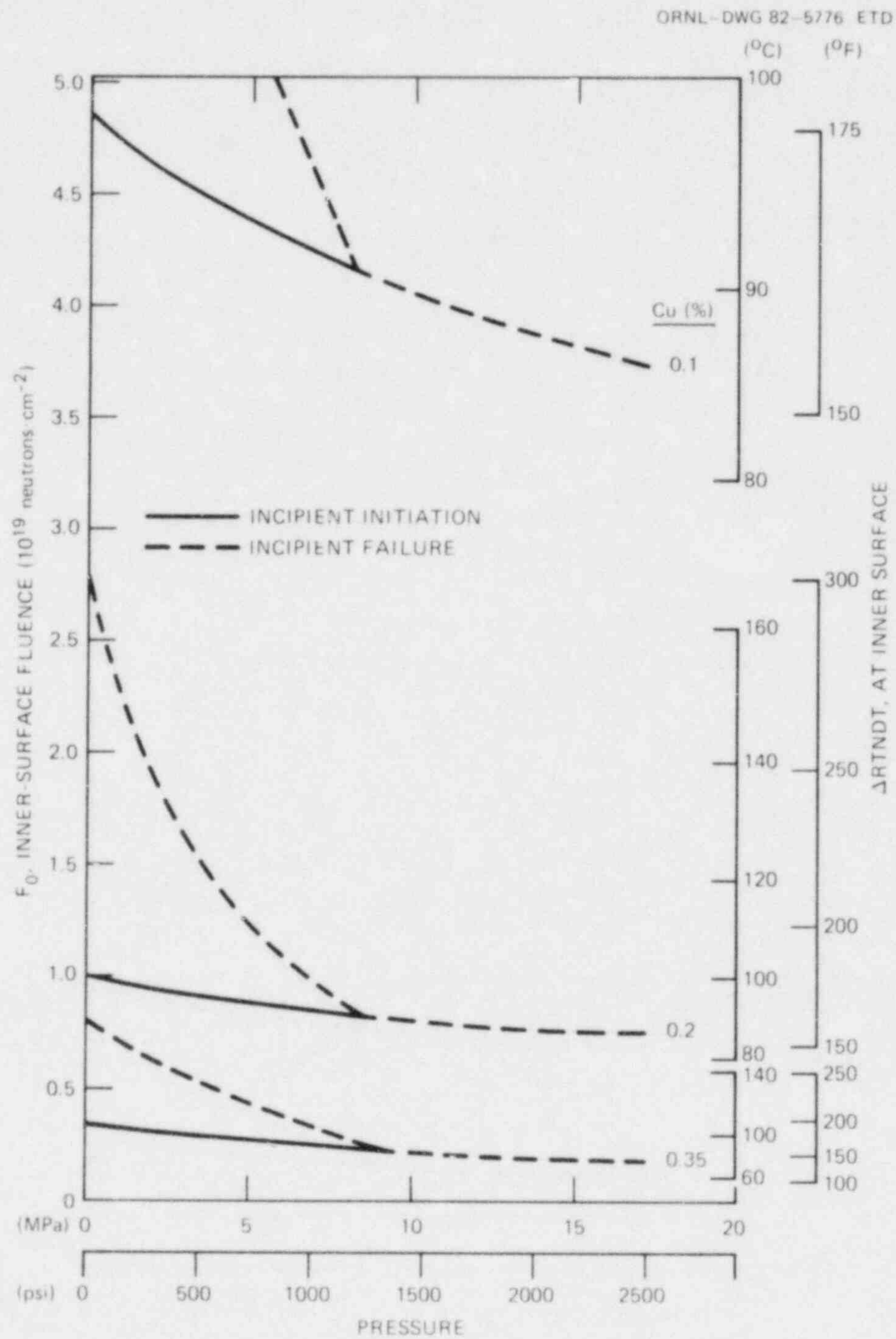

Fig. 4.5. Fluences corresponding to incipient initiation and incipient failure, assuming WPS to be effective, vs primary-system pressure and various parameters pertaining to a thermal transient. LOCA with Cu = 0.1, 0.2, 0.35%.

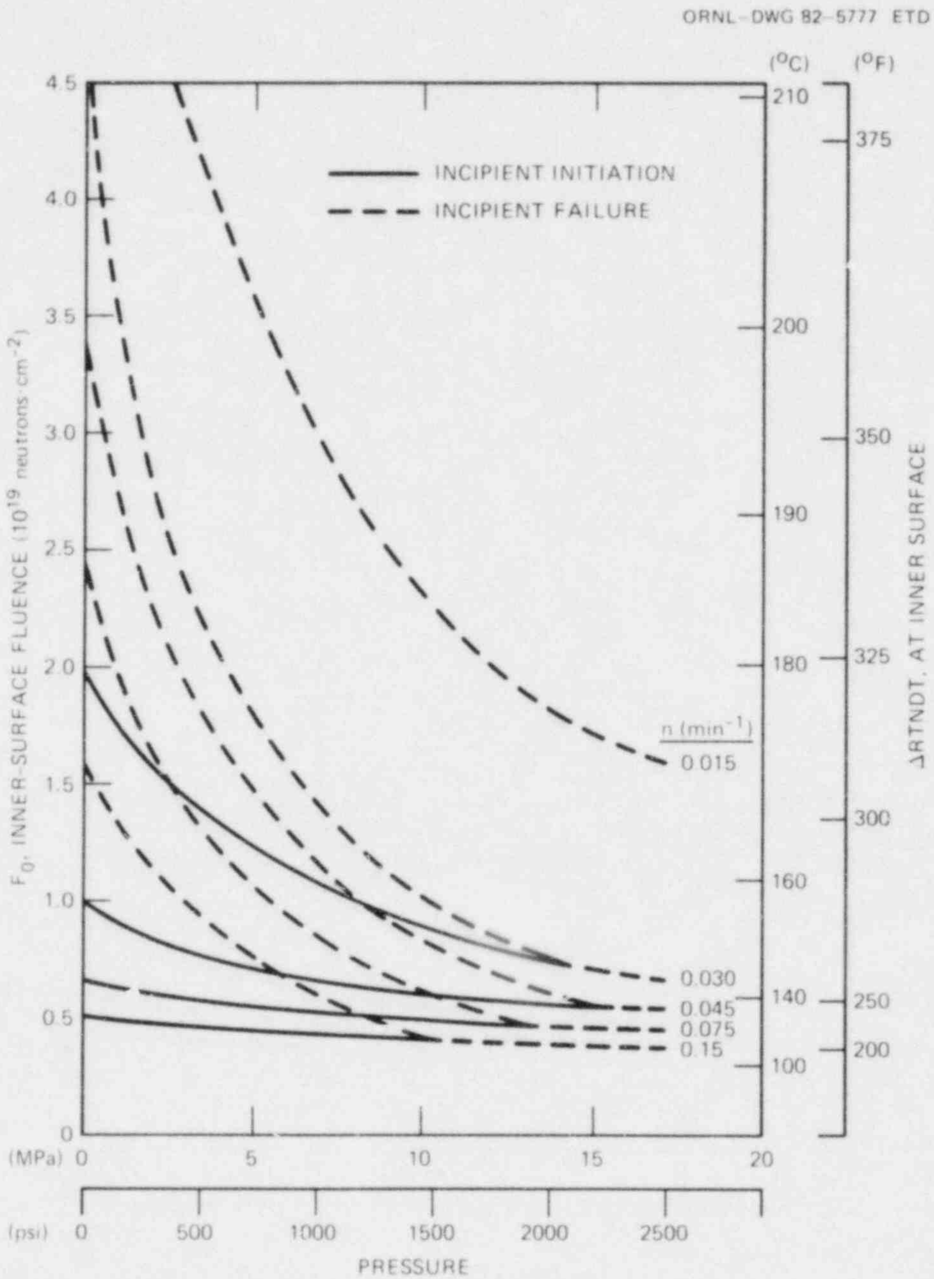

Fig. 4.6. Fluences corresponding to incipient initiation and incipient failure, assuming WPS to be effective, vs primary-system pressure and various parameters pertaining to a thermal transient. Cu = 0.35%, T_f = 65.6°C.

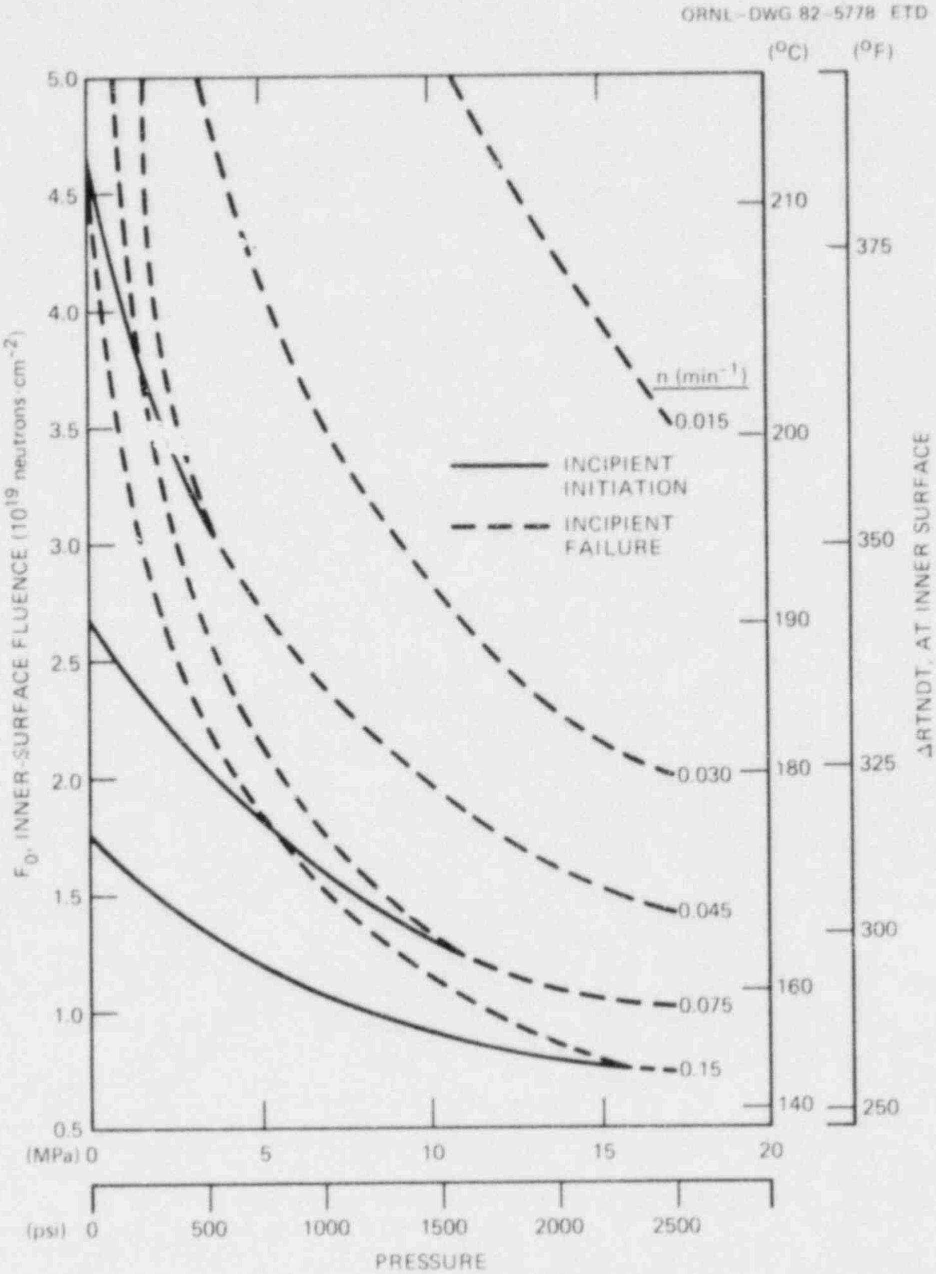

Fig. 4.7. Fluences corresponding to incipient initiation and incipient failure, assuming WPS to be effective, vs primary-system pressure and various parameters pertaining to a thermal transient. Cu = 0.35%, T_f = 121.1°C.

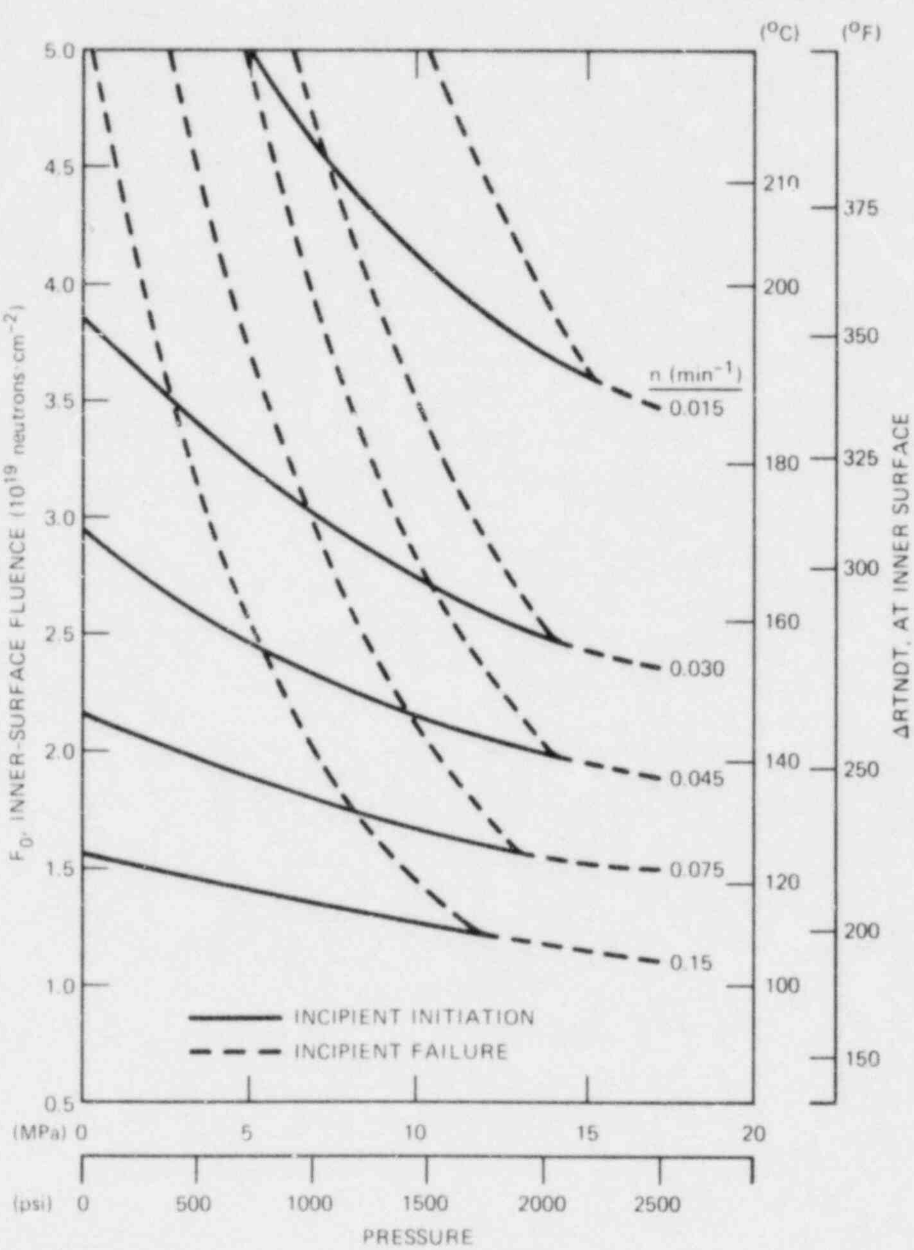

Fig. 4.8. Fluences corresponding to incipient initiation and incipient failure, assuming WPS to be effective, vs primary–system pressure and various parameters pertaining to a thermal transient. Cu = 0.20%, T_f = 65.6°C.

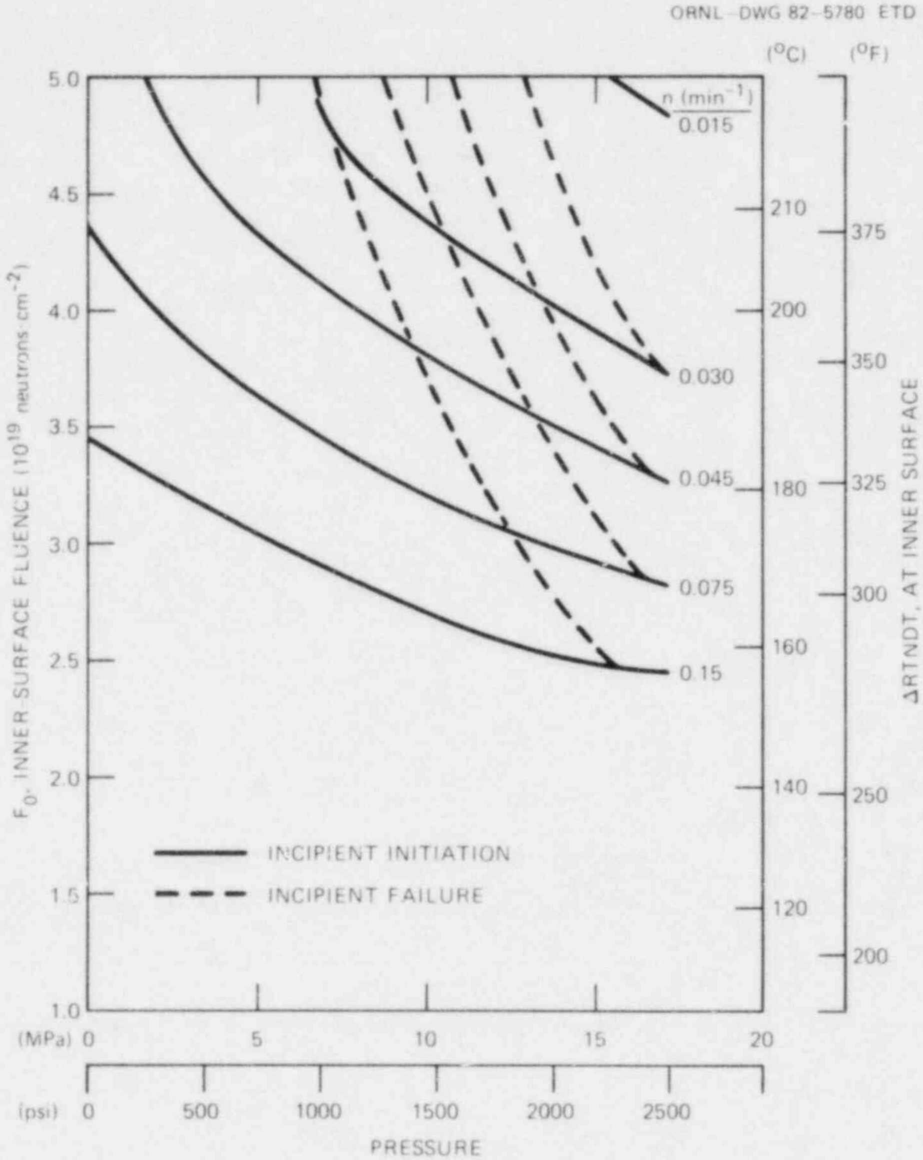

Fig. 4.9. Fluences corresponding to incipient initiation and incipient failure, assuming WPS to be effective, vs primary-system pressure and various parameters pertaining to a thermal transient. Cu = 0.20%, T_f = 121.1°C.

the five thermal decay constants, each figure corresponding to a combination of copper concentration and asymptotic temperature T_f. In each figure the solid line represents incipient initiation and the dashed line represents incipient failure. Beyond the point where the two curves come together and for those transients for which no solid curve is shown, incipient initiation results in failure. As indicated by the figures this condition is more likely to exist with high pressure and the less severe thermal transients.

With the exception of the LOCA, cases with a copper concentration of 0.1% did not result in crack initiation; thus, no figures are included for these cases (Cu = 0.1%). For all other cases, including the LOCA with 0.1% copper, crack initiation does take place over some portion of the range of pressures considered.

As indicated by the expressed intent of the study, the curves in Figs. 4.5–4.9 can be used to estimate the fluences corresponding to incipient initiation and incipient failure, assuming WPS to be effective. Additional data concerning critical fluences can be derived from the critical-crack-depth curves and the K_I vs time curves that will be included in the final report.

4.4 Modification of OCA-1 for Application to Clad Reactor Pressure Vessel

Art Sauter

The extension of the OCA-I computer code[6] for taking into account the effects of cladding was prompted by a growing interest in the influence of a cladding layer on the initiation and arrest of a surface flaw in reactor pressure vessels (RPVs) during OCAs.

Because of the ability of the OCA-1-1R temperature code to deal with different material properties through the wall thickness of the cylinder under consideration, only the fracture mechanics part of the code needed to be modified accordingly.

In addition, provisions were made for consideration of existing residual stresses in the clad structure prior to the transient.

4.4.1 Method of analysis

The procedure to obtain the K_I distribution over the wall thickness ought to remain the same as before;[10] that is, a superposition technique proposed by Bueckner,[11] which uses the stress distribution in the uncracked structure together with K_I solutions for unit loads along the surface of the crack under consideration. This leads to the stress distribution across the wall thickness as the only part of the code which had to be reformulated (Fig. 4.10).

The method chosen to obtain an analytical solution for the stress distribution throughout the entire wall thickness is a linear superposition of the solutions for two separately analyzed cylindrical structures, which represent the clad part and the base material part of the RPV.

To get a compatible solution one has to fulfill two boundary conditions:

1. The radial position of the outer surface of the inner cylinder has to be the same as the position of the inner surface of the outer cylinder.
2. The axial strains have to be constant across the entire wall thickness.

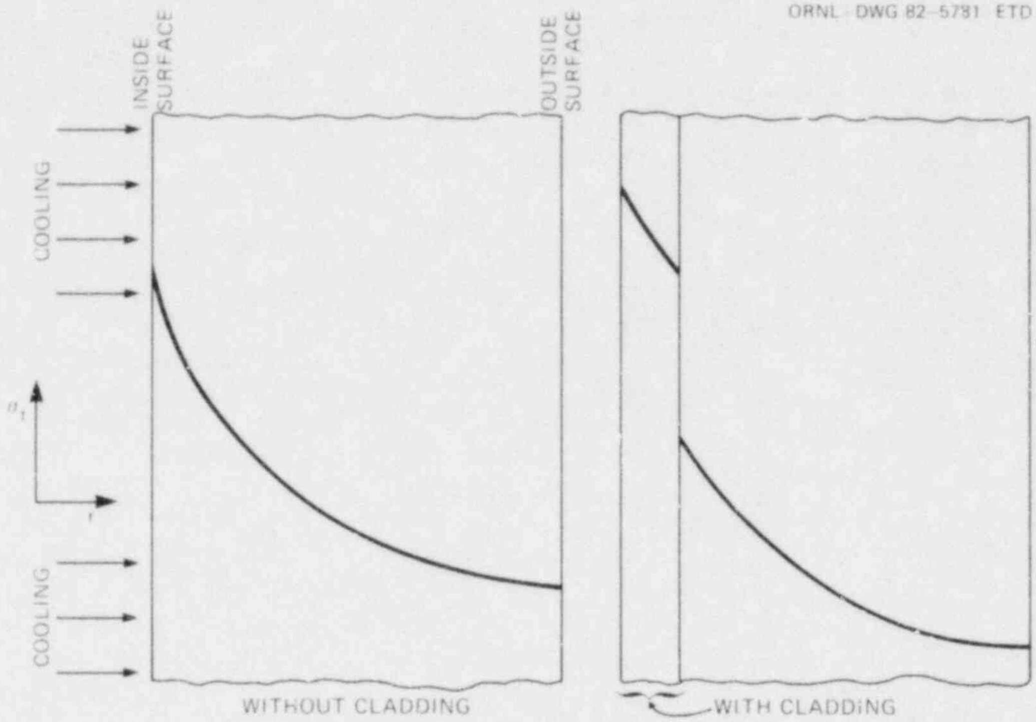

Fig. 4.10. Typical distribution of circumferential stress across the wall thickness of a cylinder for a temperature transient without mechanical load.

The first condition is achieved by applying an additional surface pressure on both cylinders acting at the interface between them. Its magnitude and direction (tension or compression) have to be chosen so that the resulting radial displacements satisfy the compatibility condition.

The second requirement is achieved by solving for two forces with opposite signs at the ends of the cylinders which satisfy the equilibrium of forces and moments and provide the compatibility of axial expansion between the cylinders. They are applied in the form of a second interface pressure. The complete process is graphically shown in Fig. 4.11.

4.4.2 Solution

Steps in solution. With these conditions in mind the calculational procedure is as follows:

1. Solving for the stress distribution and the axial and circumferential strain according to the temperature profile in each separate cylinder.
2. Calculation of the interface pressure which accomplishes the displacement compatibility.
3. Evaluation of the axial deformations (contraction in one and extension in the other cylinder) produced by the additional interface pressure of step 2, and adding them to the axial strain of step 1.

ORNL-DWG 82-5782 ETD

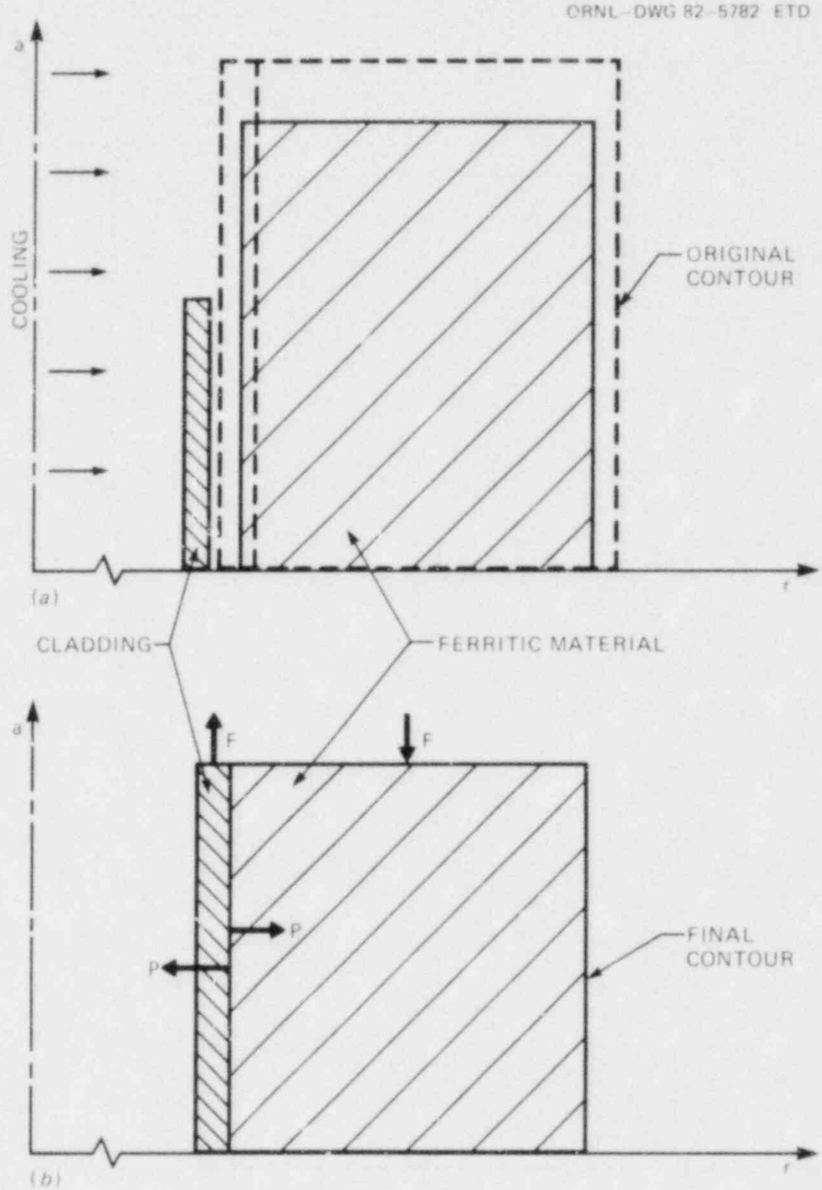

Fig. 4.11. Method of analysis for a cool-down process on the inner surface of a cylinder: cylinder boundaries (a) before and (b) after compatibility conditions are imposed.

4. From the difference in axial straining between the two cylinders an equilibrium force can be solved for, which provides a constant axial strain in both cylinders (Fig. 4.12).
5. Applying these forces results again in a violation of the displacement condition. Therefore, a second additional interface pressure has to be found which equilibrates the circumferential strain on the outer surface of the inner cylinder with the one on the inner surface of the outer cylinder at the same time as it reverses the axial

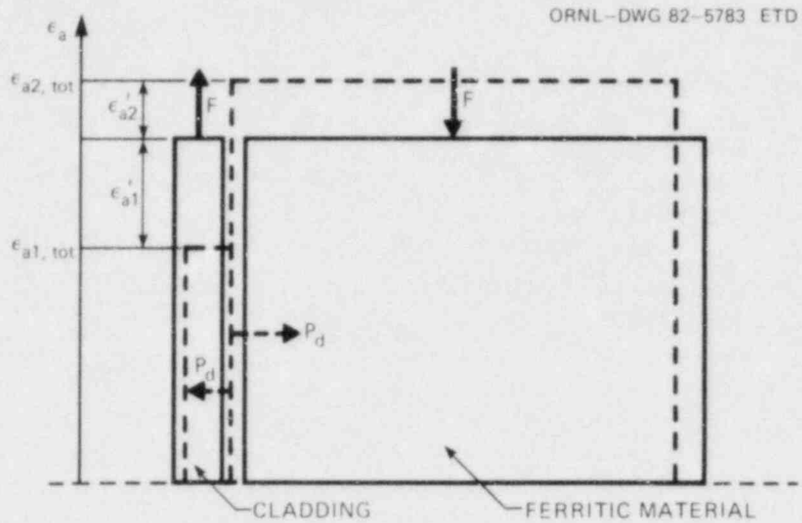

Fig. 4.12. Diagram of axial strains for solving step 4 [Eq. (13)].

strains produced by the end forces. The additional axial strains caused by this second interface pressure in both cylinders have also to be taken into account so that the axial strain compatibility remains unviolated (Fig. 4.13).

6. The stress distribution resulting from the total interface pressure is added to the stress distribution produced by the temperature gradient alone, which was computed in step 1.

<u>Initial temperature</u>. In a single-material cylinder, stresses produced by a temperature gradient over the wall thickness are independent

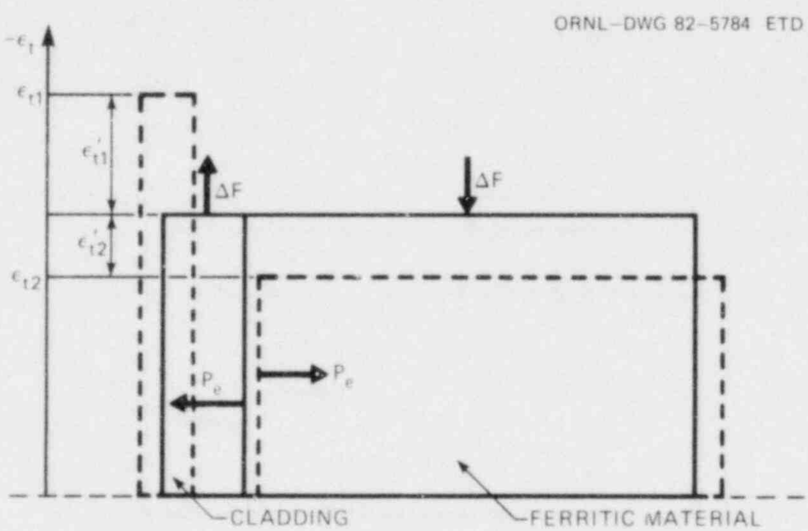

Fig. 4.13. Diagram of circumferential strains for solving step 5 [Eq. (18)] at $r = b_1 = a_2$.

of a reference temperature because any temperature condition at the surfaces of the cylinder may be obtained by superposing a uniform heating or cooling, which does not produce stresses. In the analysis of a cylinder consisting of two different materials, it is necessary to define a temperature from which the calculation is started. Therefore, an initial temperature was introduced into the formulation. Thus, heating would lead to positive strains and cooling would result in negative strains, according to the initial temperature (i.e., $\Delta t = t - t_{initial}$).

Equations. Because only long axial flaws are considered at present, only the circumferential stresses will be given herein.

The nomenclature referred to in the following discussion is listed in Table 4.3.

Step 1: The axial strain in a homogeneous cylinder caused by a temperature gradient is[12]

$$\bar{\varepsilon}_a = \frac{2\alpha}{b^2 - a^2} \int_a^b tr\ dr \ . \tag{2}$$

On the surfaces the circumferential strain $\bar{\varepsilon}_t$ is equal to the axial strain $\bar{\varepsilon}_a$. The circumferential stress in a homogeneous cylinder caused by a temperature gradient is[13]

$$\bar{\sigma}_t = \frac{E \cdot \alpha}{(1 - \mu)} \frac{1}{r^2} \left[\int_a^r tr\ dr + \frac{(r^2 + a^2)}{(b^2 - a^2)} \int_a^b tr\ dr - r^2 t \right] . \tag{3}$$

Step 2: To solve for an interface pressure that accomplishes the radial displacement compatibility at the interface between the two cylinders, one has to satisfy

$$\left(U_1,T + U_1,p\right) r{=}b_1 = \left(U_2T + U_2p\right) r{=}a_2 \ . \tag{4}$$

The four terms in Eq. (4) can be found to be

$$\begin{aligned} U_1,T &= \frac{2\ \alpha_1\ b_1}{b_1^2 - a_1^2} \int_{a_1}^{b_1} tr\ dr \\ U_2,T &= \frac{2\ \alpha_2\ a_2}{b_2^2 - a_2^2} \int_{a_2}^{b_2} tr\ dr \end{aligned} \tag{5}$$

Table 4.3. Nomenclature used in Section 4.4

$\bar{\varepsilon}$ = strains caused by thermal loading in a homogeneous cylinder

$\bar{\sigma}$ = stresses caused by a thermal loading in a homogeneous cylinder

ε = strains caused by mechanical loading

σ = stresses caused by mechanical loading

r = radial distance

t = temperature in wall at r at a specific time in the transient

a = inside radius of a cylinder

b = outside radius of a cylinder

E = Young's modulus (independent of temperature)

μ = Poisson's ratio (independent of temperature)

α = coefficient of thermal expansion (independent of temperature)

P = pressure acting in the interface between the two cylinders

U = radial displacement

F = force at the end of a cylinder

Indices are:

a	for "axial"
t	for "circumferential"
1	for "inner cylinder" (representing the cladding)
2	for "outer cylinder" (representing the ferritic part of the RPV)
tot	for "thermal + mechanical"
T	for "caused by temperature"
p	for "caused by interface pressure"
d	for "displacement condition"
e	for "end condition"
res	for "resulting"

$$U_{1,p} = -\frac{P_d\ b_1}{E_1}\left[(1-\mu_1)\frac{b_1^2}{(b_1^2-a_1^2)} + (1+\mu_1)\frac{a_1^2}{b_1^2-a_1^2}\right]$$

$$U_{2,p} = \frac{P_d\ a_2}{E_2}\left[(1-\mu_2)\frac{a_2^2}{(b_2^2-a_2^2)} + (1+\mu_2)\frac{b_2^2}{b_2^2-a_2^2}\right] \tag{6}$$

with Eqs. (5) and (6) in Eq. (4) and solving for P_d with $b_1 = a_2$:

$$P_d = \frac{\frac{2\alpha_1}{b_1^2-a_1^2}\int_{a_1}^{b_1} tr\ dr - \frac{2\alpha_2}{b_2^2-a_2^2}\int_{a_2}^{b_2} tr\ dr}{D}$$

where

$$D = \frac{(1-\mu_2)}{E_2}\frac{a_2^2}{(b_2^2-a_2^2)} + \frac{(1+\mu_2)}{E_2}\frac{b_2^2}{(b_2^2-a_2^2)} + \frac{(1-\mu_1)}{E_1}\frac{b_1^2}{(b_1^2-a_1^2)} + \frac{(1+\mu_1)}{E_1}\frac{a_1^2}{(b_1^2-a_1^2)}\ . \tag{7}$$

<u>Step 3</u>: Deformations caused by P_d are:

$$\left(\varepsilon_{t_1p}\right)_{r=b_1} = -\frac{P_d}{E_1}\frac{(1-\mu_1)\ b_1^2 + (1+\mu_1)a_1^2}{(b_1^2-a_1^2)}$$

$$\left(\varepsilon_{t_2p}\right)_{r=a_2} = \frac{P_d}{E_2}\frac{(1-\mu_2)\ a_2^2 + (1+\mu_2)b_2^2}{(b_2^2-a_2^2)} \tag{8}$$

$$\varepsilon_{a_1p} = -\mu_1\ \varepsilon_{t_1p}$$

$$\varepsilon_{a_2p} = -\mu_2\ \varepsilon_{t_2p} \tag{9}$$

Step 4: With

$$\varepsilon_{a_1,tot} = \bar{\varepsilon}_{a_1} + \varepsilon_{a_1 p}$$
$$\varepsilon_{a_2,tot} = \bar{\varepsilon}_{a_2} + \varepsilon_{a_2 p} \tag{10}$$

and

$$\varepsilon'_{a_1} = \frac{F}{\pi\ E_1(b_1^2 - a_1^2)}$$
$$\varepsilon'_{a_2} = \frac{-F}{\pi\ E_2(b_2^2 - a_2^2)} \tag{11}$$

one finds

$$\Delta\varepsilon_{a,tot} = \varepsilon_{a_1,tot} - \varepsilon_{a_2,tot} = \varepsilon'_{a_1} - \varepsilon'_{a_2}\ . \tag{12}$$

Solving with Eq. (11) for

$$\Delta\varepsilon_{a,tot} = \frac{F}{\pi}\left[\frac{1}{E_1(b_1^2 - a_1^2)} + \frac{1}{E_2(b_2^2 - a_2^2)}\right] \tag{13}$$

leads to

$$F = \frac{\pi\ \Delta\varepsilon_{a,tot}}{\dfrac{1}{E_1(b_1^2 - a_1^2)} + \dfrac{1}{E_2(b_2^2 - a_2^2)}}\ . \tag{14}$$

Step 5: At this point while solving for the second interface pressure P_e, an assumption is made that is a simplification of the solution method as long as $\mu_1 = \mu_2$. To keep the axial strains equal in both cylinders even after applying P_e, an additional end force ΔF was applied which produces additional axial strains $\Delta\varepsilon_a$ such that under the pressure load of P_e, the cylinder ends would be still at the same position that existed before applying ΔF and P_e:

$$\Delta\varepsilon_{a_1} = \frac{\Delta F}{\pi\ E_1(b_1^2 - a_1^2)}$$

and

$$\Delta\varepsilon_{a_2} = \frac{\Delta F}{\pi\, E_2 (b_2^2 - a_2^2)} \quad .$$

Given these assumptions, a solution can be obtained for P_e, keeping in mind that P_e results in ε_{t_1} in cylinder 1 and ε_{t_2} in cylinder 2;

$$\Delta\varepsilon_{a_1} = \mu_1 \; \varepsilon_{t_1}$$

and

$$\Delta\varepsilon_{a_2} = \mu_2 \; \varepsilon_{t_2} \; ,$$

therefore

$$\varepsilon_{t_1} = - \mu_1 \; \varepsilon'_{a_1} + (-\mu_1)\; (-\mu_1 \varepsilon_{t_1})$$

$$= - \mu_1 \; \varepsilon'_{a_1} + \mu_1^2 \varepsilon_{t_1}^{\;2}$$

and

$$\varepsilon_{t_2} = - \mu_2 \; \varepsilon'_{a_2} + \mu_2^2 \varepsilon_{t_2}^{\;2} \; .$$

The difference in circumferential strains becomes now

$$\left(\varepsilon_{t_1}\right)_{r=b_1} = - \frac{\mu_1 \; \varepsilon'_{a_1}}{(1 - \mu_1^2)} \; , \qquad (15)$$

$$\left(\varepsilon_{t_2}\right)_{r=a_2} = - \frac{\mu_2 \; \varepsilon'_{a_2}}{(1 - \mu_2^2)} \; ,$$

$$\Delta\varepsilon_t = \varepsilon_{t_1} - \varepsilon_{t_2} = \varepsilon'_{t_1} - \varepsilon'_{t_2} \; , \qquad (16)$$

with P_e for P_d in Eq. (8) and with Eq. (16)

$$-\frac{\varepsilon'_{t_1}}{\varepsilon'_{t_1} - \Delta\varepsilon_t} = \frac{E_2(b_2^2 - a_2^2)\left[(1-\mu_1)b_1^2 + (1+\mu_1)a_1^2\right]}{E_1(b_1^2 - a_1^2)\left[(1-\mu_2)a_2^2 + (1+\mu_2)b_2^2\right]} . \tag{17}$$

With K = the right side of Eq. (17) one finds that

$$\varepsilon'_{t_1} = \frac{\Delta\varepsilon_t \, K}{1 + K} \tag{18}$$

and

$$P_e = -\frac{\varepsilon'_{t_1} E_1 (b_1^2 - a_1^2)}{(1-\mu_1)b_1^2 + (1+\mu_1)a_1^2} . \tag{19}$$

Step 6: With

$$P_{res} = P_d + P_e$$

the stress distribution fulfilling the boundary conditions becomes

$$\sigma_{t_1} = -P_{res}\frac{b_1^2}{(b_1^2 - a_1^2)}\left(1 + \frac{a_1^2}{r^2}\right)$$

$$\sigma_{t_2} = P_{res}\frac{a_2^2}{(b_2^2 - a_2^2)}\left(1 + \frac{b_2^2}{r^2}\right) \tag{20}$$

and the resulting stress distribution across the weld thickness of the clad cylinder comes out to be [with Eqs. (3) and (20)]

$$\sigma_{t_1,res} = \bar{\sigma}_{t_1} + \sigma_{t_1} ,$$

$$\sigma_{t_2,res} = \bar{\sigma}_{t_2} + \sigma_{t_2} . \tag{21}$$

Residual stresses. When the cladding option in the modified code is used. a possibility is provided to specify residual stresses throughout the wall thickness. These stress values have to be given at every single crack depth used in the calculation. The user has to provide a residual stress that is self-equilibrating.

The specified residual stress values will be added to the stress values computed by the code at every single crack depth value.

4.4.3 Use of modified code

If no cladding analysis is required, the only change to the input file would be the switch parameter on card 1 (referring to Ref. 6, p. 35), which has to be added after the last parameter given there. It initiates the cladding analysis in case of a positive value and does not in case of a zero or negative value.

For a cladding analysis to be conducted, two more cards have to be added after card 4.0 (Ref. 6, p. 38). The first card contains four numbers:

1. Number of clad elements in the finite-element (FE) grid geometry; the grid geometry is a fixed input resulting from the temperature analysis with OCA-1-1R (Ref. 6, p. 29). In specifying the number of clad elements, the thickness of the cladding layer will be determined.
2. Young's modulus of the cladding material.
3. Poisson's ratio of the cladding material.
4. Coefficient of expansion of the cladding material.

The first number on the second additional card specified the number of residual stress values to be given. It is followed by these values.

An additional number is also to specify on card 2.0 (Ref. 6, p. 36) following the variable "CONS." It specifies the initial temperature.

All additional input can be made in the so-called "free field input" (Ref. 6, p. 22). Default values are not provided. This means each number has to be specified, separated either by a comma or a blank.

4.4.4 Sample results

Cladding effect. To demonstrate the influence of cladding on a fracture mechanics analysis with OCA-I, a large-break LOCA transient was calculated with and without a cladding layer in the RPV, whereas the input temperature distributions have been the same in both cases (cladding effect was included in the temperature analysis).

The only difference in the material properties used in the calculations was established in the coefficient of thermal expansion for austenitic and ferritic material, which has been taken to be 10^{-5} K^{-1} and 8×10^{-6} K^{-1}, respectively.

The K_I distributions with respect to time and crack depths are compared in Figs. 4.14–4.17 for a fluence of 4.0×10^{19} neutrons/cm^2, an

ORNL-DWG 82-5785 ETD

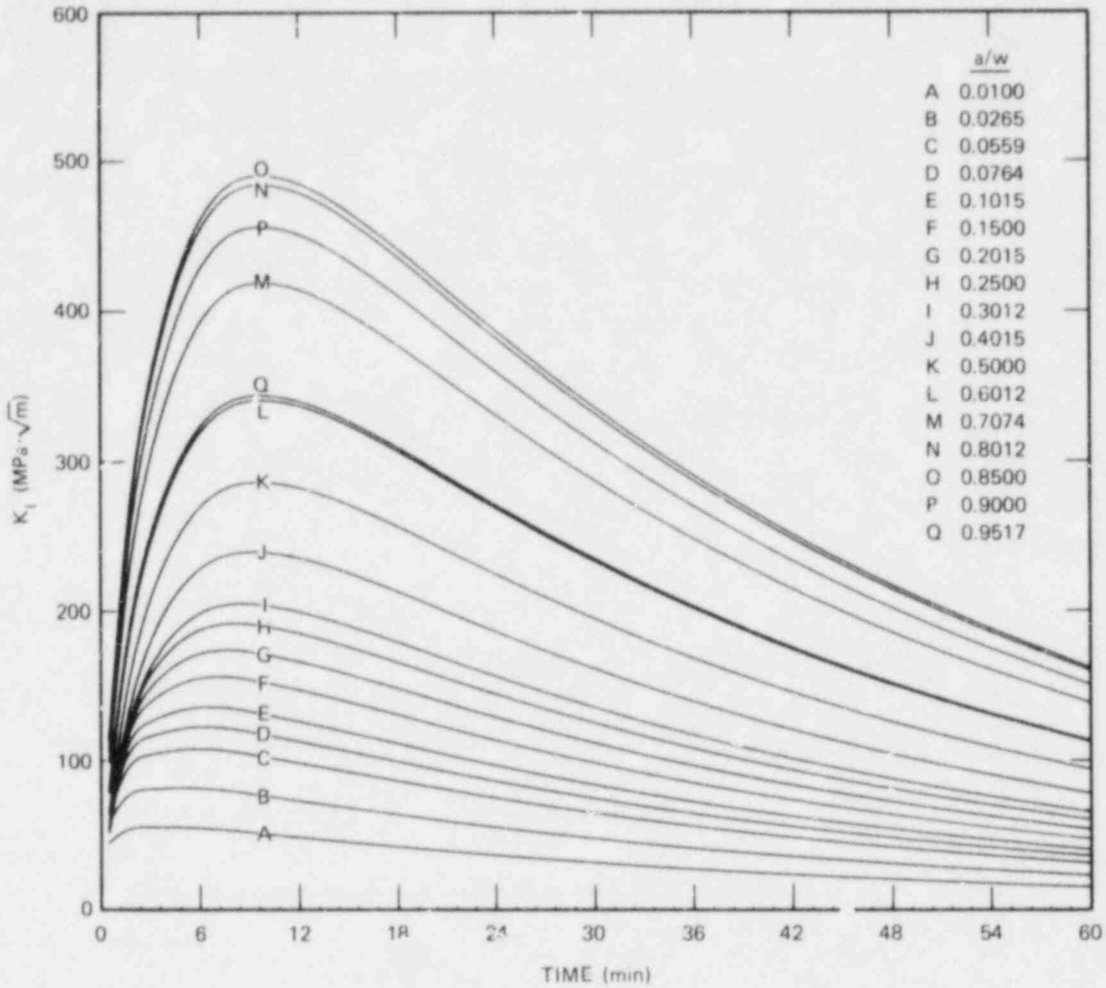

Fig. 4.14. K_I vs time, a/w for LOCA without cladding.

initial reference temperature of −17.8°C, a copper content of 0.25%, and a phosphorus content of 0.012%.

The distributions of the transient variables across the wall thickness after 10 min are shown in Fig. 4.18. The slight oscillations, which can be observed in Figs. 4.17 and 4.18 in the K_I distributions right behind the interface between the cladding and the base material, are artifacts due to mesh variations. They can be diminished by future improvements.

Stress intensity distribution produced by a residual stress. The demonstration of the K_I distribution arising from residual stresses in a clad RPV was the purpose of a calculation assuming a tensile stress in the cladding layer and a compressive stress in the base metal. Looking to long axial flaws, only the circumferential stresses would be considered; they had to fulfill the equilibrium of axial forces across the cylindrical wall. The equilibrium of momentum is assured because of the rotational symmetry of the structure.

ORNL-DWG 82-5786 ETD

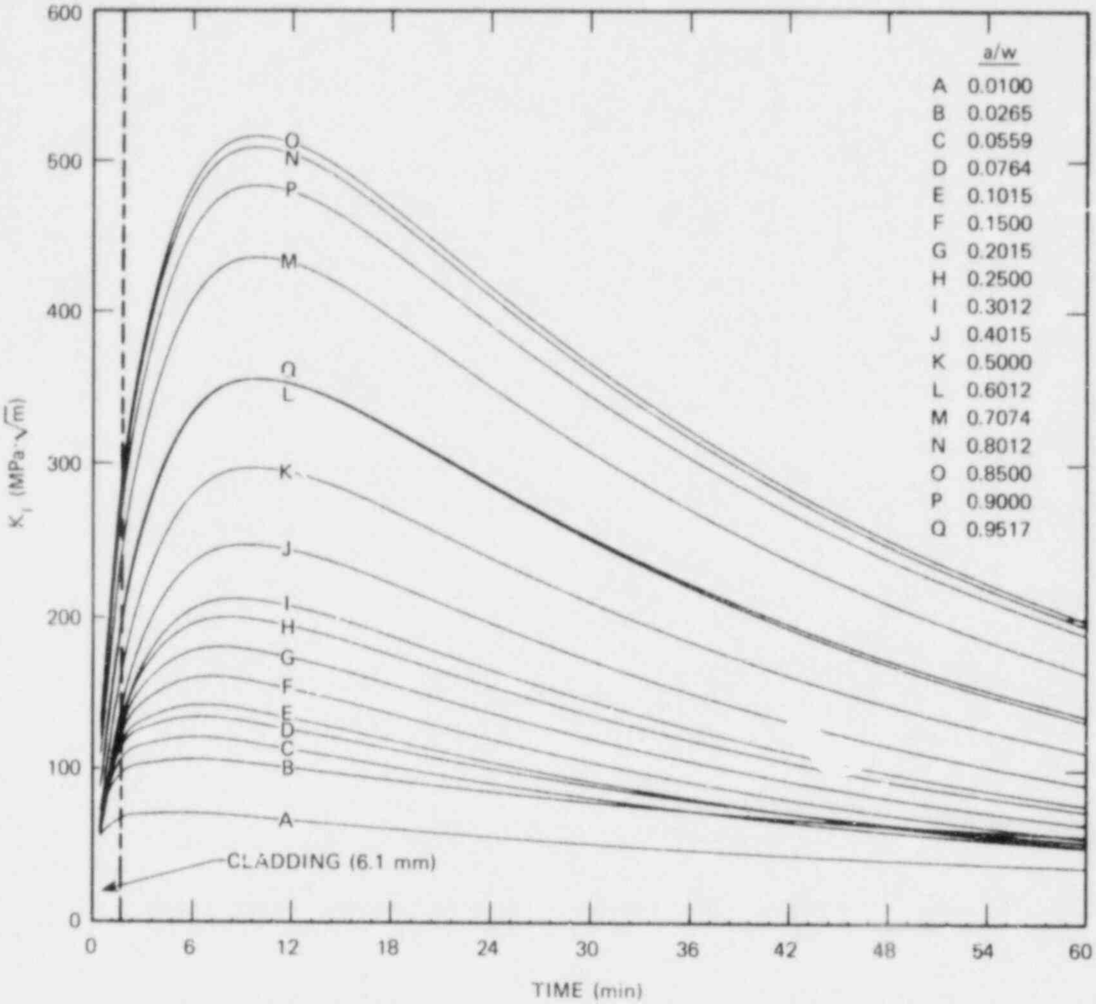

Fig. 4.15. K_I vs time, a/w for LOCA with cladding.

The example chosen was a tensile residual stress in the stainless steel cladding at the yield limit, which was taken to 209 MPa. With the geometrical data (1) an inner diameter of 4368.8 mm, (2) an outer diameter of 4800.6 mm, and (3) cladding thickness of 6.1 mm, one finds for the stress in the base metal − 4.98 MPa.

The definition of the initial temperature was used to solve for the stress distribution. Herein the stresses which are produced by a temperature change from the uniform initial temperature to another uniform temperature are computed, the latter temperature being, for example, a starting temperature in a transient at time 0. These stresses then would be added to the stresses produced by the transient itself for the whole time history.

After some attempts a temperature drop of 214 K was found to give the stress distribution intended. It is shown in Fig. 4.19 together with

ORNL-DWG 82-5787 ETD

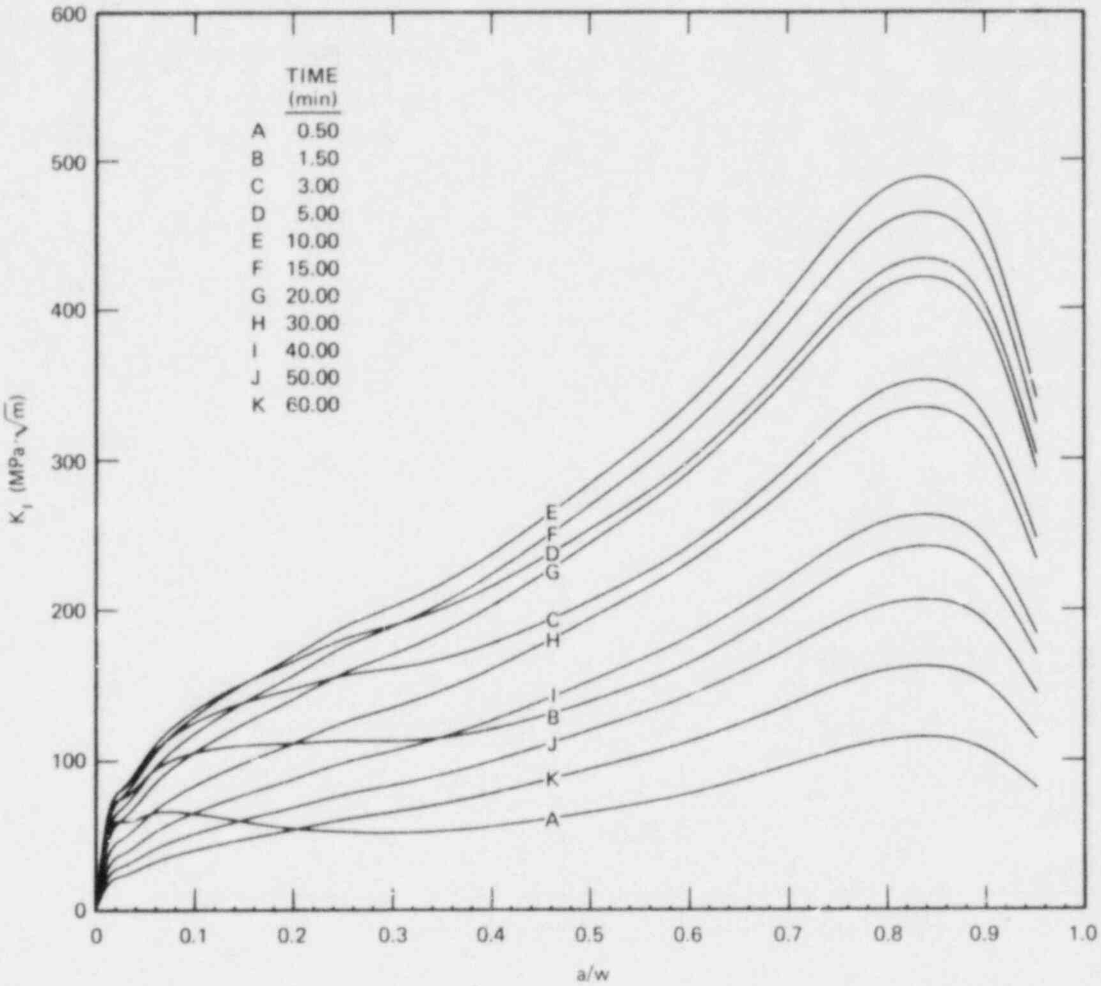

Fig. 4.16. K_I vs a/w, time for LOCA without cladding.

the resulting K_I profile. The latter appears with a sharp peak at the interface between cladding and base metal. In effect, this constitutes a discontinuity in the K_I distribution according to the jump in the stress profile at the interface which is present in any K_I profile resulting from a cladding analysis. Because the plotting routines in the computer code are not capable of showing these discontinuities, the K_I curves appear smoothly dependent on the number of points across the interface on which the K_I values are given.

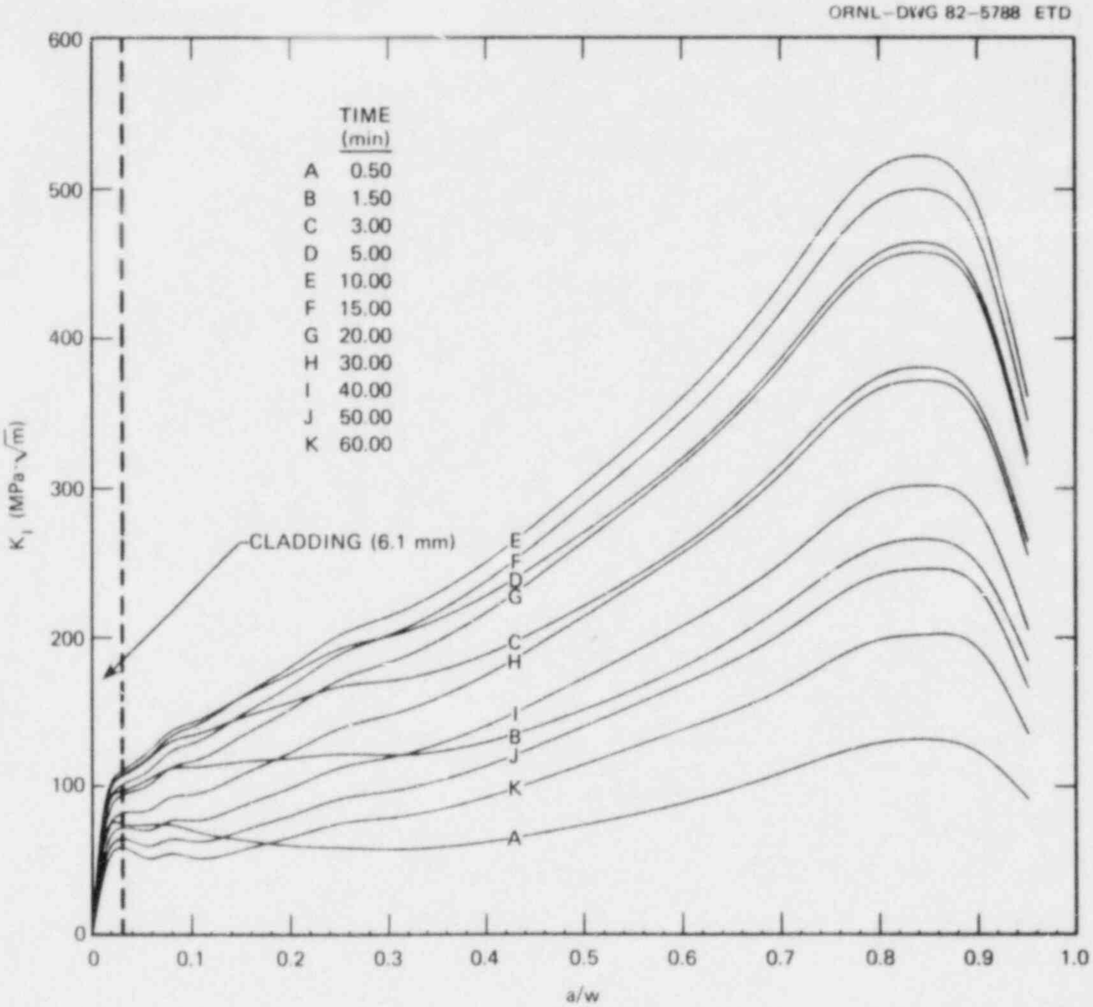

Fig. 4.17. K_I vs a/w, time for LOCA with cladding.

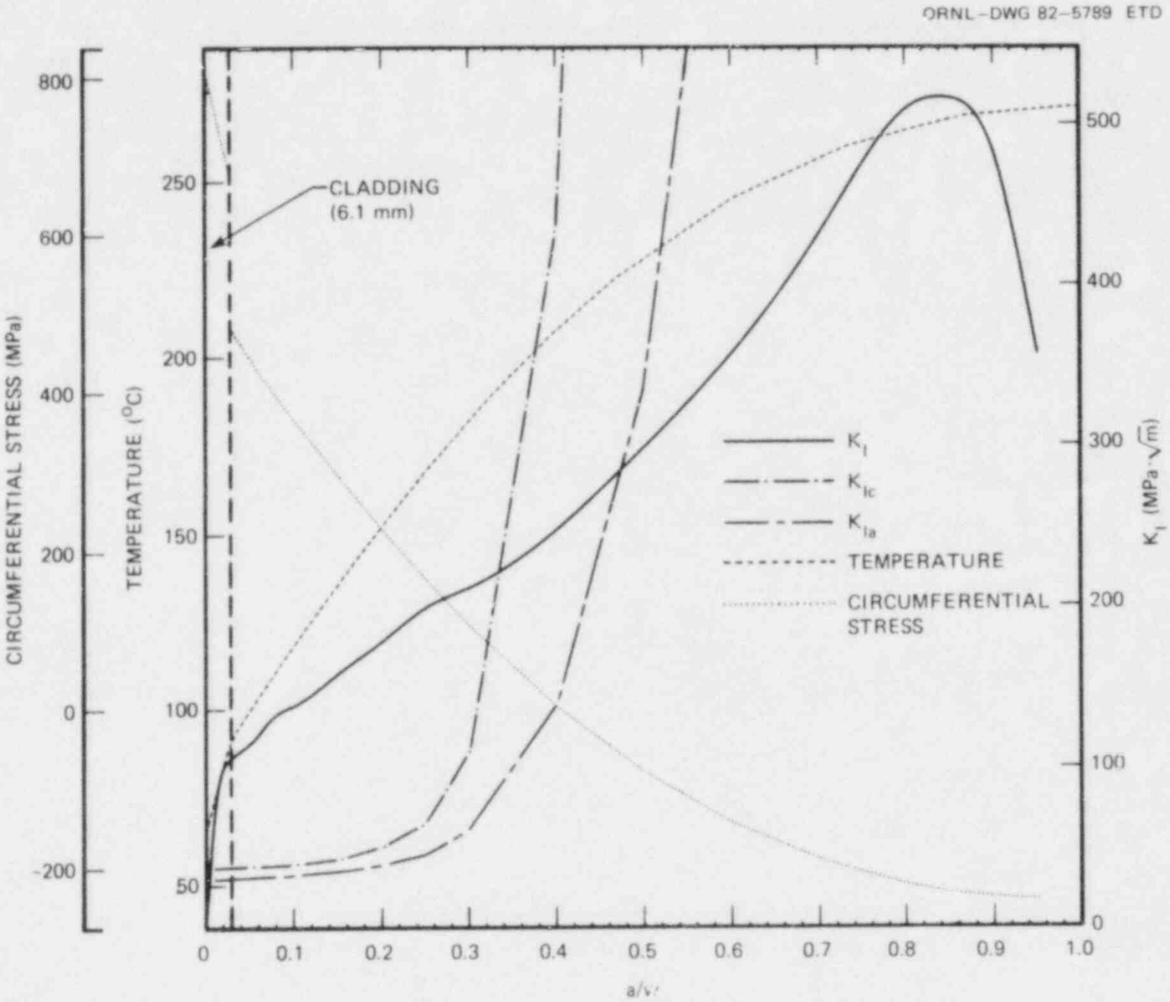

Fig. 4.18. LOCA transient with cladding at 10 min.

ORNL-DWG 82-5790 ETD

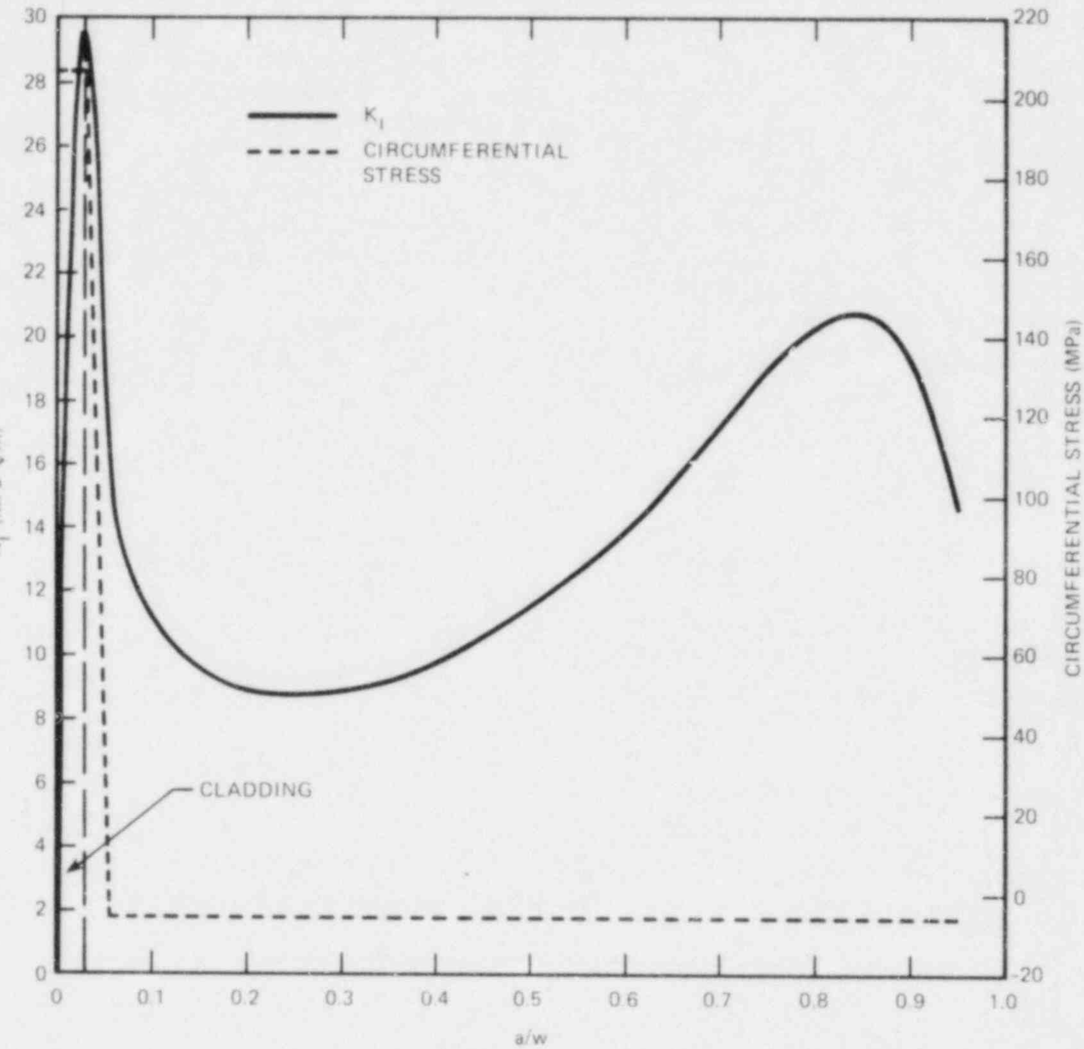

Fig. 4.19. K_I vs a/w resulting from a residual stress distribution.

4.5 Finite-Element-Based Stress Calculation for OCA-I

S. K. Iskander D. G. Ball

In the OCA-I code,[6] the stress-intensity factor K_I is calculated by means of the superposition principle

$$K_I(a) = \sum_{i=1}^{n} \sigma_i \, \Delta a_i \, K_i^* \, (a_i', a) \ , \tag{22}$$

where σ_i, Δa_i, and K_i^* (a_i',a) are defined in Fig. 4.20. In particular, σ_i is the stress at the midpoint of the panel Δa_i in the uncracked vessel. Contributing to these stresses are temperature gradients, pressure loading, etc. The stresses had previously been calculated by means of the standard closed-form solutions.[13] These solutions are derived on the basis of various assumptions, one of which is homogeneous material properties.

To analyze a wider range of problems (e.g., vessels with cladding on the inner surface) the FE method is now used to compute the stresses required for Eq. (22). The OCA-I code has been modified to incorporate the FE procedure in a proposed new version to be called OCA-II. The FE procedure solves the one-dimensional (1-D) axisymmetric problem of a circular cylinder subjected to a radial temperature gradient and/or pressure

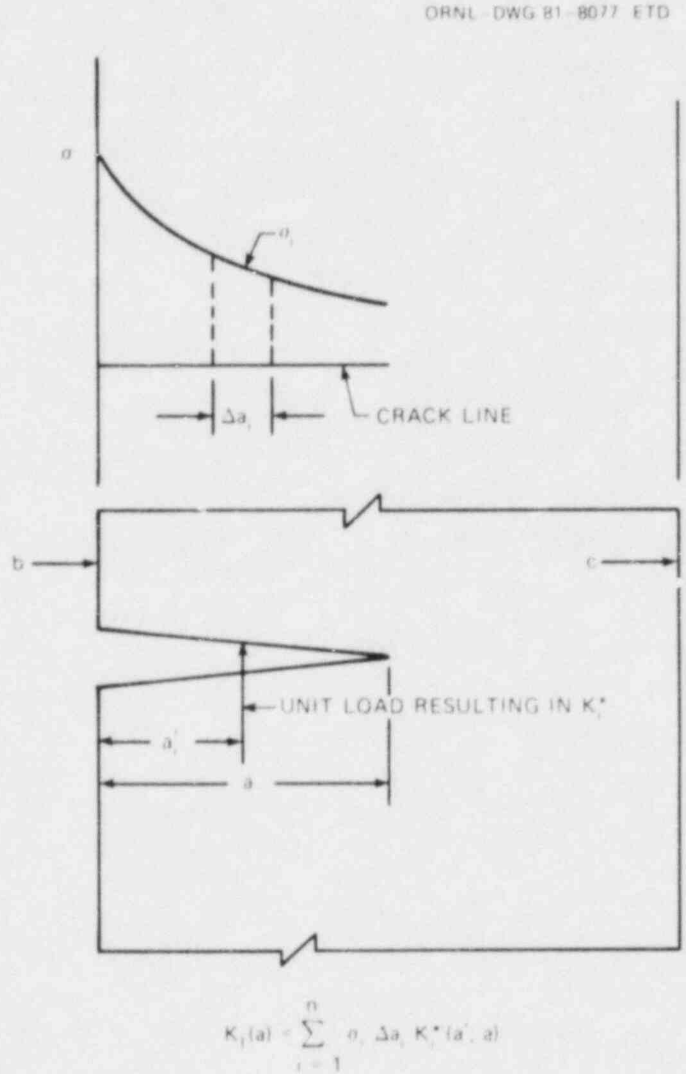

Fig. 4.20. Method of calculation of K_I using the superposition principle.

loading on any of the surfaces. One of the advantages of the FE solution over the closed-form solution is that the material properties can vary arbitrarily in the radial direction, thus permitting the analysis of vessels with cladding. It is also capable of handling temperature-dependent material properties. However, the use of the resulting stresses in Eq. (22) raises some questions about the validity of the resulting K_I.

A brief summary of the equations involved will be presented. The derivations of the FE formulation per se, can be found in the standard texts and will not be repeated here. However, the special case of the 1-D axisymmetric geometry is not readily available and is the one presented, particularly to highlight the method used to calculate the longitudinal stresses in the case of a long cylinder with traction-free ends.

Consider the three-dimensional (3-D) cylindrical coordinate axes (r, t, z) with the r-axis oriented radially, the z-axis oriented along the axis of the cylinder, and the t-axis being mutually normal to both the r and z axes and referred to as the tangential direction.

Assuming the cylinder to be long with no variations in loading or material properties in the tangential or axial directions, the strain-displacement relations in cylindrical coordinates are

$$\varepsilon_r = \frac{du}{dr} ,$$

$$\varepsilon_t = \frac{u}{r} , \tag{23}$$

and

$$\varepsilon_z = \frac{dw}{dz} = \text{constant} ,$$

where u and w are the displacements in the radial and axial directions. The last of Eq. (23) implies that the ends of the cylinder are traction free (an infinitely long cylinder would give zero axial strain).

The general 3-D stress-strain relations for homogeneous isotropic materials can be written as

$$\varepsilon_r = \frac{1}{E} [\sigma_r - \nu(\sigma_t + \sigma_z)] + \alpha T' . \tag{24}$$

with similar expressions for ε_t and ε_z, and E and ν being Young's modulus and Poisson's ratio, respectively. T' is the difference between the temperature at the point and some stress-free reference temperature, and α is the mean coefficient of expansion for the same temperature range.

When these equations are inverted, the stresses are found:

$$\sigma_r = \frac{E}{(1+\nu)(1-2\nu)} [(1-\nu)\varepsilon_r + \nu(\varepsilon_t + \varepsilon_z)] - \frac{\alpha E}{1-2\nu} T' , \qquad (25)$$

with similar expressions for σ_t and σ_z.

Note that although the stress state is 3-D, the mathematical problem to be solved is 1-D in (r). To present the problem in terms of the FE formulation, it is useful to recall that the FE process is based on subdividing the domain to be analyzed into smaller ones called elements. Within each element the continuous (and therefore infinite in number) field variables to be determined are expressed in terms of a finite number of variables at points called nodes. Moreover, for each element the equations of equilibrium are applicable, and for purposes of this discussion, the material properties can be considered constant. Thus, the equations developed for homogeneous material properties are applicable. The 1-D solution for long circular cylinders leads to expressions for σ_r and σ_t that do not involve the axial strain ε_z (Ref. 14). Furthermore, in the case of traction-free faces at either end of the cylinder, the longitudinal stresses are related to the radial and tangential stresses. The stress-strain equations[15] then become

$$\left.\begin{aligned} \sigma_r &= \frac{E}{(1+\nu)(1-2\nu)} [(1-\nu)\varepsilon_r + \nu\varepsilon_t] - \frac{\alpha E}{1-2\nu} T' , \\ \sigma_t &= \frac{E}{(1+\nu)(1-2\nu)} [(1-\nu)\varepsilon_t + \nu\varepsilon_r] - \frac{\alpha E}{1-2\nu} T' , \\ \sigma_z &= \sigma_r + \sigma_t . \end{aligned}\right\} \qquad (26)$$

The FE 1-D formulations will now be presented. Central to the FE formulation is the type of element used. In this case an axisymmetric three-noded bar element (similar to the one used in the 1-R module of OCA-I) is used. The interpolating functions N_i, i = 1,2,3, are

$$\left.\begin{aligned} N_1 &= -\frac{1}{2}(\xi - \xi^2) , \\ N_2 &= 1 - \xi^2 , \\ N_3 &= \frac{1}{2}(\xi + \xi^2) , \end{aligned}\right\} \qquad (27)$$

where ξ is a local variable that ranges between ± 1.

Any field variable ϕ required within the element, such as a coordinate or a displacement, can then be interpolated from the nodal values ϕ_i by means of the expression

$$\phi = \sum_{i=1}^{3} N_i \phi_i$$

or for brevity,

$$\phi = N_i \phi_i .$$

Particularly, the displacements (u) within an element are $u = N_i u_i$, where u_i are the nodal displacements. The strains are therefore

$$\left.\begin{aligned} \varepsilon_r &= \frac{du}{dr} = \frac{dN_i}{dr} u_i \\ &\text{and} \\ \varepsilon_t &= \frac{u}{r} = \frac{N_i}{r} u_i \end{aligned}\right\} , i = 1,2,3 . \tag{28}$$

Utilizing the chain rule of differentiation,

$$\frac{dN_i}{dr} = \frac{dN_i}{d\xi} \cdot \frac{d\xi}{dr} = \left(\frac{dN_i}{d\xi}\right) \Big/ J , \ i = 1,2,3 \tag{29}$$

where J is the Jacobian $(dr/d\xi)$.

Recalling that $r = N_i r_i$, where r_i are the nodal radial coordinates,

$$J = \frac{dr}{d\xi} = \frac{dN_k}{d\xi} \cdot r_k .$$

The values $dN_k/d\xi$ are easily evaluated from Eq. (27).

The basic equations for the displacement FE formulation in linear-elastic problems can be summarized as

$$K_{ij} u_i = F_j, \qquad i,j = 1,2, \ldots N \tag{30}$$

where

N = number of nodes in the FE model,
K_{ij} = global stiffness matrix for the structure,
u_i = vector of the unknown nodal displacements,
F_j = vector of the nodal "forces."

The global stiffness matrix K is obtained by summing the contributions to each node of the element stiffnesses. These element stiffnesses can be expressed as

$$K_{ij} = \int_{\text{volume}} B_i^T D B_j \, dV , \qquad i,j = 1,2,3 \tag{31}$$

where B_i are strain-displacement transformation relations described below, and the superscript T denotes the transpose. The B_i are given by

$$B_i^T = \left[\frac{\partial N_i}{\partial r} \; \frac{N_i}{r}\right] , \qquad i = 1,2,3$$

and

$$D = \frac{E}{(1 + \nu)(1 - 2\nu)} \begin{bmatrix} (1 - \nu) & \nu \\ \nu & (1 - \nu) \end{bmatrix} .$$

To perform the volume integral in Eq. (31), a unit axial distance and a sector of one radian will be assumed. Changing variables, Eq. (31) becomes

$$K_{ij} = \int_{-1}^{+1} B_i^T D B_j N_k r_k J \, d\xi , \qquad i,j = 1,2,3 . \tag{32}$$

The nodal forces vector F_i is given by summing the contributions to node i from each element. Furthermore, $F_i = F_{ei} + F_{oi}$, where F_{ei} is a vector of forces statically equivalent to the surface tractions and body forces, and F_{oi} is a vector of nodal forces statically equivalent to the thermal loads. In this case, the force at node i caused by pressure is simply (pr_i) where (r_i) is the radius coordinate of node i at which the pressure p is applied. The statically equivalent nodal forces caused by the thermal stresses are given by

$$F_{oi} = \int_{\text{volume}} B_i \sigma_o \, dV , \tag{33}$$

where σ_o is the thermal stress and is equal to $E\alpha T'/(1 - 2\nu)$.

To complete the FE formulation, note a few essential details. The integrals in Eqs. (32) and (33) are evaluated numerically. The material properties (which can be temperature dependent) are evaluated for each element at the points at which the numerical integration is performed. The temperature difference T′ is evaluated as the difference between the temperature at the integration point and the stress-free (or "reference") temperature.

The FE coding has been checked out against two closed-form solutions for homogeneous material properties. The two closed-form solutions used are those for a cylinder with a radial temperature distribution and the Lamé solution for a pressurized cylinder. Moreover, the temperature-dependent feature was checked out against a solution obtained by the ADINA code[25] using a 2-D axisymmetric model.* After the FE solution was implemented in OCA-II, it was checked out against the results of OCA-I, which uses the closed-form solution. As a further check, the results from an analysis of a clad cylinder (see Sect. 4.4) were compared with the closed-form solution for that case. In all cases the agreement was excellent.

The computer run times for OCA-II were somewhat less than those for OCA-I. Apparently, the reason is that OCA-I evaluates the stresses using the closed-form solution at every point where the stresses are required, whereas OCA-II evaluates the stresses only at a few discrete points and interpolates between these values when stresses are required at other locations.

4.6 Effect on K_I of Azimuthal Variations in Cooling of the Pressure Vessel Inner Surface

A problem of interest is the effect on the stress-intensity factor K_I of azimuthal variations in cooling of the pressure vessel during an OCA. When the crack is in the coolest portion of the cylinder, the restraint offered by the less cooled part may increase K_I.

Consider the free body diagram shown in Fig. 4.21. The mismatch at the imaginary boundary between the cooled and uncooled portions is a maximum if the cooling covers one-half of the circumference. To impose continuity at the imaginary cut, a shearing force and a moment in the directions shown must be applied. The resultant forces and moments at the crack plane depend on the stiffness of the vessel wall.

To investigate the fracture mechanics aspects of this problem, the superposition principle can still be used because only the stresses in the crack plane are utilized, and these stresses contain all the information necessary to evaluate K_I. However, the solution to the stress problem is two-dimensional (2-D), and the solution for the stresses was accomplished by means of the ADINA computer code.

---

*The version of ADINA available does not have a 1-D axisymmetric bar element.

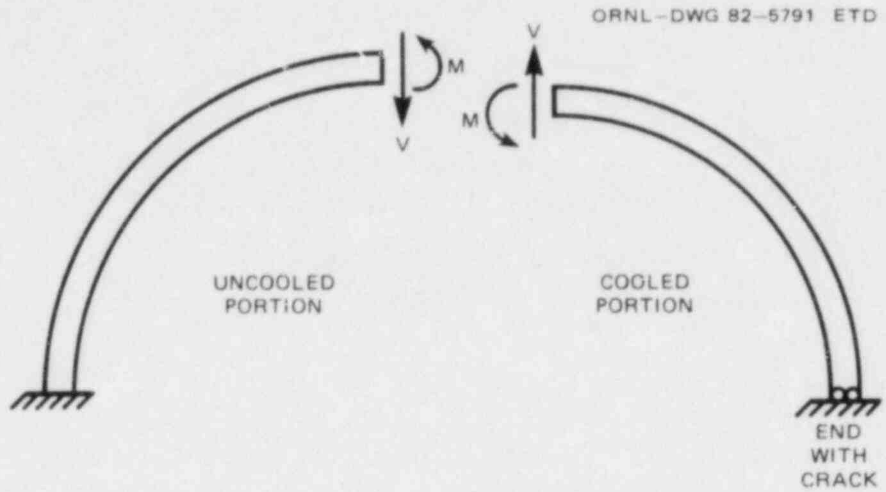

Fig. 4.21. Free-body model of asymmetric cooling of a pressure vessel.

As a possible extreme case the temperature of one-half of the cylinder was kept at 288°C, and the temperatures in the other half of the cylinder were those obtained from a 1-D solution for an LOCA.

The stresses at the crack plane were used in the OCA-I code to evaluate the fracture mechanics effects of the uneven cooling.

For purposes of comparing the effects of the asymmetric cooling with the symmetric cooling case, the following parameters were used in the OCA-I analysis: $RTNDT_o = -1°C$, a copper content of 0.35%, and a fluence of 4×10^{19} neutrons/cm^2.

The results from the OCA-I analysis indicate that the effect on the critical crack depth curves of the uneven cooling, when compared with the case of uniform cooling for the parameters mentioned above, is small. The smallest cracks capable of initiating were 0.008 in the case of even cooling, decreasing very slightly to 0.007 in the uneven cooling case. Moreover, the fluence at which crack initiation can take place when WPS is allowed is decreased by 15%.

As mentioned previously, although the mismatch between the two portions of the free body is a maximum if the cooled portion is one-half of the vessel, the net effect on the crack plane is dependent on the stiffness of the vessel wall as well as the position at which the mismatch occurs. Thus, at this time whether the case analyzed is an extreme case is not clear, and the problem is being investigated further.

4.7 Thermal-Shock Materials Characterization

W. J. Stelzman R. K. Nanstad R. L. Swain

We have completed the fracture toughness characterization of thermal-shock vessel TSC-3 after the vessel had been subjected to the through-the-wall temperature gradient experienced during thermal-shock experiment

TSE-6. The vessel had received a prior temper treatment of 4 h at 613°C, followed by cooling in air. All the specimens were WT-oriented[16] 1T compact specimens (1TCS) machined so that the fatigued crack tips would be located at the 0.41t depth location from the inner surface of the 76-mm-thick wall. All specimens were precracked to an average crack length-to-width ratio (a/W) of 0.547 and tested to failure in a stroke control mode. The crack opening displacement was measured at the specimen load line, and the calculation of the J integral was made using the area-to-maximum load and the Merkle-Corten correction for the tensile component.[17] The static fracture toughness K_J was then calculated from the relationship $K_J^2 = EJ$. Multiple specimens were tested at two test temperatures: −31.7 and 65.6°C.

A total of 19 1TCS were tested, resulting in the distribution listed in Table 4.4 and plotted in Fig. 4.22. Ten specimens were tested

Table 4.4. Static fracture toughness (K_J) from 1T compact specimens[a] from prolongation TSP-3 (SA-508) after tempering at 613°C for 4 h and cooling in air

Test temperature (°C)	Static fracture toughness, K_J (MPa·$\sqrt{m}$)	J integral (kJ/m²)	Average crack extension (mm)
−31.7	87	36	
	104	53	
	95	44	
	138	92	
	144[b]	101	
	49[c]	12	
	123	73	
	99	48	
	80	31	
	97	45	
65.6	275[b]	367	1.92
	164[c]	130	0.14
	249	300	1.90
	270	351	3.69
	265	339	2.17
	263	334	0.80
	233	262	0.43
	264	335	0.92
	247	296	1.20

[a]CT-oriented.

[b]Maximum toughness.

[c]Minimum toughness.

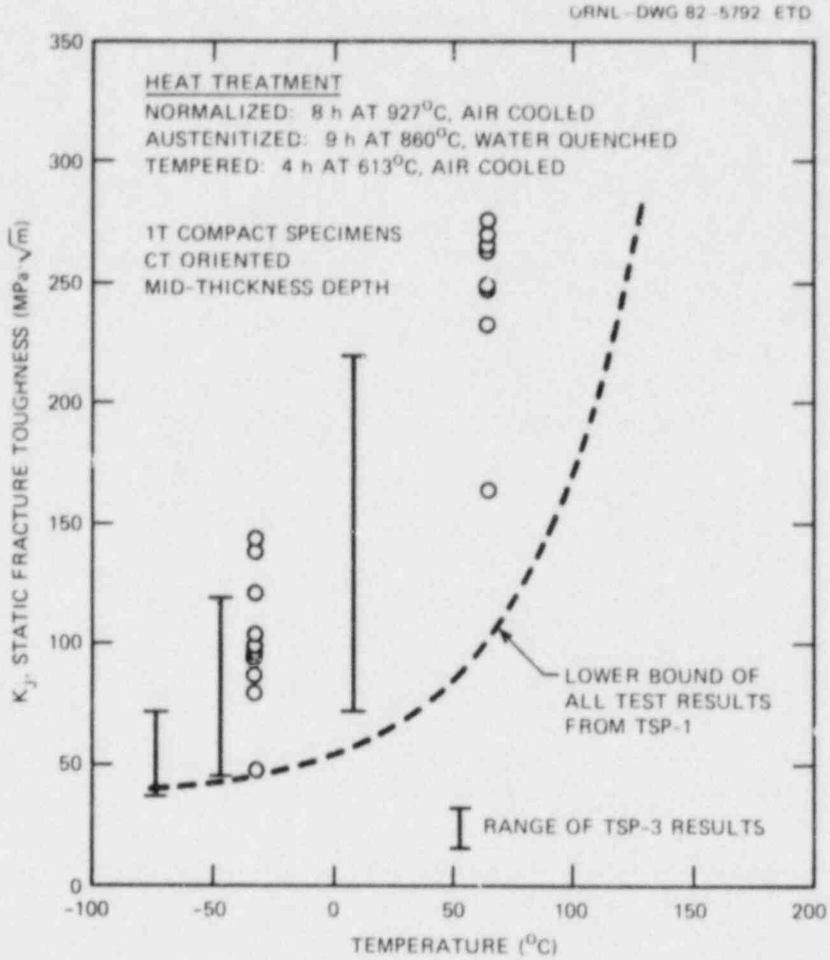

Fig. 4.22. Static fracture toughness (K_J) of "as-quenched" 76-mm-thick thermal shock vessel TSC-3 after tempering for 4 h at 613°C and cooling in air.

at −31.7°C with the K_J values ranging from 49 to 144 MPa·$\sqrt{m}$, and nine specimens were tested at 65.6°C with the K_J values ranging from 164 to 275 MPa·$\sqrt{m}$. These results cannot be compared directly with previously reported results from prolongations TSP-1 (Ref. 18) or TSP-3 (Ref. 19), because different test temperatures were investigated; however, they can be compared with the lower-bound curve constructed from the TSP-1 results. The range of K_J values from TSP-1 and TSP-3 have also been included in Table 4.5. The range of K_J from TSP-3 is also indicated in Fig. 4.22, together with the lower-bound curve for all the K_J results from TSP-1. The lowest fracture toughness result from TSC-3 at −31.7°C, 49 MPa·$\sqrt{m}$, compares well with the 44 MPa·$\sqrt{m}$ estimate from the lower-bound curve from TSP-1. Two of the specimens gave "valid" plane-strain fracture values by ASTM Standard E399.

All nine specimens tested at 65.6°C underwent mode conversion from ductile tearing to cleavage fracture. Seven specimens failed beyond

Table 4.5. Summary of the static fracture toughness (K_J) results with compact specimens[a] from prolongations TSP-1 and TSP-3 and vessel TSC-3 after receiving similar temper heat treatments[b]

Test temperature (°C)	Number of specimens 0.394T	1T	2T	Range of K_J (MPa·$\sqrt{m}$)
		Prolongation TSP-3[c,d]		
10.0		15		72–220
−45.6		10		46–120
−73.3		10		38–72
		Prolongation TSP-1[c,e]		
82.2		7	8	116[d]–298[f]
37.8	6			114–224
32.2		7	4	70[d]–221[f]
10.0	6			103–214
−17.8	14	4	5	51[f]–184
−45.6	3			41–101
−73.3	3			62–101
		Vessel TSC-3[d,g]		
−31.7		10		49–144
65.6		9		164–275

[a]CT orientation.

[b]Tempered 4 h at 613°C, cooling in air.

[c]Between 35 and 114 mm from the inner surface of the 152-mm-thick walls of the prolongations.

[d]Maximum and/or minimum values from 1T CS.

[e]Maximum and/or minimum values from 0.394T CS unless noted otherwise.

[f]Value from 2T CS.

[g]At 31 mm from the inner surface of 76-mm-thick wall.

limit load. The estimated lower bound from the TSP-1 results at 65.6°C is 110 MPa·$\sqrt{m}$, which is considerably below the 164 MPa·$\sqrt{m}$ result from TSC-3. After testing, the crack extension prior to onset of fast fracture was measured using a nine-point average technique for each specimen. This information is also included in Table 4.4. The J values (not corrected for crack growth) as a function of Δa (crack extension) for the specimens tested at 65.6°C are shown in Fig. 4.23.

Three methods of curve fitting the J-Δa data were used to determine J_{Ic}. The ASTM E813 (Ref. 20) method prescribes a linear regression of the form $J = C_1 + C_2\Delta a$, using only the data pairs between the exclusion lines; the intersection of the regression line with the blunting line is designated as the J_{Ic} value. This method yielded a J_{Ic} of about 273 kJ/m². Two other techniques were used, a power law of the form $J = C_1\Delta a^{C_2}$, and a hyperbola of the form $J = C_1C_2\Delta a/(1 + C_2\Delta a)$. The resultant curves are shown in Fig. 4.23. For these curves, the intersection with the 0.15-mm exclusion line is designated J_{Ic}, and values of 232 and 228 kJ/m² were obtained for the power law and hyperbola, respectively. The table below gives the constants and toughnesses (E = 207 GPa) determined for each fitting method using units of in.-lb/in.² for J and in. for

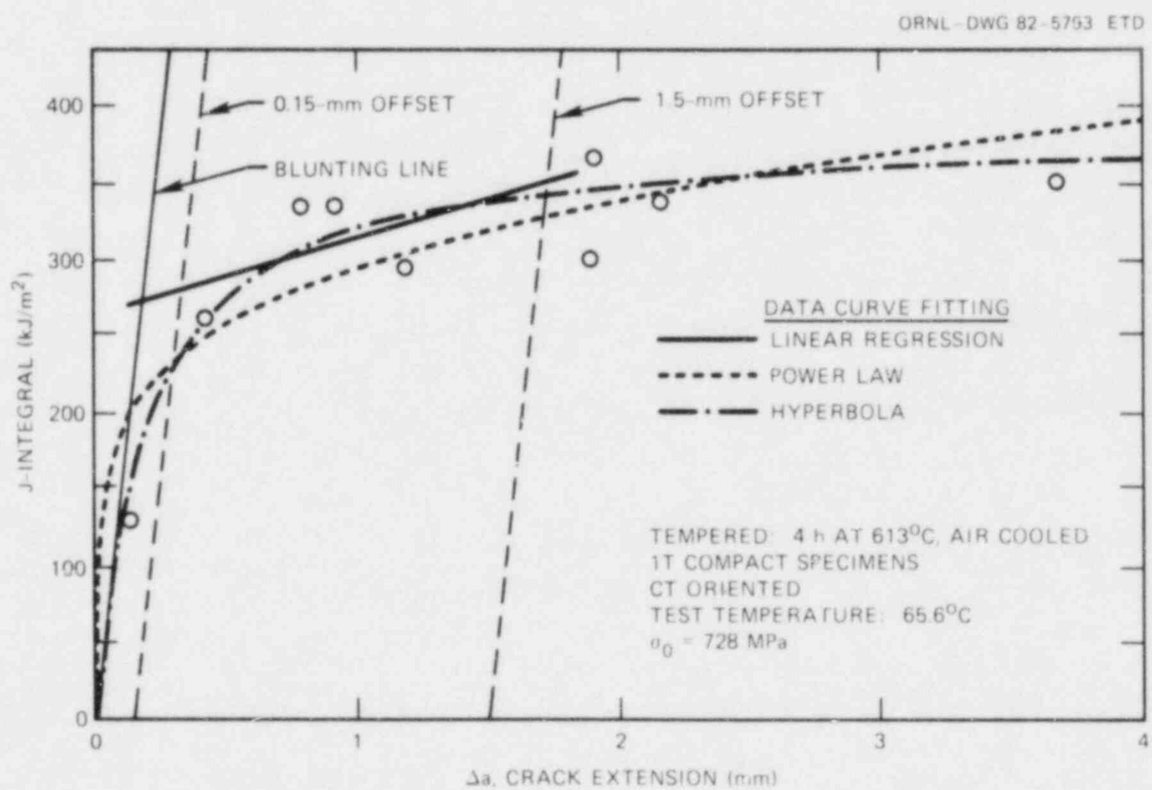

Fig. 4.23. Variation of J-integral with stable crack growth for 1T compact specimens from 76-mm-thick thermal shock vessel TSC-3 after tempering at 613°C for 4 h and cooling in air.

crack extension:

Parameter	Linear	Power law	Hyperbola
C_1	1508	3244	2149
C_2	7391	0.2034	125.2
J, kJ/m² (in.-lb/in.²)	273 (1560)	232 (1325)	228 (1300)
K_J, MPa·$\sqrt{m}$ (ksi$\sqrt{in.}$)	237 (216)	219 (199)	217 (197)

The power law fit rises steeply to the left of the blunting line, because there is only one J-Δa point in the blunting line region. These values of K_J (converted from J_{Ic}) can be compared with the lowest value obtained, 164 MPa·$\sqrt{m}$. In the future, unloading compliance tests will be performed to compare with these results.

We also determined that the nil-ductility transition temperature (NDTT) of vessel TSC-3, using type P-3 drop-weight specimens,[21] was −62.2°C. This compares with the NDTT of −45.6°C obtained from prolongation TSP-1. In both cases, single-pass Hardex N crack-starter welds were used for crack initiation. The lower NDTT appears to be associated with a tempered heat-affected zone (HAZ), which arrests the running crack until the test temperature is sufficiently low that it can penetrate the HAZ into the base plate. On penetration of the HAZ, the specimen immediately fails, indicating that the plate NDTT is at a much higher temperature and that the drop-weight test for this material tempered at 613°C is primarily a test of the HAZ, not the plate. H. Tsukada and coworkers[22] have investigated the effect of crack-starter weld application on the NDTT of A-508 class 2 and found the single-pass method of application to be more satisfactory than the two-pass method. They noted a 40-K shift in the NDTT to higher test temperatures in A-508 class 2 with single-pass compared with that for two-pass and attributed it in part to the HAZ toughness. The problem of HAZ toughness appears to be aggravated in TSC-3, even with a single-pass weld bead technique because of the low tempering temperature used. This situation is recognized for quenched and tempered steels in Para. 5.3 of E208 (Ref. 21). Further investigations are being pursued relative to NDTT determinations for materials such as TSC-3.

The Charpy V-notch impact properties of TSC-3 were also determined with CT-oriented specimens tested over a temperature range of −73.3 to 149°C and at two depth locations (0.08 and 0.42t) from the inner surfaces. The results are shown in Figs. 4.24 and 4.25. The effect of depth is minimal, and the Charpy V-notch specimens exhibited fully ductile behavior (onset of upper shelf) between 104 and 121°C. We also determined the RT_{NDT} using the 68-J energy and 0.89-mm lateral expansion criteria set forth in Sect. III, Subsect. NB, Article NB-2330 of the ASME *Boiler and Pressure Vessel Code*.[23] An example of an application has been described previously.[24] The lowest temperature at which the criteria were met by the required three Charpy V-notch (TC_V) specimens were 93 and 104°C for specimens from the 0.08 and 0.42t depth locations, respectively. The RT_{NDT} from Charpy V-notch specimens is determined from the relationship TC_V − 33°C. For TSE-3, using 0.42t depth results, the RT_{NDT} = 104°C − 33°C = 71°C.

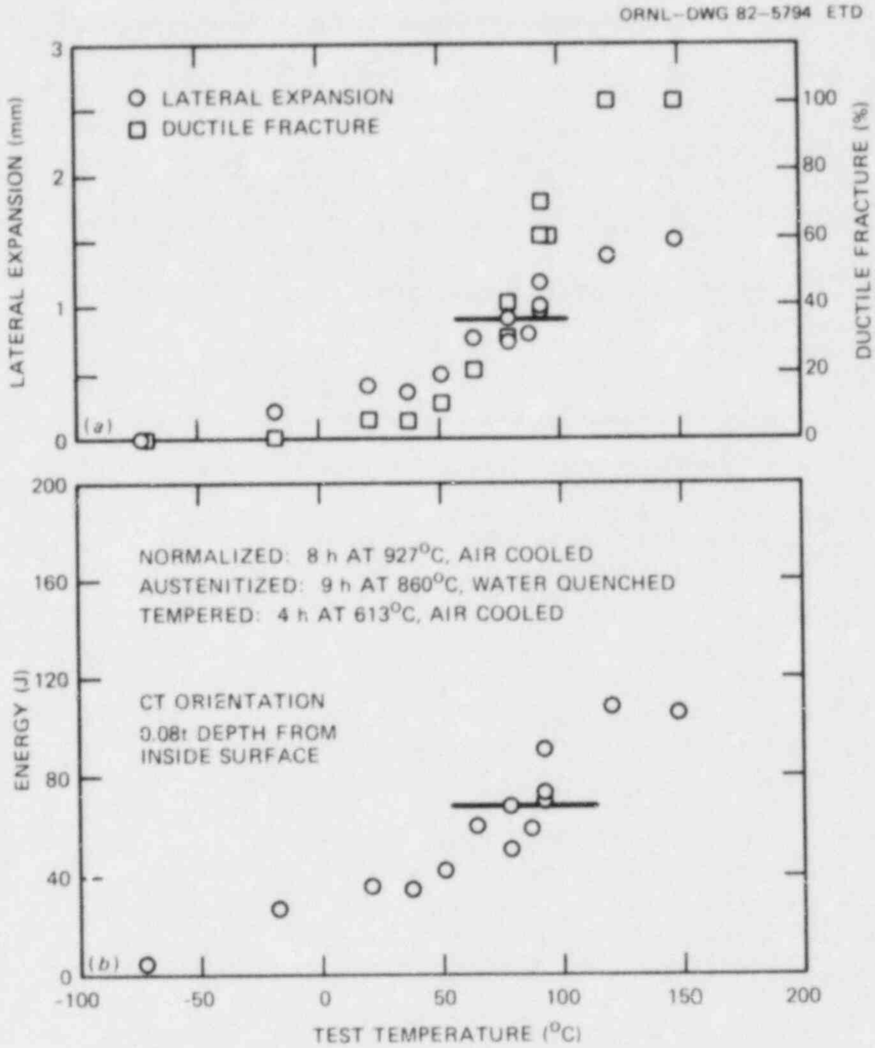

Fig. 4.24. Charpy V-notch impact properties of "as-quenched" 76-mm-thick thermal shock vessel TSC-3 after tempering for 4 h at 613°C and cooling in air; (a) fracture appearance and lateral expansion, (b) impact energy.

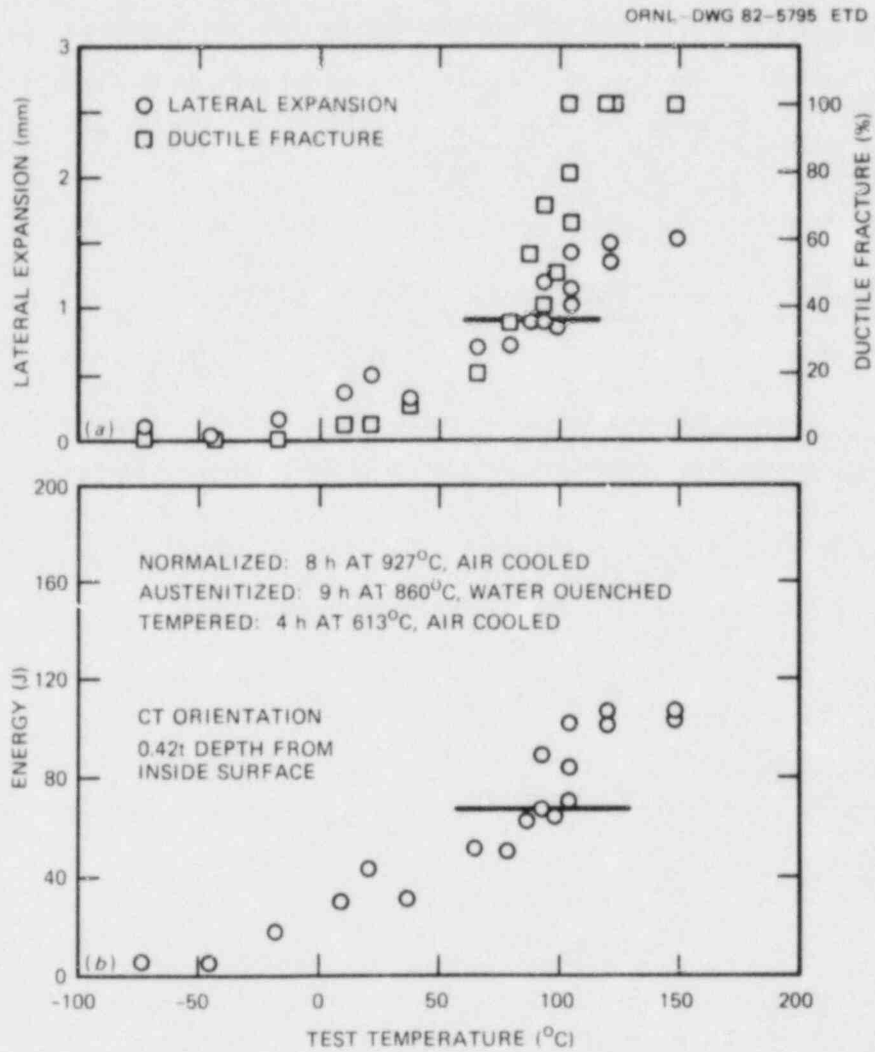

Fig. 4.25. Charpy V-notch impact properties of "as-quenched" 76-mm-thick thermal shock vessel TSC-3 after tempering for 4 h at 613°C and cooling in air; (a) fracture appearance and lateral expansion, (b) impact energy.

References

1. R. D. Cheverton et al., "Thermal-Shock Investigations," *Heavy-Section Steel Technology Program Quart. Prog. Rep. October–December 1981*, ORNL/TM-8252.

2. "Plane Strain Fracture Toughness of Metallic Materials," ASTM E399-78, *Annual Book of ASTM Standards*, Part 31, American Society for Testing and Materials, Philadelphia, 1978.

3. R. D. Cheverton et al., "Thermal-Shock Investigations," *Heavy-Section Steel Technology Program Quart. Prog. Rep. October–December 1979*, ORNL/NUREG/TM-380, pp. 67–70.

4. R. D. Cheverton et al., *Heavy-Section Steel Technology Program Quart. Prog. Rep. April–June 1981*, ORNL/TM-7955, pp. 60–65.

5. R. D. Cheverton, S. K. Iskander, and D. G. Ball, *PWR Pressure Vessel Integrity During Overcooling Accidents: A Parametric Analysis*, ORNL/TM-7931 (to be published).

6. S. K. Iskander, R. D. Cheverton, and D. G. Ball, *OCA-I, A Code for Calculating the Behavior of Flaws on the Inner Surface of a Pressure Vessel Subjected to Temperature and Pressure Transients*, ORNL/NUREG-84 (August 1981).

7. USNRC, "Effects of Residual Elements on Predicted Radiation Damage to Reactor Pressure Vessel Materials," *Reg. Guide 1.99, Rev. 1* (Sept. 16, 1976).

8. T. U. Marston (Ed.), *Flaw Evaluation Procedures: ASME Section XI*, EPRI NP-719-SR (August 1978).

9. R. Ahlstrand, P. Paalilainan, and H. Raiko, "LEFM Analysis of Irradiated Nuclear Components Having Welded Cladding," Paper G1/4 in *Transactions of the 6th International Conference on Structural Mechanics in Reactor Technology*, Vol. G, August 1981.

10. R. D. Cheverton, S. K. Iskander, and S. E. Bolt, *Applicability of LEFM to the Analysis of PWR Vessels Under LOCA-ECC Thermal Shock Conditions*, NUREG/CR-0107 (ORNL/NUREG-40) (October 1978).

11. H. F. Bueckner, "A Novel Principle for the Computation of Stress Intensity Factors," *Z. Agnew. Math. Mech.* 50, 526–546 (1970).

12. Private Notes from J. G. Merkle: "Thermal Stresses and Strains in an Elastic, Hollow Cylinder," 1963.

13. S. Timoshenko, *Strength of Materials, Part II, Advanced Theory and Problems*, 2nd Ed., D. Van Nostrand Co., Inc., New York, 1951.

14. B. A. Boley and J. H. Weiner, *Theory of Thermal Stresses*, John Wiley & Sons, New York, 1960.

15. K. J. Bathe, *ADINA — A Finite Element Program for Automatic Dynamic Incremental Nonlinear Analysis*, Massachusetts Institute of Technology Report 82448-1 (1975, revised 1978).

16. W. J. Stelzman and D. A. Canonico, "Thermal Shock-Temper Study," *Heavy-Section Steel Technology Program Quart. Prog. Rep. January–March 1979*, NUREG/CR-0818 (ORNL/NUREG/TM-324), pp. 104–10.

17. J. G. Merkle and H. T. Corten, "A J-Integral Analysis for the Compact Specimen, Considering Axial Force as Well as Bending Effects," *J. Press. Vessel Technol.*, Series J, of *Trans. ASME* 96(4), 286–92 (1974).

18. W. J. Stelzman and D. A. Canonico, "Thermal Shock Material Characterization," *Heavy-Section Steel Technology Program Quart. Prog. Rep. April–June 1981*, NUREG/CR-1627 (ORNL/NUREG/TM-401), pp. 42–55.

19. W. J. Stelzman, R. K. Nanstad, and R. L. Swain, "Thermal Shock Material Characterization," *Heavy-Section Steel Technology Program Quart. Prog. Rep. July–September 1981*, NUREG/CR-2141 (ORNL/TM-8145), pp. 97–101.

20. "Standard Test for J_{Ic}, A Measure of Fracture Toughness, ASTM Designation: E813-81," *Annual Book of ASTM Standards*, Part 10, American Society for Testing and Materials, Philadelphia, 1981.

21. "Conducting Drop-Weight Test to Determine Nil-Ductility Transition Temperature of Ferritic Steels, ASTM Designation: E208-69," *Annual Book of ASTM Standards*, Part 10, American Society for Testing and Materials, Philadelphia, 1981.

22. H. Tsukada et al., "A Study of Drop-Weight Tests Using A508 Class 2 Steel," paper R(MS)81-60, Japan Steel Works, Ltd. (Dec. 1, 1981).

23. ASME, *Boiler and Pressure Vessel Code*, Sect. III, Div. 1, "Nuclear Power Plant Components," 1977 Ed. and Addenda, American Society of Mechanical Engineers, New York.

24. W. J. Stelzman and D. A. Canonico, "Characterization of the V-9 Prolongation," *Heavy-Section Steel Technology Program Quart. Prog. Rep. October–December 1978*, NUREG/CR-0656 (ORNL/NUREG/TM-298), pp. 40–43.

5. PRESSURE VESSEL INVESTIGATIONS

5.1 Preparation for Intermediate Vessel Test V-8A

R. H. Bryan

5.1.1 Introduction

Intermediate test vessel (ITV) V-8A, in which the Babcock & Wilcox Company (B&W) placed a special low-upper-shelf seam weld, is being prepared for a fracture mechanics test. During this quarter fracture and stress analyses were performed, and instability conditions were investigated as a basis for selection of flaw dimensions. Subsequently, a flaw was generated in the special seam weld. Vessel instrumentation plans were completed, and the process of preparing, installing, and testing sensors and associated apparatus was initiated. Work continued on reactivation of the vessel test facility.

The work of B&W on the special seam weld under subcontract was essentially completed with the submission of the manuscript of a final report.[1]

5.1.2 Test objectives and plans for vessel V-8A

Intermediate test vessel V-8A is being prepared for a fracture test of which the purpose is to investigate tearing behavior of material having low-upper-shelf toughness similar to the toughness of irradiated high-copper seam welds in some existing reactor pressure vessels. Toughness properties of irradiated high-copper submerged arc welds have been investigated at Oak Ridge National Laboratory (ORNL) and the Naval Research Laboratory under the Nuclear Regulatory Commission's (NRC's) safety research program, and it has been determined that upper-shelf Charpy impact energies of such welds may typically fall below 68 J (50 ft-lb).[2,3] This level is particularly important inasmuch as it is an essential factor used in Appendix G of 10 CFR Part 50 (Ref. 4) in the determination of safe conditions for operation of reactor pressure vessels. One implication of Appendix G is that a vessel having an upper-shelf Charpy impact energy below 68 J cannot be operated with additional inspections and evaluations.

The NRC is considering all aspects of this problem by research and other regulatory actions[3] intended to identify, if possible, alternative procedures by which material not meeting the 68-J criterion may be safely used. Identification and acceptance of an alternative criterion requires an understanding of the physical phenomena of ductile fracture, and a confirmation that methods of analyzing this type of fracture are reliable. The V-8A test will be a large-scale experiment by which various theoretical concepts and methods of elastic-plastic fracture mechanics can be evaluated.

The V-8A test plan is based on the presumption that a ductile fracture theory can predict three phases of fracture: the load at which tearing commences, the relationship between increasing load and progressive stable tearing, and the load at which tearing becomes unstable. Methods of analysis based on J-integral concepts are supposed to be capable of these predictions, provided that the tearing resistance of the material and tensile properties are known. Thus, the test plan comprises:

1. the preparation of a test vessel with a sharp flaw in low-upper-shelf material;
2. measurement of the properties of the material;
3. instrumentation of the vessel for measurement of load, stress state, and crack geometry;
4. prediction of flaw and vessel behavior;
5. pressurization of the vessel to the point of incipient instability;
6. unloading;
7. posttest examination of the flaw; and
8. posttest analysis.

Vessel V-8A is ITV V-8 (Refs. 5 and 6) repaired and modified by the placing of a longitudinal seam weld of special low-upper-shelf material. Figure 5.1 schematically shows the features of vessel V-8A. Under subcontract, B&W developed a special welding procedure for low-upper-shelf material meeting ORNL specifications on upper-shelf Charpy impact energy and yield strength.[7] Subsequently, B&W repaired vessel V-8, made a flawing practice weldment, made the special seam weld in the vessel, made about 3 m of special seam welds for preparation of material characterization specimens, and made and tested the specimens.[8-10] Details of the B&W work are reported in Ref. 1.

In the Heavy-Section Steel Technology (HSST) program, three flawed cylindrical ITVs with initial flaw depths less than one-half the thickness

ORNL-DWG 80-5235 ETD

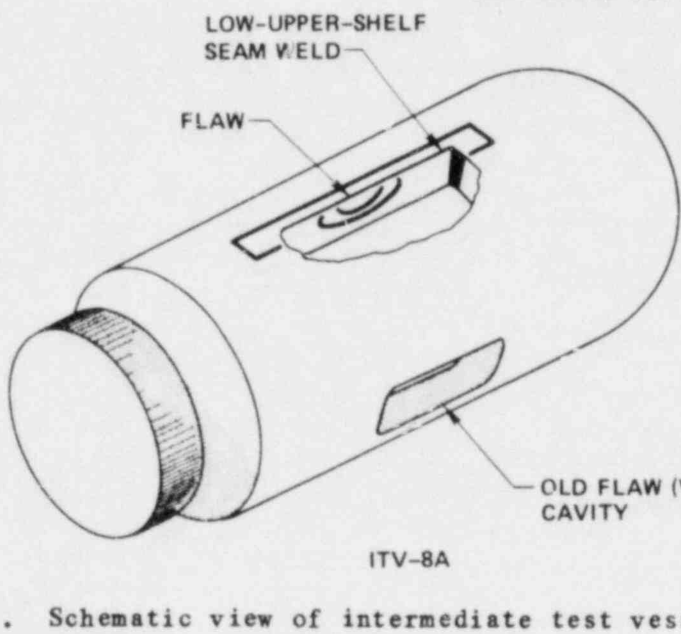

Fig. 5.1. Schematic view of intermediate test vessel V-8A showing prepared flaw in special low-upper-shelf seam weld.

have been tested to failure at upper-shelf temperatures. Vessels V-1 and V-3 were tested at 54°C, a temperature near the onset of the Charpy-impact energy upper shelf, while V-6 was tested at 88°C (Ref. 11). The flaws in these vessels, which were typically as tough as good pressure vessel steels, exhibited a ductile tearing behavior. Tearing instabilities occurred only after the vessel wall had fully yielded and probably a local plastic instability had developed. Thus, the conditions of the tests were not conducive to quantitative evaluation of ductile fracture, because unstable deformations, irrespective of tearing, were occurring.

The toughness of low-upper-shelf material in V-8A is more suitable for testing theories of elastic-plastic fracture. With this material it is feasible to attain incipiently unstable crack growth prior to gross yield in the ITV. At the point of gross section yielding, an unflawed cylinder experiences a temporary instability, in that it may deform without a further increment in load until strains reach ~1%. When gross yielding occurs in a vessel test, it is impractical to make the measurements necessary for a decisive evaluation of fracture theories. This consideration influenced the selection of flaw size for the V-8A test.

The desire to observe incipient tearing instability implied limitations on material properties and the vessel test temperature. As was demonstrated in the V-1 and V-3 tests, a ductile tear may change to a fast cleavage fracture if the test temperature is not substantially higher than the onset of the Charpy upper shelf.[11] An unstable ductile fracture may proceed slowly enough in an ITV to be arrested by a drop in load, as was observed in the V-7B test,[12] but a cleavage fracture would burst the vessel. Accordingly, the V-8A test temperature, 150°C, is 35 K above the temperature of the onset of the upper shelf as defined by 100% shear appearance of Charpy-impact specimens.

The pressurization test will be carried out with the intent of observing flaw geometry changes with increasing load and preserving the final flaw geometry for precise posttest measurement. The test consists of

1. slowly increasing pressure while continuously recording strains, crack-mouth-opening displacements (CMOD), and ultrasonic measurements of crack geometry;
2. intermittent partial unloading for elastic compliance measurements, which will be used for estimating flaw depths;
3. sustained loading, with pressure being held constant if possible long enough to detect incipient flow instability;
4. rapid partial unloading on detection of an instability to interrupt unstable tearing; and
5. repressurization after interruption of loading, if necessary, to confirm the attainment of an instability.

If possible, the test will be terminated prior to attainment of a burst condition to permit the recovery of important information on flaw geometry and to permit reuse of the vessel.

5.1.3 Fracture and stress analysis of vessel V-8A

J. G. Merkle, B. R. Bass, J. W. Bryson, R. H. Bryan, G. D. Whitman

Statement of problem. In vessel V-8A as pressure is increased the flaw will first tear at a load determined by J_{Ic} of the material, then tear stably until a pressure is reached at which the flaw will continue to grow without further increase in load. This tearing instability can be produced in two ways. If tearing resistance is high enough a flaw of a given size may not be prone to tear unstably until a local or general plastic instability develops, in which case the flawed region would deform without an increase in load. In this instance the strain field around the flaw changes with time even if the flaw size and applied load do not. If, on the other hand, tearing resistance is low enough a tearing instability will occur at a flaw size and applied load that cannot cause a plastic instability. In both cases tearing eventually ensues, but in the latter situation the state of stress that caused the tearing instability is more clearly defined and measured.

In planning the V-8A test both cases must be considered in order that observations of fracture can be attributed to the proper causes. Analyses are being made to define structural instabilities as well as tearing instabilities based on V-8A material properties determined by B&W (Refs. 1 and 10) and ORNL (Ref. 10). Selection of the V-8A flaw geometry and decisions on the placement of vessel instrumentation were made as a consequence of the preliminary analyses described in the following paragraphs.

Five types of analyses were made: tangent-modulus (TM) elastic-plastic fracture analysis, linear-elastic fracture analysis based on Raju-Newman equations, ORVIRT-3D finite-element elastic-plastic fracture analysis, local plastic instability analysis of a flawed cylinder, and determination of gross yield of an unflawed cylinder.

Simplified analyses were based on the definition of a piecewise linear stress-strain relationship defined in Fig. 5.2. The relationship consists of a perfectly linear-elastic region A, a perfectly plastic region B, and a strain hardening region C. Values of the relevant stress-strain parameters used in these analyses are given in Table 5.1 and represent the best estimates of tensile properties available at the time. From these data the pressure-strain relationship, shown in Fig. 5.3, was calculated for an infinitely long unflawed cylinder of V-8A geometry. This relationship is used to relate nominal strains, calculated by linear-elastic fracture mechanics (LEFM) or the TM method[13] to vessel pressure.

The inital fracture mechanics computations performed for the purpose of selecting a flaw size for vessel V-8A employed closed-form expressions that could be solved explicitly for a strain, given the flaw geometry and a value K_I or J_I. For nominal strains below the value of outside surface circumferential strain at which gross yield occurs (Fig. 5.3) LEFM applies; that is,

$$K_I = C\sigma \sqrt{\pi a}$$

ORNL-DWG 82-5796 ETD

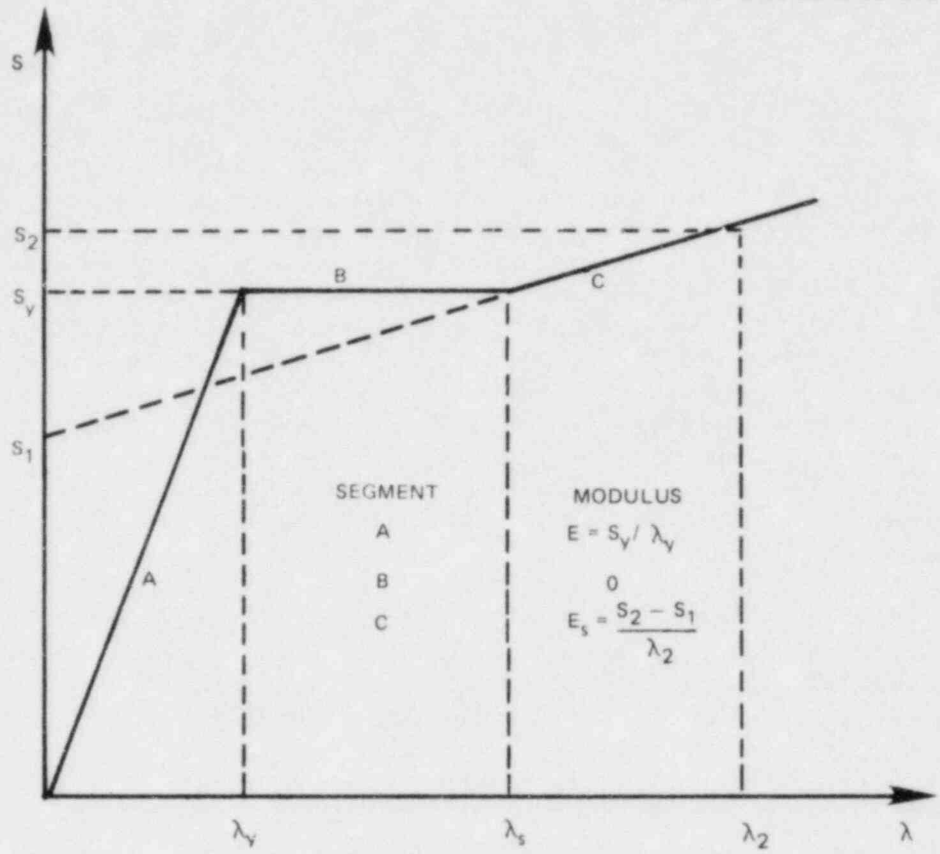

Fig. 5.2. Stress and strain parameters defining linearized stress-strain relationship.

Table 5.1. Material properties used in preliminary tangent modulus, local plastic instability, and gross yield calculations for vessel V-8A

Property	Value
Poisson's ratio, ν	0.3
Uniaxial yield strength σ_{yu}, MPa[a]	413.7
Tensile strength σ'_{ult}, MPa	551.6
Young's modulus E, GPa	206.8
Tangent modulus E_s, GPa	2.068
Yield strain λ_y	0.002 (0.00208 for p − ε curve)
Hardening strain λ_s	0.012

[a]Biaxial yield strength, $\sigma_y = 1.04\ \sigma_{yu}$ = 430.2 MPa.

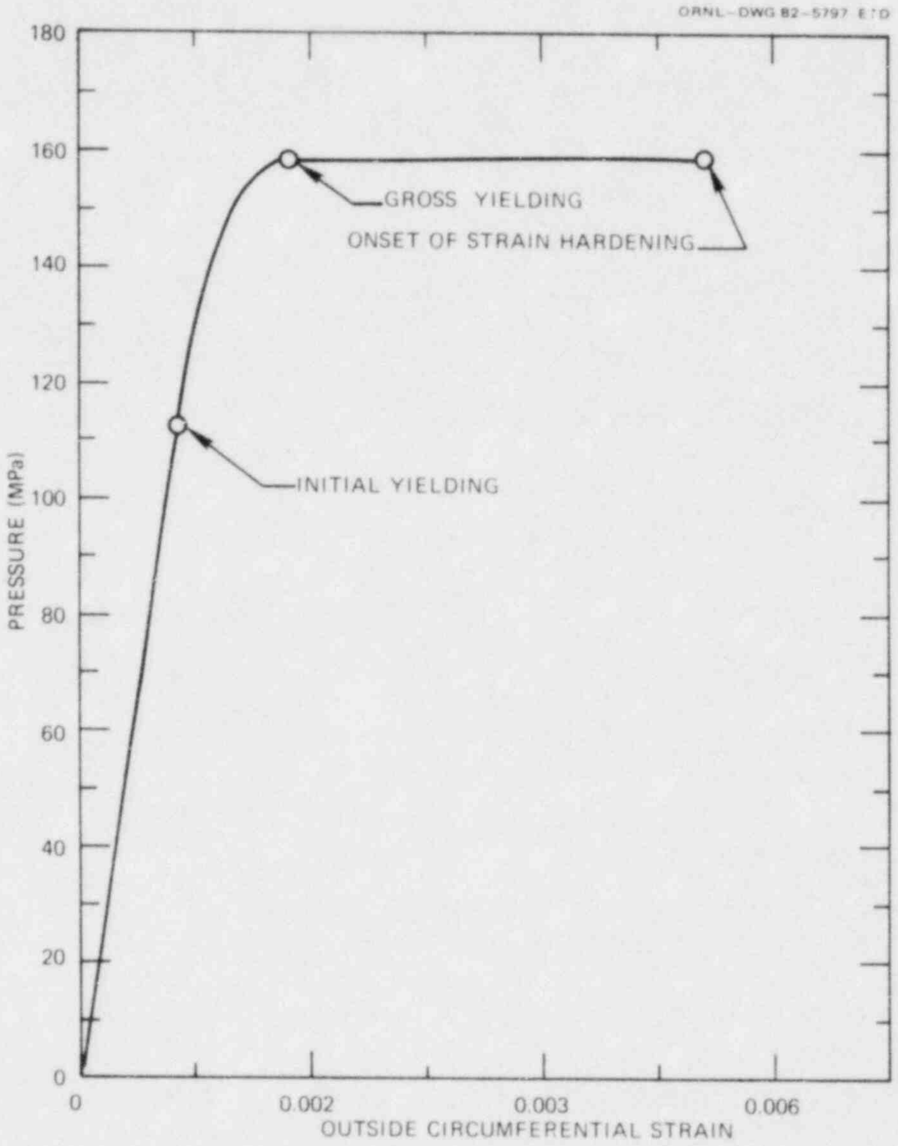

Fig. 5.3. Pressure vs outside circumferential strain for a cylinder of V-8A geometry with properties given in Table 5.1.

or

$$\lambda = \frac{(1 - \nu/2)\ K_I}{CE\ \sqrt{\pi a}} \ , \qquad (1)$$

where K_I is the stress intensity factor, C is the elastic shape factor for surface cracks,[14,15] σ and λ ar[illegible]propriate nominal stress and strain, a is the crack depth, and E is Yo[illegible] modulus. For larger strains the TM method is used to calculate λ [illegible]function of K_I or J_I, the J-integral;

from

$$\lambda = f\ (C,\ a,\ J_I,\ \lambda_y,\ \lambda_s)\ . \tag{2}$$

K_I and J_I are assumed to be related by

$$K_I^2 = EJ_I\ . \tag{3}$$

Tearing resistance J_R for vessel V-8A material is conveniently represented by the power law expression

$$J_R = C(\Delta a)^n\ , \tag{4}$$

where c and n are parameters determined by fitting the expression to specimen test data.

The scheme for using Eqs. (1)–(4) and the p-λ relationship of Fig. 5.3 to find a tearing instability is illustrated in Fig. 5.4. Assume an initial crack depth a_0. For a subsequent depth a_1, values of J_{R1} and p_1 are calculated for the condition $J_I = J_R$. Figure 5.4 shows that, at a constant pressure p_1, a virtual increment in crack depth would cause J_R to increase more than J_I, with the result that $J_R > J_I$. This implies that more energy would be required to generate the virtual extension than could be supplied by the strain energy released; thus, a_1 is a stable crack depth. At crack depths a_2 and a_3 a virtual extension would result in $J_I > J_R$ and a tearing instability. Pressure p_2 is the maximum pressure computed by this procedure and is therefore defined as the tearing instability pressure.

Three J_R curves were selected from preliminary data from the B&W test of characterization specimens for vessel V-8A (Ref. 1). The power-law parameters corresponding to high, medium, and low values are given in Table 5.2. Results of tearing instability computations are shown in Fig. 5.5 for an initial crack depth a_0 = 91.44 mm. The high J_R case gave strains in excess of gross yield but below the strain hardening range. The other two cases indicate tearing instability pressures of 145.3 and 154.7 MPa at crack depths of ~104.7 and 105.7 mm, respectively. The higher pressure is lower than the gross yield pressure, 158.21 MPa.

Also shown in Fig. 5.5 are the local plastic instability pressures[13] as a function of crack depth. For the conditions assumed this shows that a local plastic instability would precede a tearing instability in the medium J_R case.

As a consequence of these analyses the instrumentation plan for the vessel test was altered to include several strain gage rosettes in the vicinity of the flaw. Rosettes will provide a better description of the stress state than the gage layout originally planned. Also, the decision to machine the flaw notch in the vessel to a depth of 70 mm and a length of 280 mm was based on the conclusion that, if the vessel toughness were

ORNL-DWG 82-5798 ETD

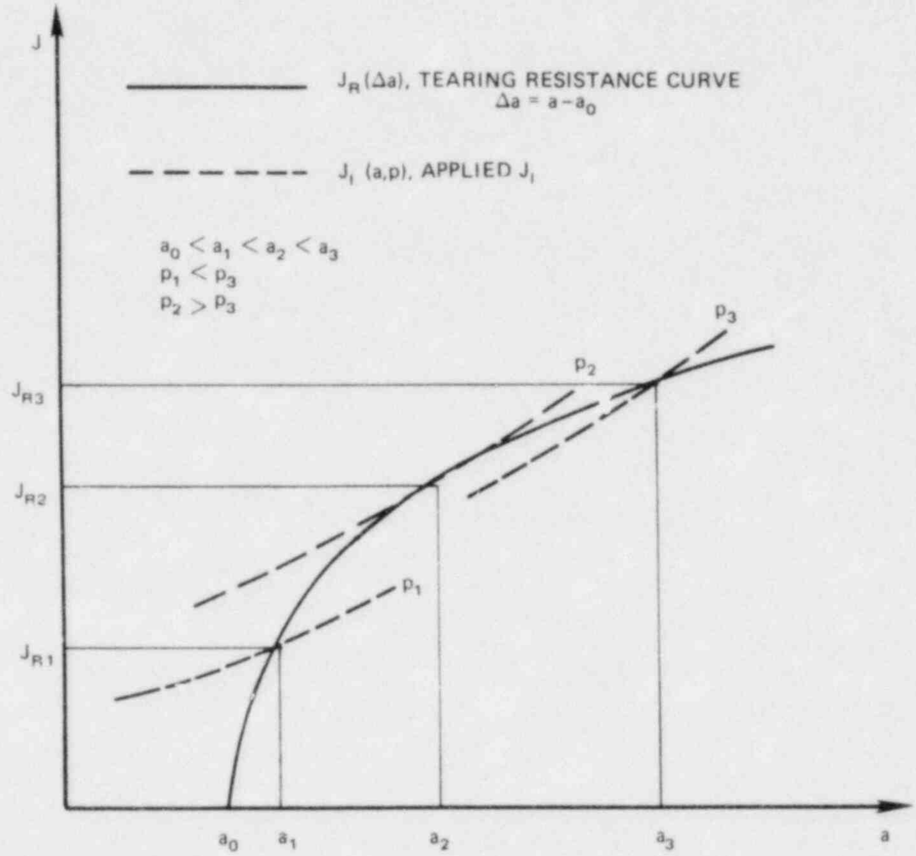

Fig. 5.4. Schematic for determination of J_R-controlled crack depth and tearing instability pressure of a vessel.

Table 5.2. J_R-curve power law parameters for tearing instability estimates[a]

Designation	Specimen No.	C	n
	V852J5	136.33	0.4071
	V862J5	123.72	0.4722
High	Average	130.03	0.4397
Medium	V882J2	124.38	0.3119
Low	V8102J7	92.45	0.2798

[a]Parameters obtained by least-squares fit to B&W data[1] for all points beyond the lower exclusion line. Both J_R and Δa considered random. $J_R = C\,(\Delta a)^{n_R}$, with J_R in kJ/m² and Δa in mm.

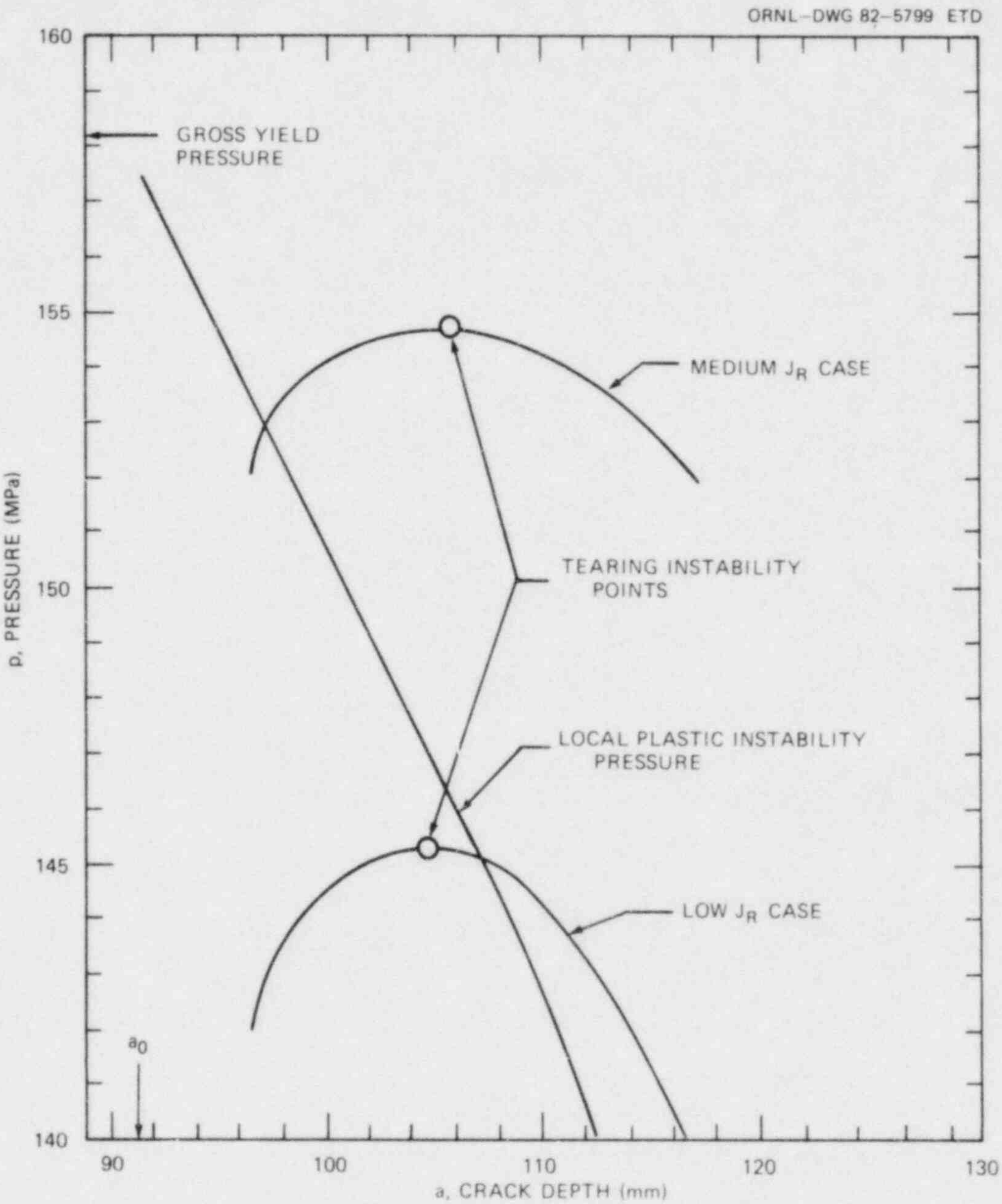

Fig. 5.5. J_R-controlled crack depth vs pressure and local plastic instability pressure of vessel V-8A based on properties given in Table 5.1 and J_R-curve parameters in Table 5.2.

actually as high as the high-J_R case, the vessel would attain gross yield prematurely, a condition that would certainly impair the quality and usefulness of test data.

While the vessel was being flawed the first set of ORVIRT elastic-plastic calculations of J_I were made. The flaw geometry and cases analyzed are defined in Fig. 5.6 and Table 5.3. Initial ORVIRT-3D computations using an incremental plasticity model were abandoned because of the excessive expense of the computations. Deformation plasticity theory was used in all the ORVIRT computations shown in Table 5.3.

The first case, V8EP1, was analyzed with a Ramberg-Osgood stress-strain law

$$\frac{\varepsilon}{\varepsilon_y} = \frac{\sigma}{\sigma_y} + \alpha\left(\frac{\sigma}{\sigma_y}\right)^n , \tag{5}$$

for which the parameters are defined in Table 5.3 (Fig. 5.7). The parameter values for case V8EP1 were taken from the work of Shih et al.[16] at General Electric Company, because measured values[17] for V-8A were not available at the time.

Results of ORVIRT case V8EP1 are shown in Fig. 5.8 in terms of $J_I(\phi)$ in comparison with previous linear-elastic analyses performed with ORVIRT and with the Raju-Newman equations.[18,19] At pressures below about 75 MPa there is little difference between linear-elastic and elastic-plastic distributions $J_I(\phi)$. Figure 5.8 shows that at higher pressures the linear-

ORNL-DWG 82-5800 ETD

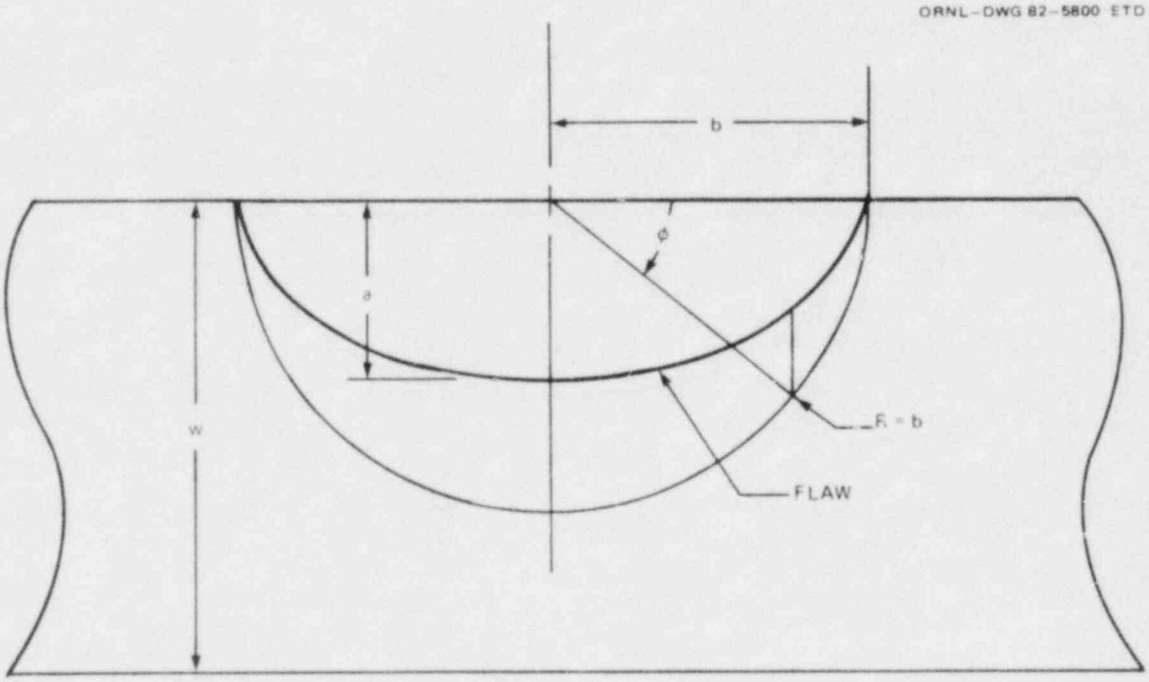

Fig. 5.6. Definition of flaw geometry for analyses of vessel V-8A.

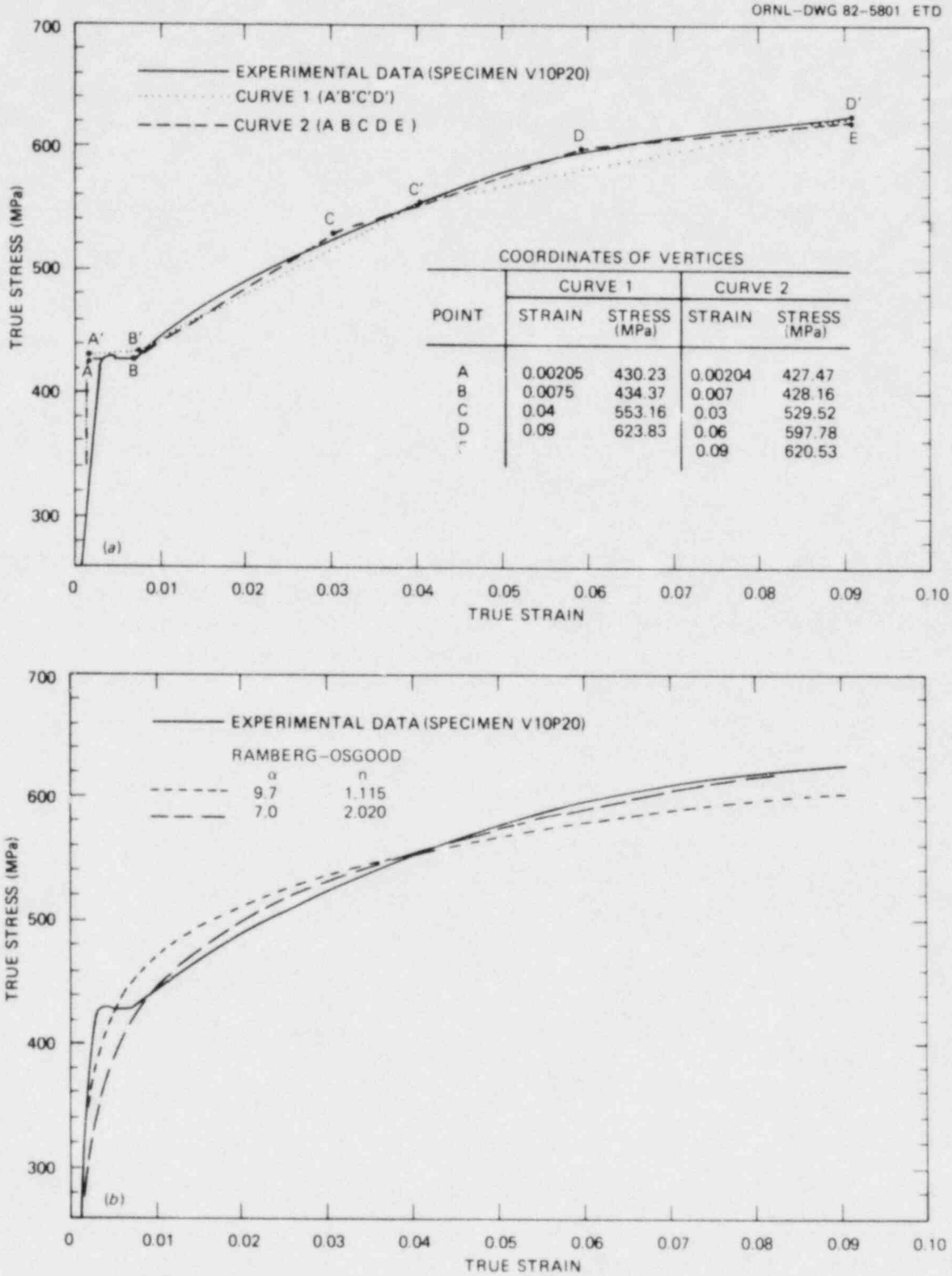

Fig. 5.7. Uniaxial true stress-strain curve of tensile specimen V10P20 tested at 149°C. The four stress-strain relationships used in ORVIRT analyses are also shown. (a) Piecewise linear; (b) Ramberg-Osgood.

Table 5.3. ORVIRT-3D elastic-plastic computations for vessel V-8A

Case No.	a (mm)	b (mm)	E (MPa)	σ_y (MPa)	Ramberg-Osgood parameters[a] n	Ramberg-Osgood parameters[a] α	Piecewise linear $\sigma - \varepsilon$ representative curve No.
V8EP1	101.60	152.40	206,843	427.5	9.7[b]	1.115[b]	
V8EP2	101.60	152.40	209,600	401.3	7.0[c]	2.020[c]	
V8EP3	101.60	152.40	209,600	430.2			1[d]
V8EP4 to 7			209,600	427.5			2[d]
V8EP4	101.60	152.40					
V8EP5	95.52	152.40					
V8EP6	91.44	139.70					
V8EP7	96.52	139.70					
Large deformation[e]	101.60	152.40					

[a] $\varepsilon/\varepsilon_y = \sigma/\sigma_y + \alpha(\sigma/\sigma_y)^n$; $\varepsilon_y = \sigma_y/E$.

[b] Ref. 16.

[c] V-8A data by Stelzman.[17]

[d] Curves in Fig. 5.7.

[e] ADINA only run for large deformations.

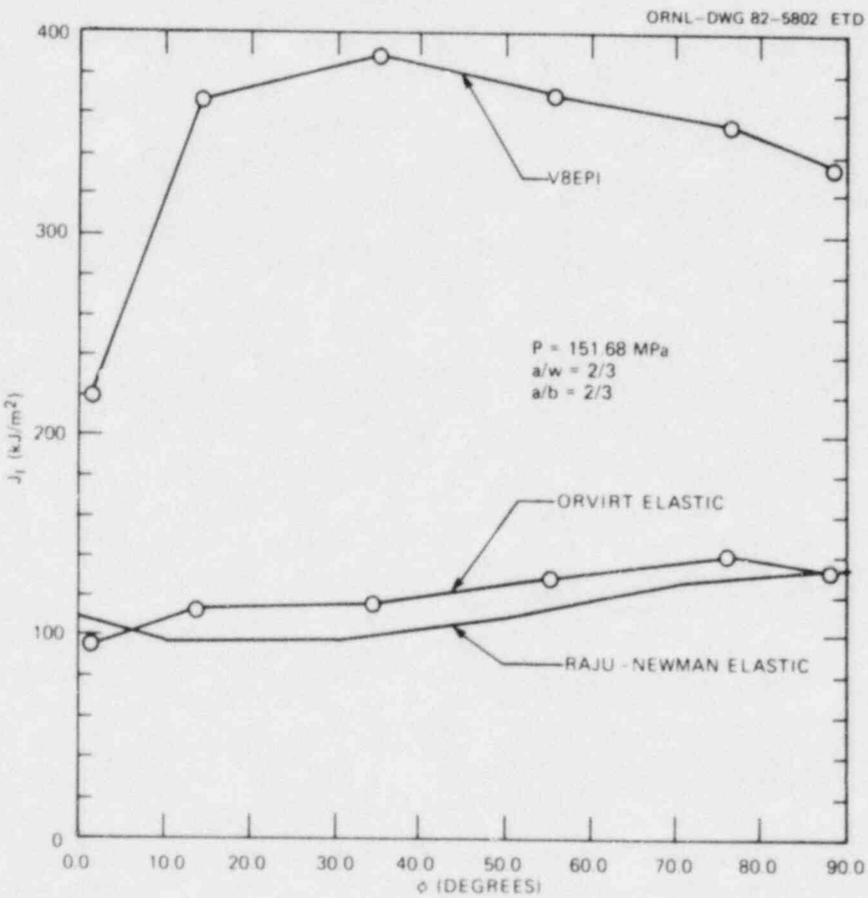

Fig. 5.8. Results of ORVIRT case V8EP1 (elastic-plastic) compared with linear elastic values from ORVIRT and Raju-Newman expressions.

elastic result can be a very poor representation of J_I. This divergence from LEFM may be reasonably represented by the TM method, but this method will have to be used discreetly because the method usually employs elastic shape factors. The elastic-plastic analyses all show a shifting of the $J_I(\phi)$ distribution with increasing pressure.

Another factor investigated is the influence of variations of the stress-strain relationship on calculated deformations and J_I. ORVIRT cases V8EP1, 2, 3, and 4 represent four different relationships for the same crack geometry. The assumptions are shown graphically in comparison with experimental data in Fig. 5.7.

The CMODs shown in Fig. 5.9 indicate the importance of an accurate stress-strain representation. Here two different Ramberg-Osgood cases, V8EP1 and 2, are compared with a case (V8EP3) based on a very good stress-

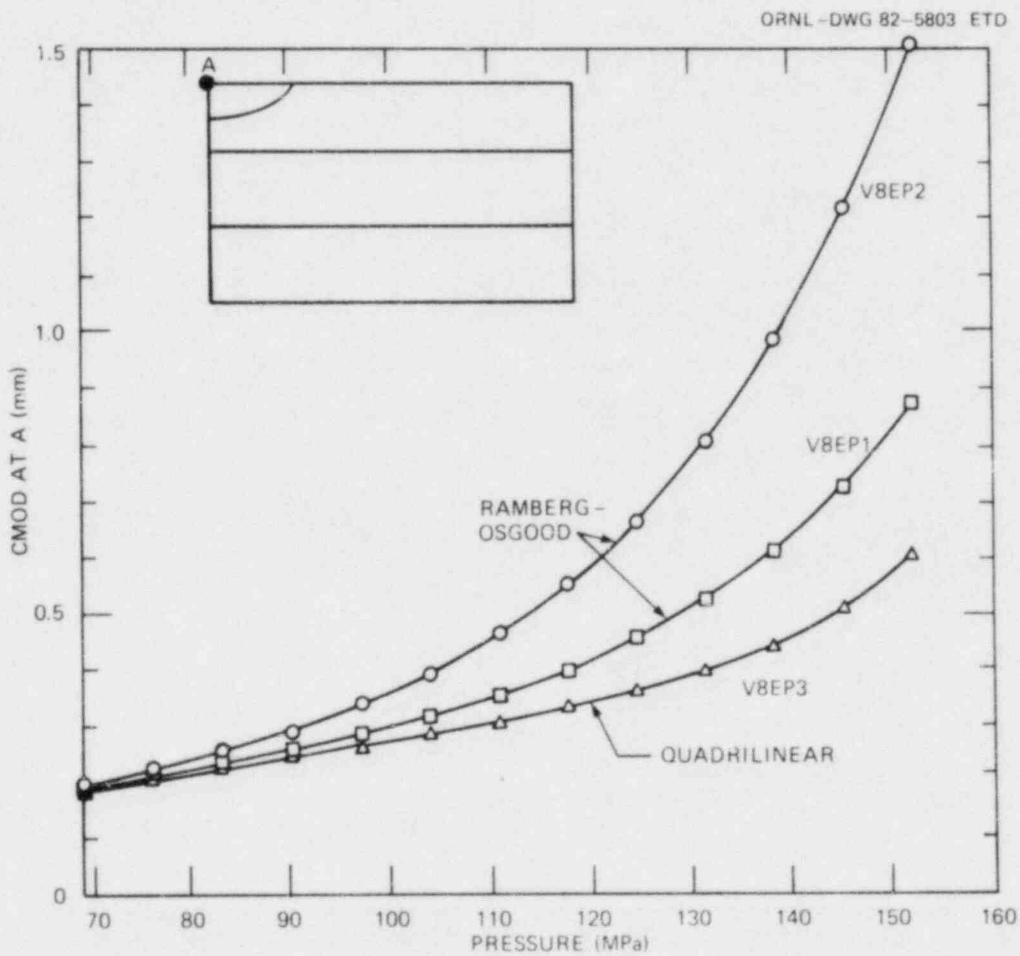

Fig. 5.9. A comparison of CMOD calculated by ORVIRT for three stress-strain relationships: two Ramberg-Osgood cases and one piecewise linear case. Note the relatively large overestimate of displacement in the V8EP2 case, using the Ramberg-Osgood parameters that give the best fit to the stress-strain curve.

strain representation. Figure 5.9 shows that the Ramberg-Osgood parameters that gave a poorer representation of stress-strain produced CMOD much closer to that of case V8EP3. One conclusion is that the stress-strain representation in the low strain range is very important. Consequently, it was decided that the Ramberg-Osgood law, which is convenient for computations, could not be used in the V-8A analysis, because it implicitly is a poor representation near the elastic range.

Figures 5.10 and 5.11 compare J_I values based on the three stress-strain relationships that fit V-8A data best. Again this indicates that a Ramberg-Osgood curve that fits the data well gives poor results. The comparison of cases V8EP3 and 4 in this figure suggests that details of the fit beyond the yield stress are not very important.

ORVIRT-3D calculations were made for a set of four crack geometries and a single stress-strain representation, the piecewise linear curve 2 of Fig. 5.7. The results of these four cases, V8EP4 to 7, are presented in Figs. 5.12–5.15 in terms of J_I (ϕ,p). The crack depths and lengths include some of the cases previously analyzed by the LEFM and TM methods. Results obtained by ORVIRT and the simplified methods need further study and application to V-8A tearing resistance data. However, a preliminary conclusion at this time is that the ORVIRT results indicate that J_I will be slightly higher than the values implied by the particular LEFM and TM

ORNL-DWG 82-5804 ETD

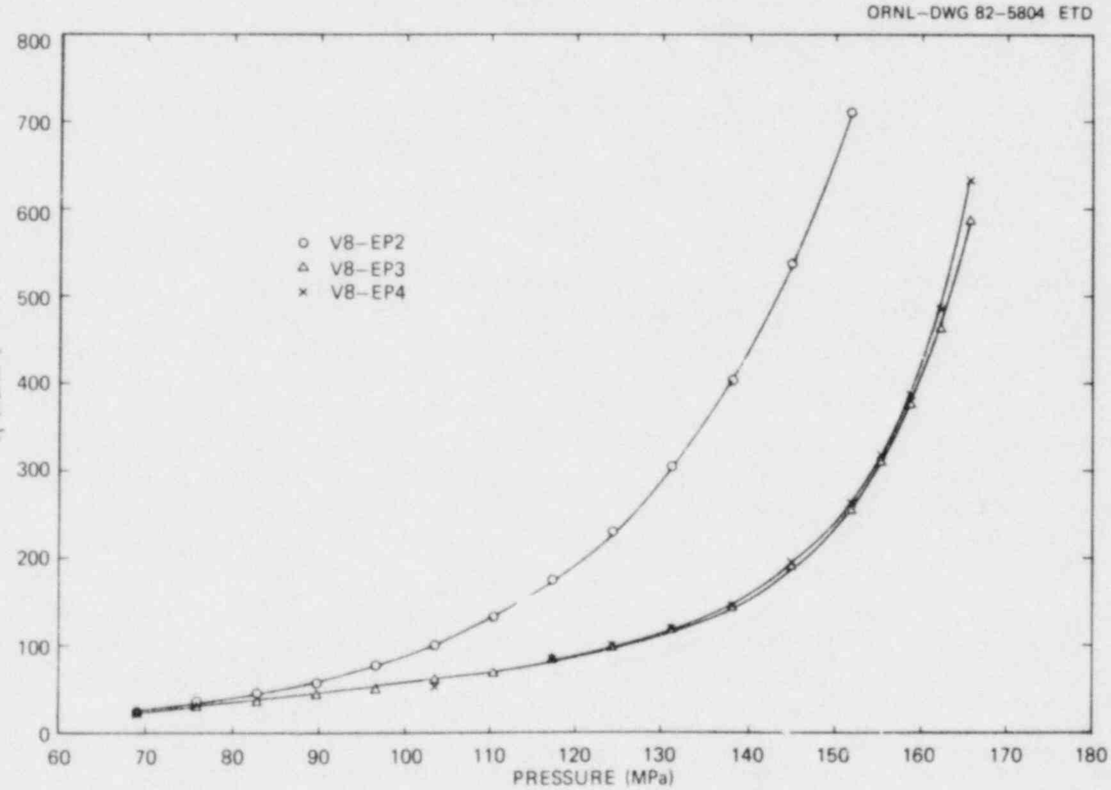

Fig. 5.10. J_I at ϕ = 34.62° vs p, a comparison of three ORVIRT cases with parameters producing the best fits to the stress-strain curve.

ORNL-DWG 82-5805 ETD

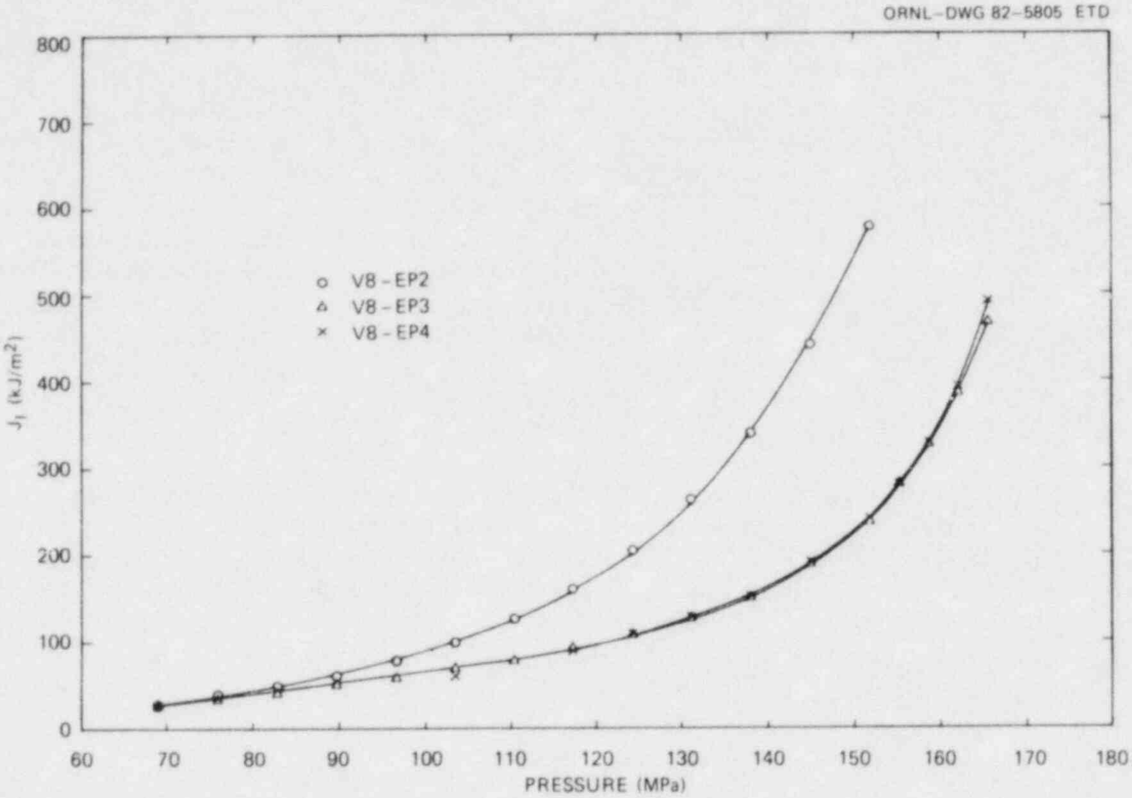

Fig. 5.11. J_I at ϕ = 88.27° vs p, a comparison of three ORVIRT cases with parameters producing the best fits to the stress-strain curve.

analyses described herein. Furthermore, the CMOD behavior shown in Fig. 5.16 for the crack geometries analyzed by ORVIRT indicate that a local plastic instability is beyond 165 MPa. With adjustment for the higher yield strength used in the ORVIRT calculation, it appears that the earlier estimate of local plastic instability is slightly low. The plot of outside circumferential strain as a function of pressure shown in Fig. 5.17 indicates good agreement with the theoretical solution of the elastic perfectly plastic cylinder.

In preparation for a more detailed analysis of the V-8A flaw, the J_R-curve data reported by B&W were evaluated statistically, as reported previously.[18] The J_R vs Δa curves for the average power-law parameters are plotted in Figs. 5.18 and 5.19 (see Table 5.4) to show the essential differences among the sets of data. Figure 5.18 shows the results of three statistical assumptions, namely considering the random variable to be (1) J_R, (2) Δa, or (3) both J_R and Δa. The influence of this choice on the J_R curve is very small. The figure also shows the effect of the selection of the Δa domain of data included in the curve-fitting calculation.

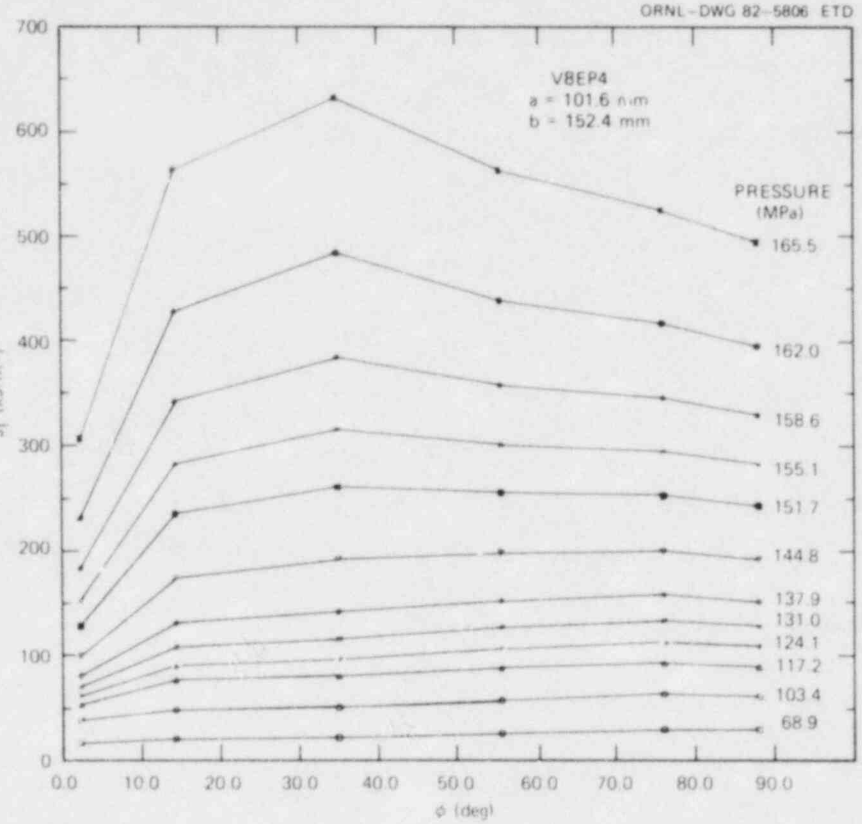

Fig. 5.12. J_I vs ϕ and p for ORVIRT case V8EP4.

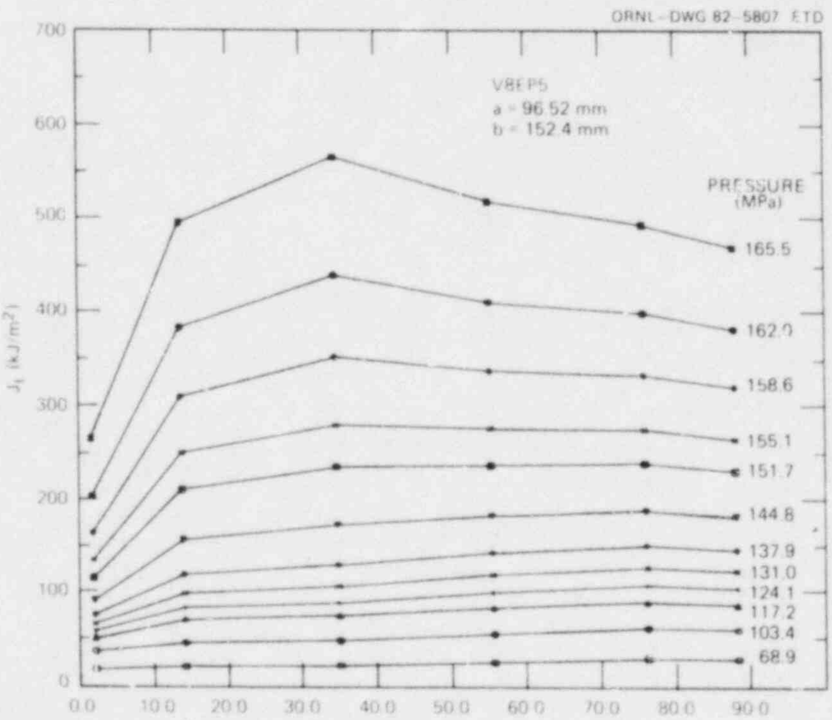

Fig. 5.13. J_I vs ϕ and p for ORVIRT case V8EP5.

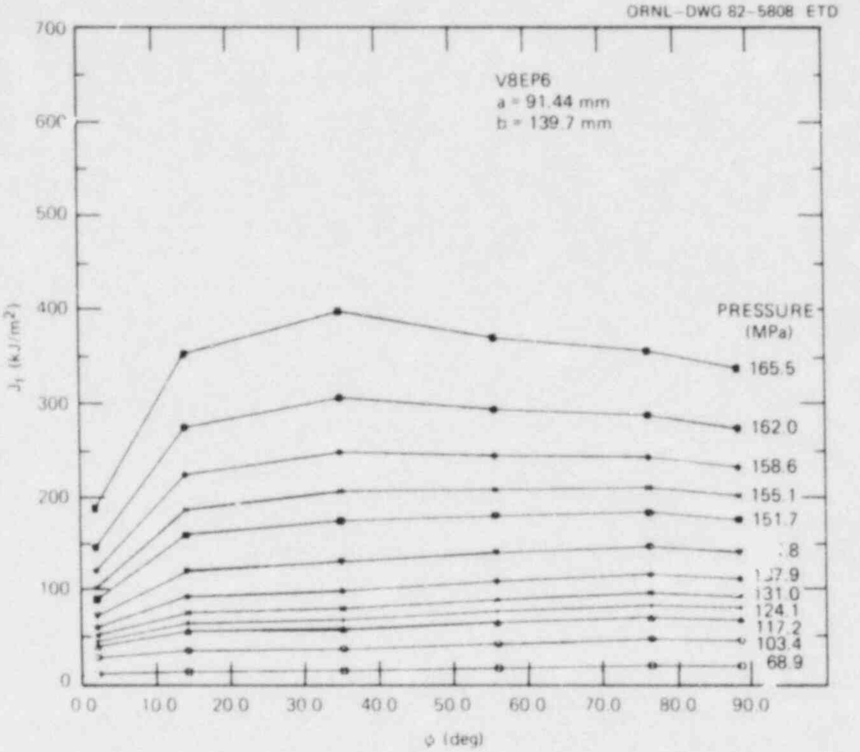

Fig. 5.14. J_I vs ϕ and p for ORVIRT case V8EP6.

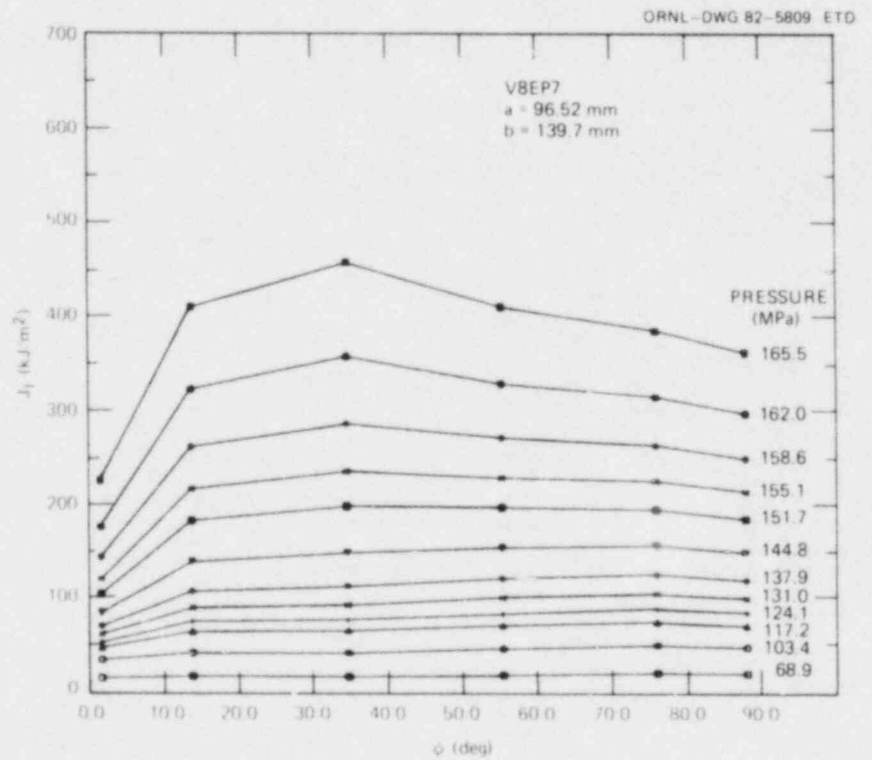

Fig. 5.15. J_I vs ϕ and p for ORVIRT case V8EP7.

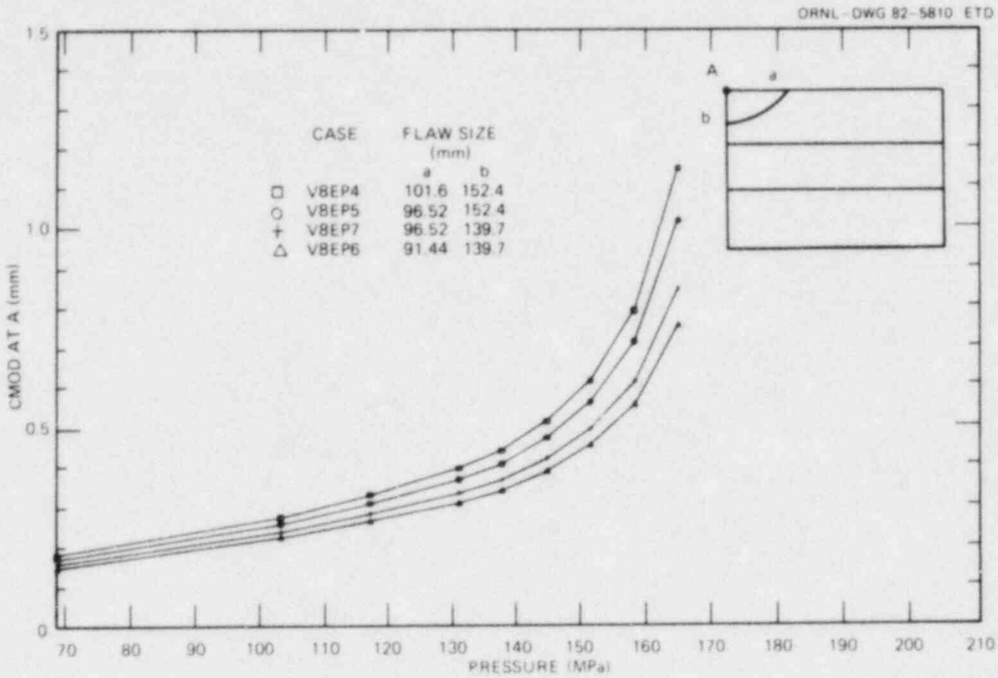

Fig. 5.16. CMOD vs p for four different crack geometries. The tendency toward a local plastic instability is shown by the increasing slope (dCMOD/dp) with increasing pressure and crack size.

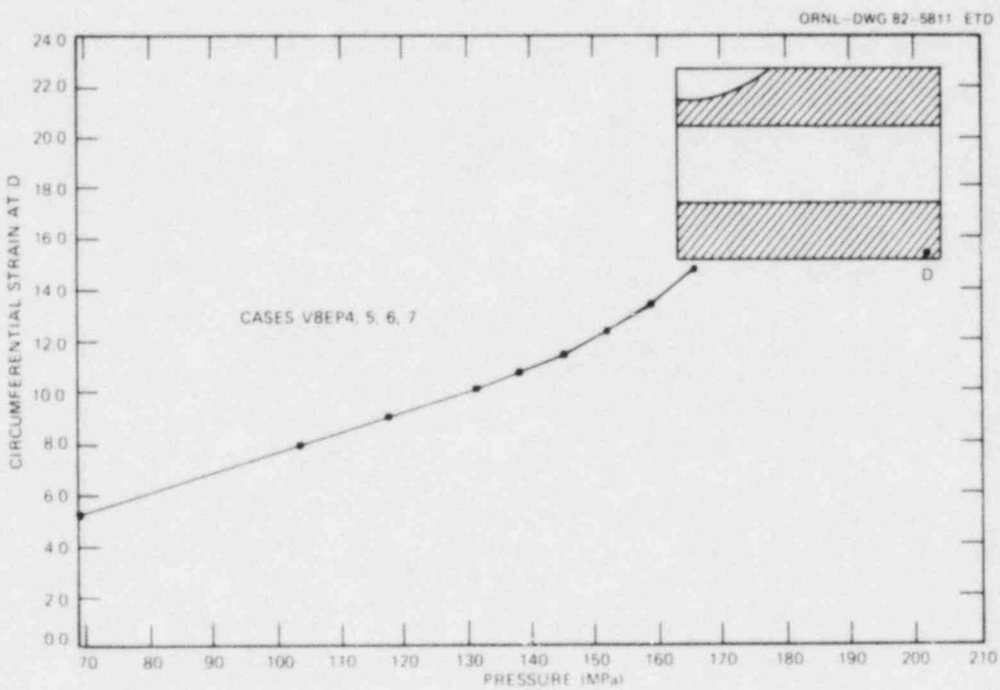

Fig. 5.17. Outside circumferential strain vs p at a point remote from the flaw.

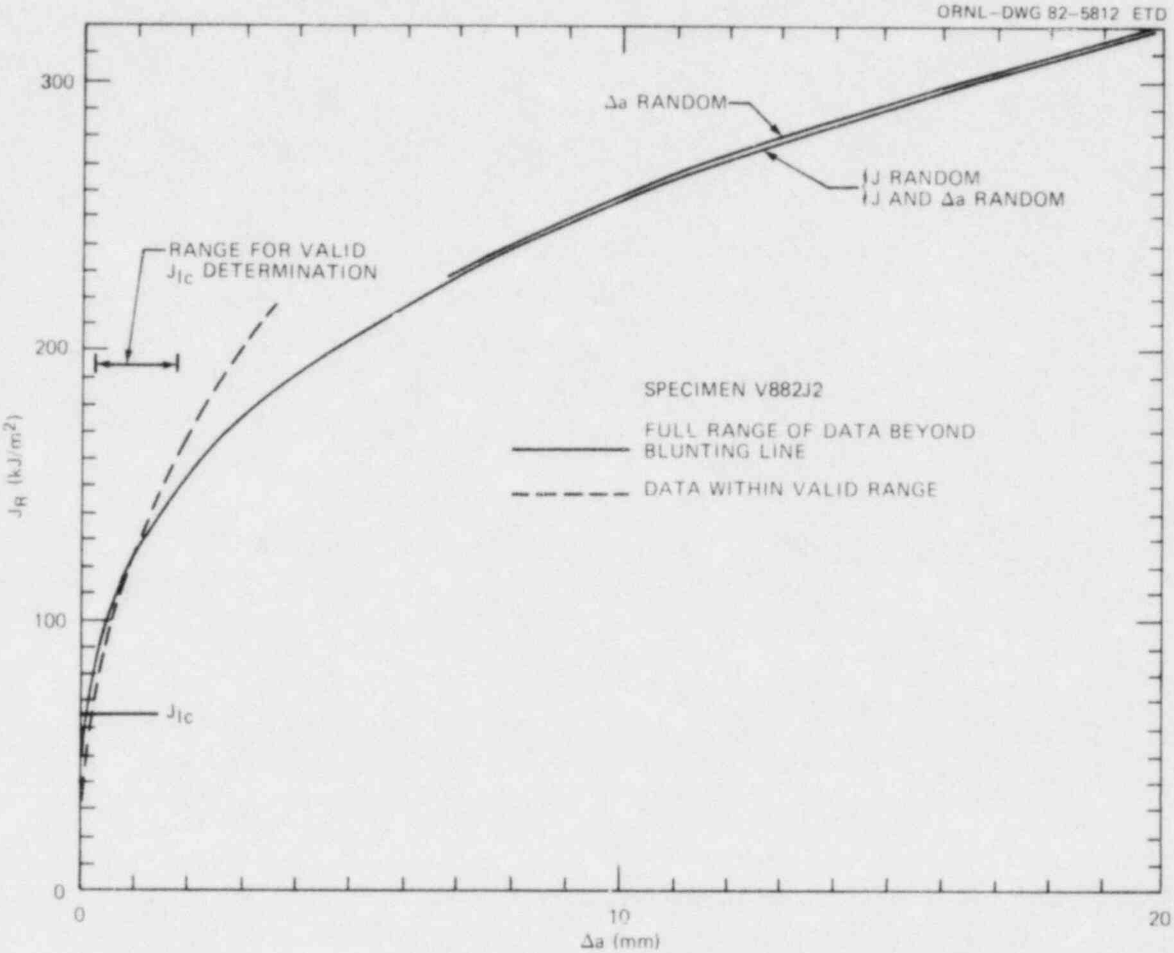

Fig. 5.18. Power law J_R curves for specimen V882J2. The set of curves represents four different least-squares fits.

Table 5.4. Average J_R-curve power law parameters for each V-8A characterization weld[a]

Characterization weld No.	Number of specimens[b]	$\bar{C}$	$\bar{n}$
V852	5	137.853	0.3862
V862	6	134.044	0.4509
V882	2	122.981	0.3418
V8102	10	89.316	0.3080

[a] $\bar{C}$ and $\bar{n}$ are unweighted averages of the power law parameters C and n obtained by least-squares fit to B&W data[1] for all points beyond the lower exclusion line with J_R considered random

$J_R = C\,(\Delta a)^n$ with J_R in kJ/m², Δa in mm .

[b] Specimens tested at 149°C.

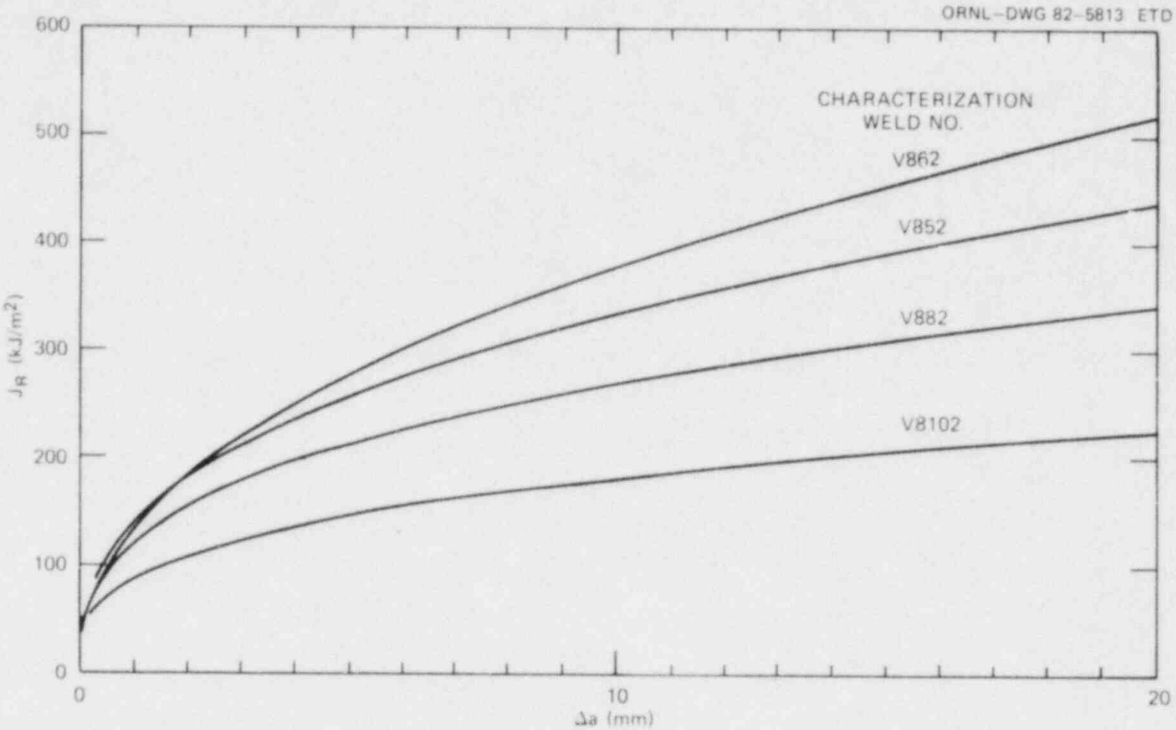

Fig. 5.19. J_R curves for average power law parameters for each of the four V-8A characterization welds at 149°C. See Table 5.4 for values of the parameters.

5.1.4 V-8A flaw preparation

P. P. Holz, K. K. Klindt, and J. E. Batey

On the basis of fracture analyses discussed in the preceding section dimensions of the machined notch and tentative objectives for fatigue crack extension of that notch were selected. Machining and cyclic pressurization of the notch were accomplished by procedures used in two earlier trials of the flaw preparation procedure.[8,20] The objective of the procedure was to produce a fatigue-sharpened flaw of approximately semielliptical profile.

The machining operations consisted of first machining a flat on the vessel, centered on the special low-upper-shelf seam weld, as shown in Fig. 5.20. Then a notch of dimensions and shape shown in Fig. 5.21 was cut in a radial-axial plane of the vessel in the center of the special seam weld.

The fatigue sharpening of the notch was initiated with the objective of attaining crack growth of 21.6 mm at the deepest point of the flaw. However, the depth actually accepted was contingent on the profile of the flaw maintaining a reasonable shape. This was a special concern, because in the flawing trials both asymmetrical crack growth and unexpectedly rapid growth had been observed.

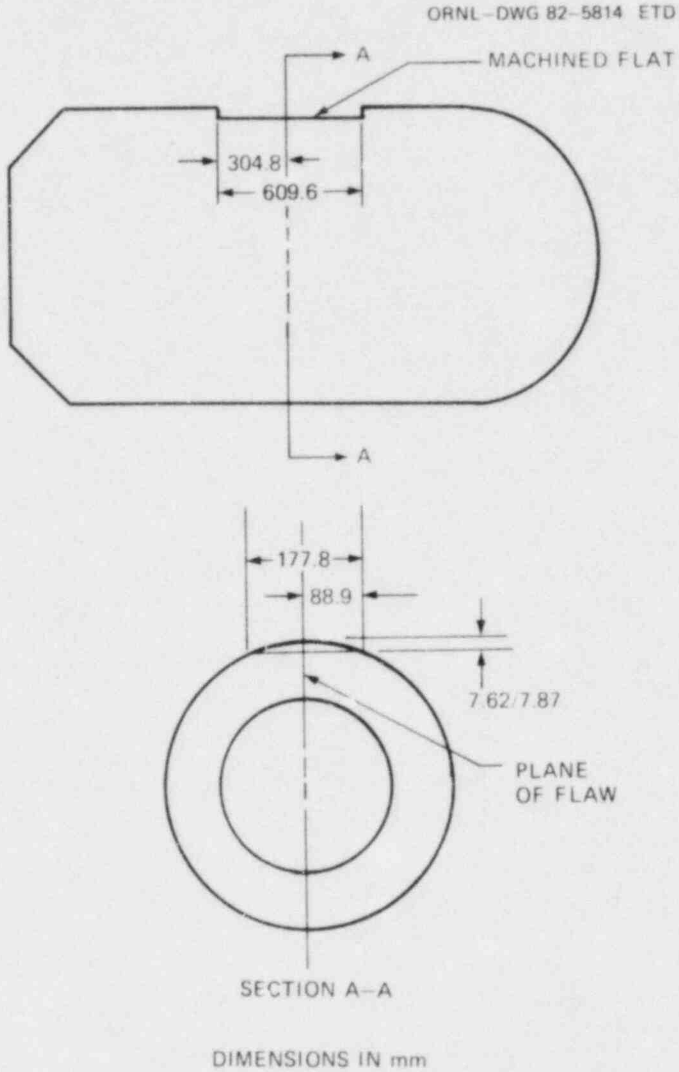

Fig. 5.20. Dimensions of machined flat at flaw site in vessel V-8A.

The vessel was instrumented with ultrasonic transducers mounted on the inside surface of the vessel in positions (Fig. 5.22) from which measurements of crack growth could be observed. Pressurization apparatus was mounted as shown in Fig. 5.23 so that high pressure could be applied to the machined notch.

Pressure was applied cyclically to the notch, and ultrasonic measurements were made continuously. The maximum pressure p_{max} in each cycle was limited to keep K_I well below K_{Ic}. Intermittently, the pressure cycles were changed to produce beach marks on the fatigued fracture surface. The schedule of p_{max} vs number of cycles is given in Fig. 5.24.

The successive observations of crack growth during pressurization are presented in Figs. 5.24 and 5.25. The process was stopped after 105,331 cycles with an indicated crack growth of 21.3 mm. Figure 5.26 is a view of the machined notch and a portion of the surrounding machined flat.

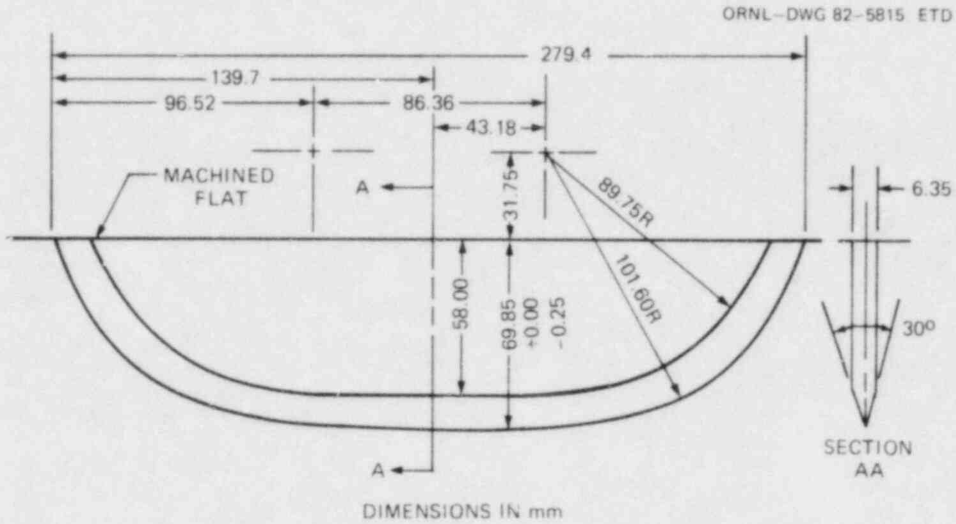

Fig. 5.21. Configuration of V-8A machined notch, a sectional view of the radial-axial plane of the vessel that is the plane of symmetry of the flaw.

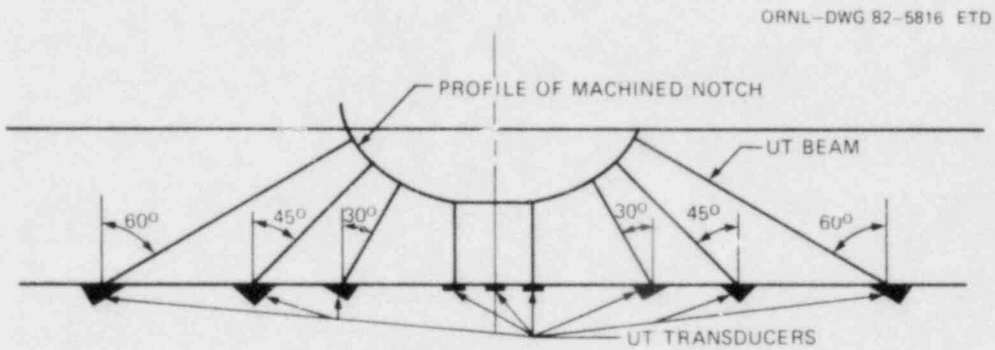

Fig. 5.22. Sectional view of the profile of the V-8A machined notch with locations of ultrasonic (UT) transducers used to measure fatigue crack growth.

5.1.5 Vessel V-8A instrumentation

R. H. Bryan

Instrumentation studies for the V-8A test have been under way for more than a year. An important objective of this work was to identify and develop means of measuring the crack shape and size during the vessel test. Other special problems were concerned with

1. sensors designed to function under high pressure (to ~200 MPa) at temperatures higher than any previously attained in intermediate vessel tests, up to 150°C;
2. sensing tearing or structural instability; and
3. synchronizing the recordings of widely varying types of measurements.

ORNL–PHOTO 8132–82

Fig. 5.23. Intermediate test vessel V-8A with apparatus used to cyclically pressurize the machined notch.

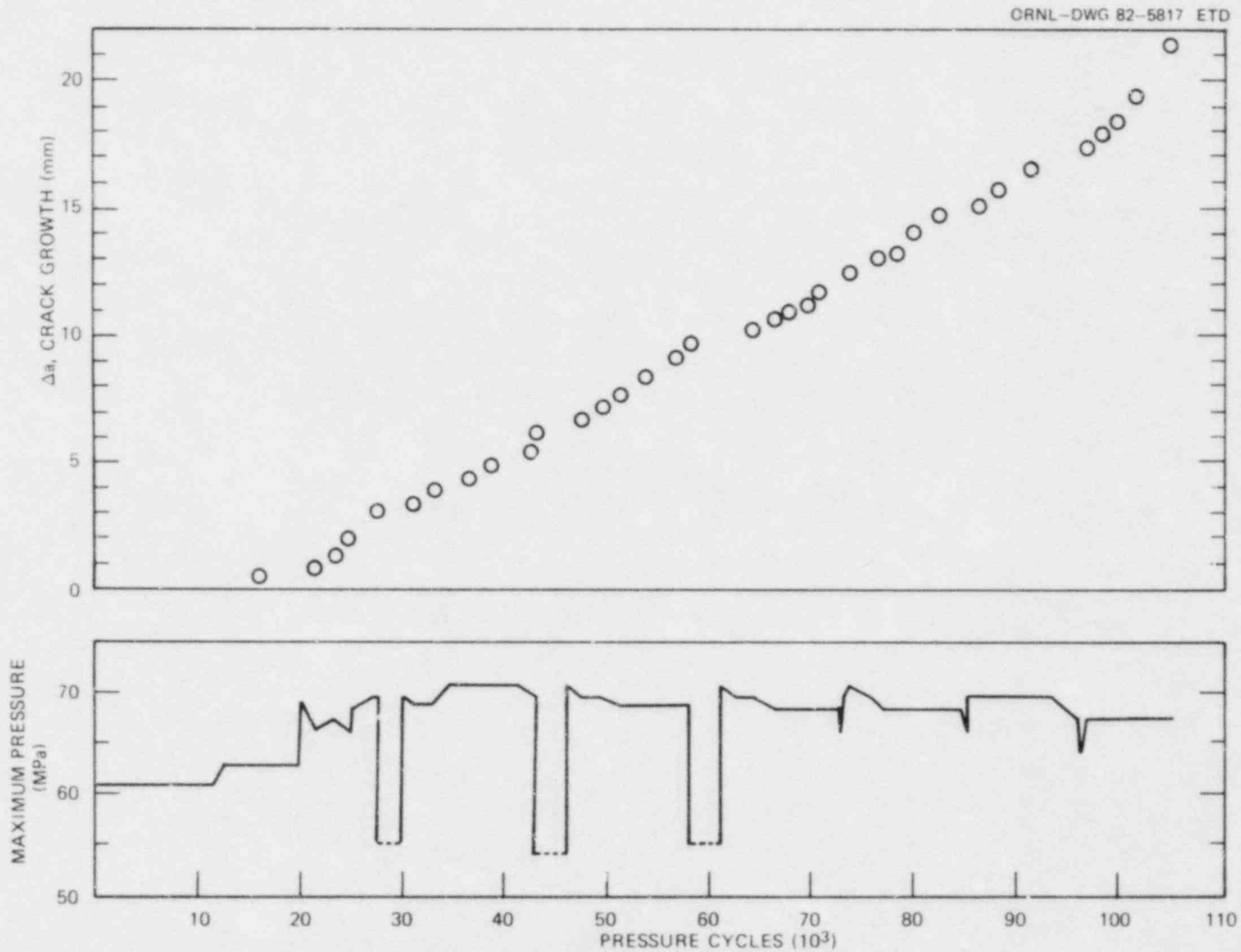

Fig. 5.24. Maximum cyclic pressure p_{max} and crack growth Δa at deepest point of flaw vs number of cycles.

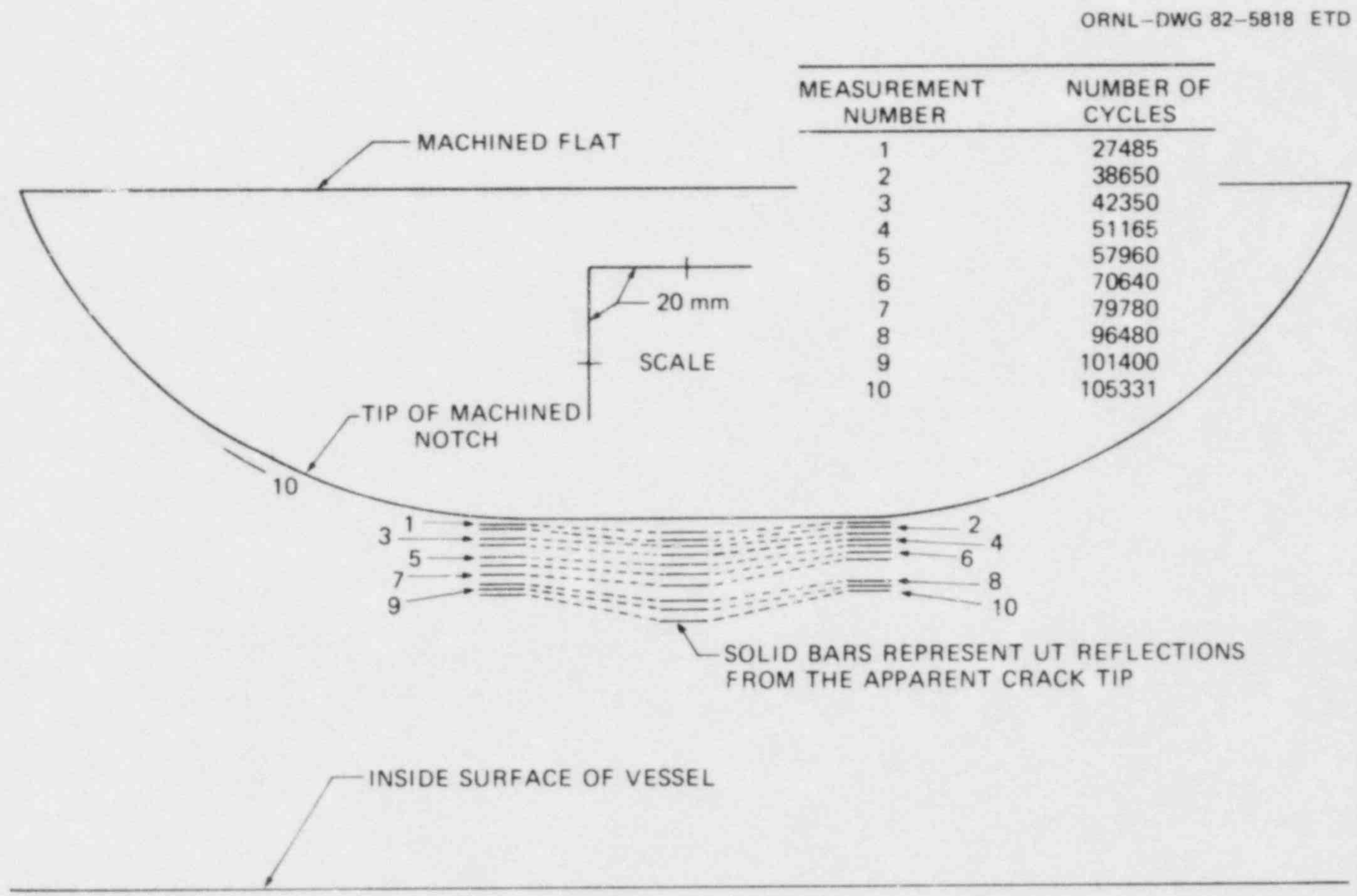

MEASUREMENT NUMBER	NUMBER OF CYCLES
1	27485
2	38650
3	42350
4	51165
5	57960
6	70640
7	79780
8	96480
9	101400
10	105331

Fig. 5.25. A scale plot of locations of UT reflections from the crack tip at several stages of crack growth.

ORNL-PHOTO 8135-82

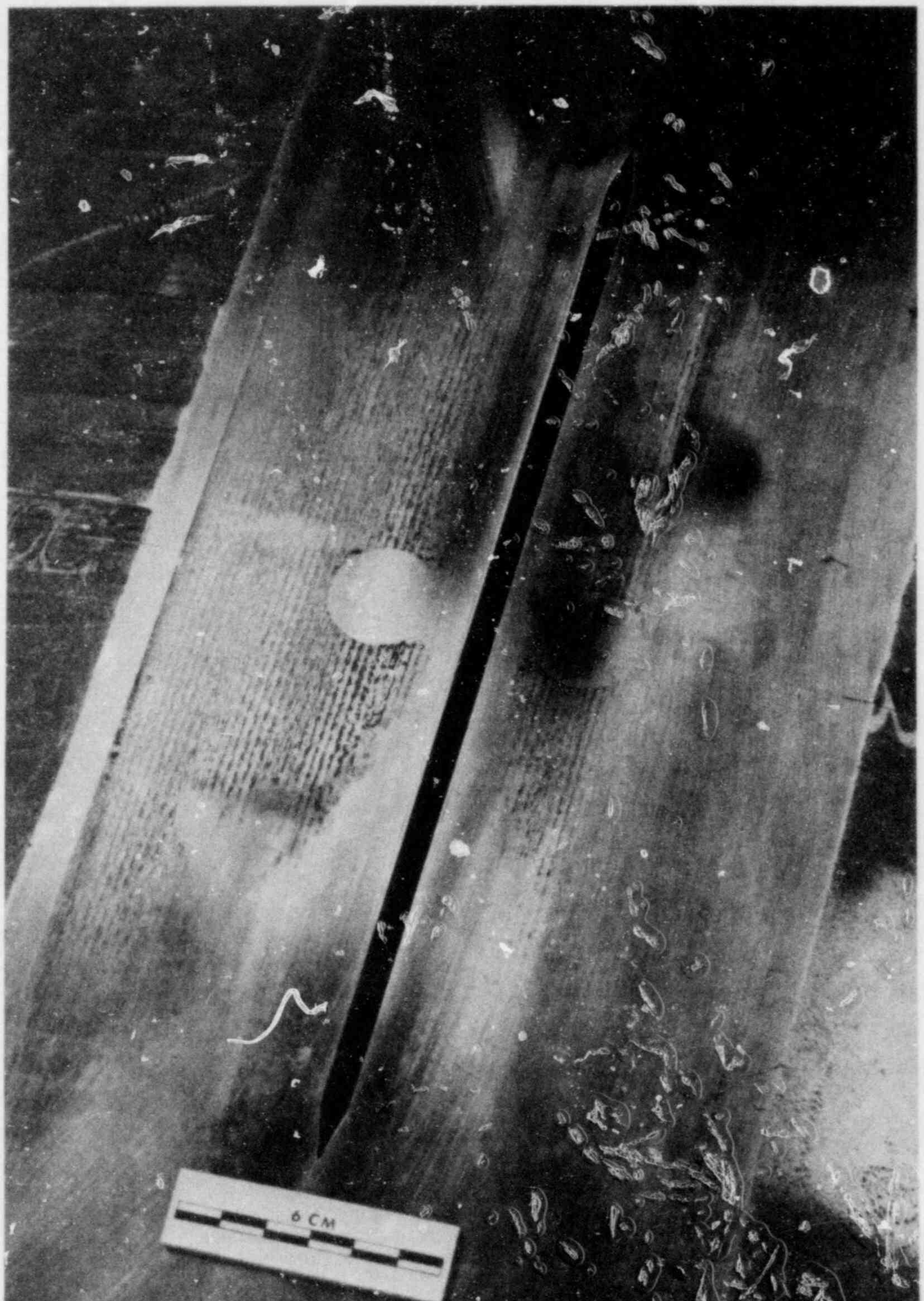

Fig. 5.26. Machined and fatigue-sharpened flaw in vessel V-8A.

The instrumentation plan adopted is based on the use of methods and devices that are well developed in terms of objective and quantitative interpretation of data and are adaptable to the vessel test environment. Beach marking and potential drop methods of measuring crack geometry were investigated and partially developed but were abandoned.

The sensor and data acquisition features of the V-8A instrumentation are presented in Table 5.5. These include the features necessary for test control, real-time evaluation of test results, and data recording for post-test evaluation and analysis.

Pressure and temperature indications will be used for control. In addition, a CMOD-pressure variable $d/dt \ \mathrm{Ln}\ (\mathrm{CMOD}/p^2)$ will be produced and used as an indicator of incipient instability so that the vessel can be depressurized manually at the proper time.

During the test, estimates of crack size and shape will be made from CMOD measurements and ultrasonic (UT) observations of the crack tip. CMOD

Table 5.5. V-8A instrumentation output assignments

Variable	Location of sensors on vessel	Number of sensors	Primary recording device[a]	Secondary output	
				Device[a]	Number of channels
Temperature	Inside	4	CCDAS		
	Outside	13	CCDAS		
	Outside	16	Strip chart[b]		
Pressure	Static line	2	CCT	Plotter	1
				Strip chart	1
				Digital display	1
		1	Video tape	Visual	1
Strain	Inside - F[c]	41	CCDAS	Strip chart	1
	Outside - F[d]	42	CCDAS	Strip chart	2
	Inside - other	8	CCDAS	Plotter	1
	Outside - other	13	CCDAS	Plotter	1
	Outside	3	Vishay		
CMOD	Crack mouth	4	CCDAS (8 channels)	Plotter	4
				Strip chart	1
				Digital display	1
d/dt Ln (CMOD/p^2)	e	1	Strip chart Digital display	CCDAS	1
Ultrasonic	Inside - F[c]	7	Video tape[f]	Oscilloscope	

[a]CCDAS: computer-controlled data acquisition system with time base. Scanning rate is 10,000 points/s. Recording rate is variable. Strip chart: variable vs time. Vishay: printed paper tape on manual command. Plotter: variable plotted vs pressure.

[b]At heater control panel.

[c]Inside vessel near flaw.

[d]Outside vessel near flaw.

[e]Derived from sensors specified for CMOD and pressure.

[f]Video section of tape records UT signal; audio section records time code.

will be measured during small decrements of pressure, and the resultant data will be output to plotters displaying CMOD vs p. The elastic response of CMOD will be correlated with precalculated CMOD changes for various crack sizes. The resolution of the UT and CMOD measurements of crack depth is expected to be on the order of 1 mm. Crack size and pressure will be compared with pretest calculations continually in order to know whether instabilities are imminent.

All measurements made during the test will be recorded. The principal recording media for posttest evaluation will be magnetic tapes of digital data produced by a computer-controlled data acquisition system (CCDAS) and video tapes for UT data. The records on the two types of tapes will be synchronized by writing a time code on the UT tapes by a time code generator set to the CCDAS clock time. The data recording scheme presented in Table 5.5 provides redundancy, diversity, and dispersion of sensors, recording devices, and other apparatus to minimize the adverse impact of equipment malfunctions.

Generally the test will not proceed if the CCDAS is not functioning properly, but if the CCDAS should fail after the test has reached a point of no return, there will be independent recordings of pressure, all CMODs, and some strains. Also two magnetic tapes of the CCDAS data will be written simultaneously to protect against accidental loss of those records.

5.2 Pressurized Thermal-Shock Studies

G. C. Robinson R. W. McCulloch

The pressurized thermal-shock (PTS) test concept, described in earlier reports,[21-23] provides a means to obtain realistic flaw behavior and fracture information under combined pressure and thermally induced stresses. During this report period primary activities have been associated with determination of the costs and schedule for facility design and construction and in the continuation of analysis leading towards a realistic, achievable test matrix of HSST ITV under established criteria.

5.2.1 Test facility design and construction

Criteria have been established on which the Pressurized Thermal-Shock Test Facility (PTSTF) design is based,[23] and the operation has been summarized.[21,22] However, as design has progressed, several facility changes have been required. These changes are primarily associated with the application of coolant to the ITV and center around the possible nonuniformity of the surface heat transfer coefficient h as a function of time and position and on the effect of thermal shock on the test tank that contains the ITV. It is useful to briefly summarize the ITV test sequence prior to discussion of design changes.

Figure 5.27 shows the flow diagram of the HSST program PTSTF in its present configuration. The ITV, containing a flaw (or flaws) on its outer surface, is housed in a test tank that enables it to be preheated to a

ORNL-DWG 82-5819 ETD

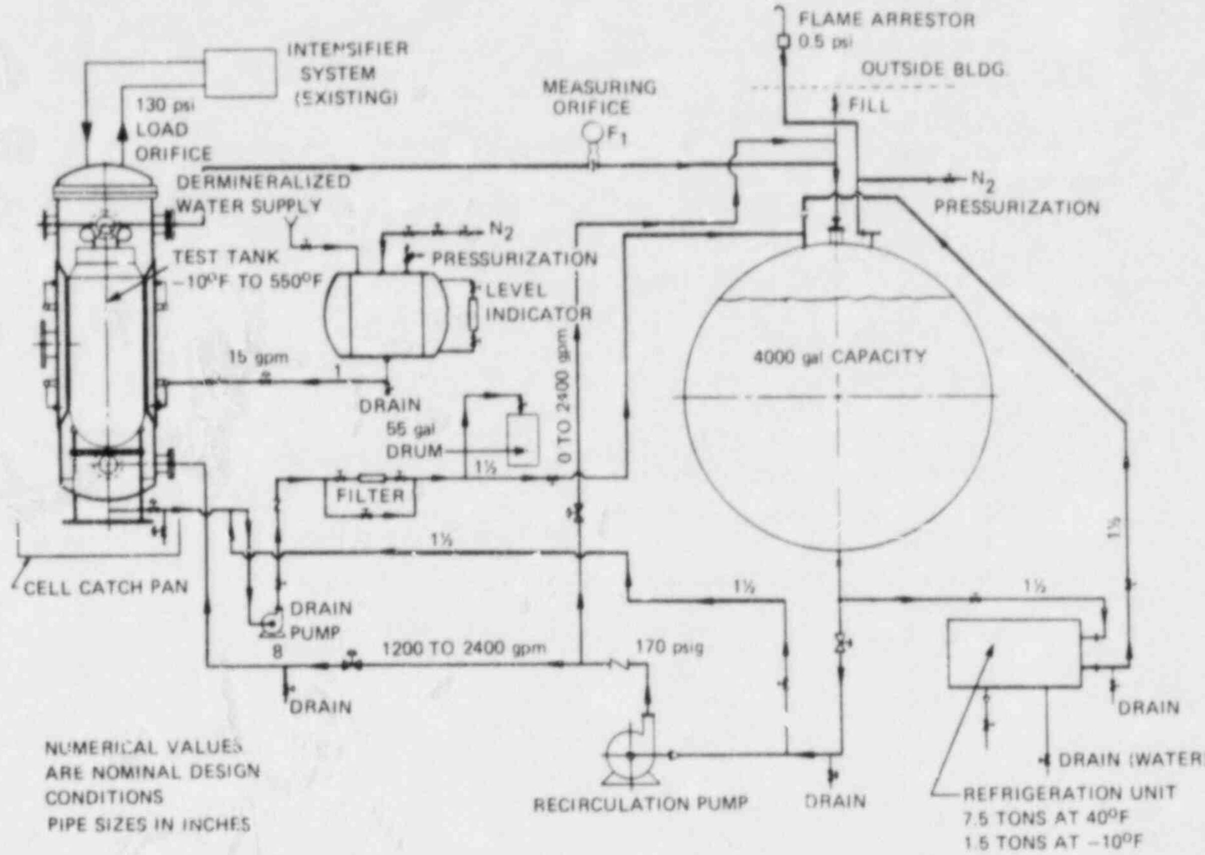

Fig. 5.27. Flow diagram of pressurized-thermal-shock test facility, Bldg. K-702, Oak Ridge Gaseous Diffusion Plant.

uniform temperature of 288°C prior to application of test pressure and coolant. During the heatup phase, the ITV is internally pressurized by the intensifier system at a level sufficient to prevent boiling of the pressurizing liquid. After isothermal conditions are attained and just prior to thermal-shock initiation, heater power is removed, and jacket cooling water is injected into the precooling chamber to cool test tank walls adjacent to the ITV to ~100°C. The required thermal shock to the ITV is then attained by injecting a 40 wt % methanol and 60 wt % water coolant mixture through the annulus between the test tank and ITV. The coolant is prechilled to approximately −23°C and is pumped through the nominal 6.35-mm annular gap at a velocity sufficient to establish a minimum heat transfer coefficient h of 4000 to 6000 $W \cdot m^{-2} \cdot K^{-1}$, depending on desired test conditions. Internal pressure can be applied to the ITV at any desired level between 0 and 200 MPa and at any time during the thermal transient.

The test tank must have a relatively thin wall to minimize thermal stresses resulting from the application of coolant to the hot tank walls. High stresses limit the number of thermal cycles the tank can withstand prior to replacement. Additionally, tolerances in the annular region must initially be, and remain, sufficiently low to maintain uniform heat transfer around the ITV circumference (a condition implicit in analysis of fracture and flaw behavior). The test tank, designed to Section VIII, Division I code requirements, initially consisted of a 7.9-mm-thick wall with ID diametrical tolerances of 1.28 mm and a concentricity tolerance of 0.125 mm. Discussions with fabricators indicated that the combination of thin wall and close tolerances could not be met at a reasonable price and, if it were met, that it could not be maintained after the application of thermally induced stresses. It was therefore necessary to increase the test tank wall to enable achieving and maintaining any degree of ID tolerances.

Major test parameters were analyzed using the OCA-I code to determine their sensitivity to variations in h. Results indicated that for h > 4000 $W \cdot m^{-2} \cdot K^{-1}$ variations in h of ±10% had little effect. Using the modified Sieder-Tate correlation[21] for the flow of coolant through the test tank annulus, h is found to be proportional to flow velocity V and annular gap d as follows:

$$h \propto \frac{V^{0.8}}{d^{0.2}} \quad .$$

For small variations in annular cross section A and with constant pressure, $V \propto 1/A$ so that $h \propto 1/(d^{0.2} \times A^{0.8})$. Using this relationship, it is apparent that variations in annular dimensions of ±1 mm result in a 10 to 11% change in h.

The true situation involving differential changes around the circumference and possible flow perturbations is much more involved and would require three-dimensional analysis. However, the simple analysis in the preceding paragraph serves to set an upper bound on dimensional tolerances. Based on it the test tank concentricity tolerances were increased to 0.5 mm; ID dimensional tolerances remained the same.

The temperature gradient across the test tank wall, caused by the introduction of coolant in the precooling chamber, was calculated as a function of wall thickness and coolant temperature using the HEATING-5 computer program. Resulting thermal stresses were then calculated. Results indicated that secondary thermal stresses could be maintained below a reasonable limit for a vessel wall of 19 mm by cooling the chamber with warm water (~65°C). A wall thickness of 16 mm was considered sufficient to provide adequate support for maintenance of test tank tolerances and provide an additional safety factor. Discussions with potential test tank fabricators confirmed that the increased wall thickness and relaxed tolerance significantly increased the procurement chances. Procurement is being initiated.

5.2.2. <u>HSST test facilities safety criteria</u>

In the initial design and development of the equipment and facilities to test the ITVs in K-702 at the Oak Ridge Gaseous Diffusion Plant (ORGDP) site, C. L. Segaser assessed the potential hazards.[24] This assessment concluded that the HSST cell could withstand missile impact with energy as high as 7.81 x 10^{6} J (5.76 x 10^{6} ft-lb) without perforation of the thinnest (weakest) reinforced concrete wall section. Several conservative assumptions were made:

1. The most potentially damaging missile was considered to be the top head even though the stress state at frangible failure favored smaller missiles.
2. No energy partitioning was assumed. All of the strain energy and fluid stored energy were assumed to be available to propel the critical missile.
3. The fluid stored energy was arbitrarily premised on kerosene, which has a much higher stored energy than the fluid subsequently used (i.e., water).
4. The most conservative of the formulas available at that time for estimating missile penetration was used.

Premised on these assumptions the design of the facility was reviewed and approved by safety personnel at both the Y-12 and ORGDP plants, including the two-plant high-pressure safety committee.

In 1978 the facilities at K-702 were expanded; a reinforced concrete structure adjoining the HSST cell was modified to form a test cell to permit the testing of prestressed concrete reactor vessel (PCRV) models, and a spare intensifier was installed to serve both the HSST and PCRV cells. Safety of the new PCRV cell was premised on the criteria established for the HSST cell and was again approved by ORGDP and Y-12 safety reviews.

With the planning of the testing of ITV V-8A and vessels also under the Pressurized Thermal-Shock Task (PTST) it was evident that the former safety criteria, although quite conservative for the ten tests performed to date in the HSST cell, would be inadequate because of the strong effect of the elevated temperature of these tests on the contained energy.

5.2.3 Missile-containing capability of HSST and PCRV cells for V-8A test and PTS tests

To compensate for the increased heat energy content for intermediate vessel test V-8A and the prospective PTST tests, ballast in the form of graphite segments has been designed and fabricated to fill the test vessels, leaving a 10.4% calculated void volume. Estimates of the compressibility of the pressurizing fluid as a function of temperature were determined by using the energy-volume coefficients derived by Gibson and Loeffler[25] and by using the ASME Steam Tables.[26] Figures 5.28 and 5.29 show the pressure-specific-volume curves for water and ethylene glycol, respectively, for temperatures of 25, 148.7, and 287.8°C. The curves at 148.7 and 287.8°C for water on Fig. 5.28 were extrapolated from ASME Steam Table data by curve fitting as shown.

Figure 5.30 was developed by integrating the area under the curves of Figs. 5.28 and 5.29 considering the pressurization fluid to consist of a mixture of 50% by weight each of ethylene glycol and water.

Estimates of the heat energy available were made by determining the internal energy change for an isentropic process for liquid on the saturation curves corresponding to temperatures of 148.7°C for V-8A and 287.8°C for PTST tests expanding down to atmospheric pressure considering

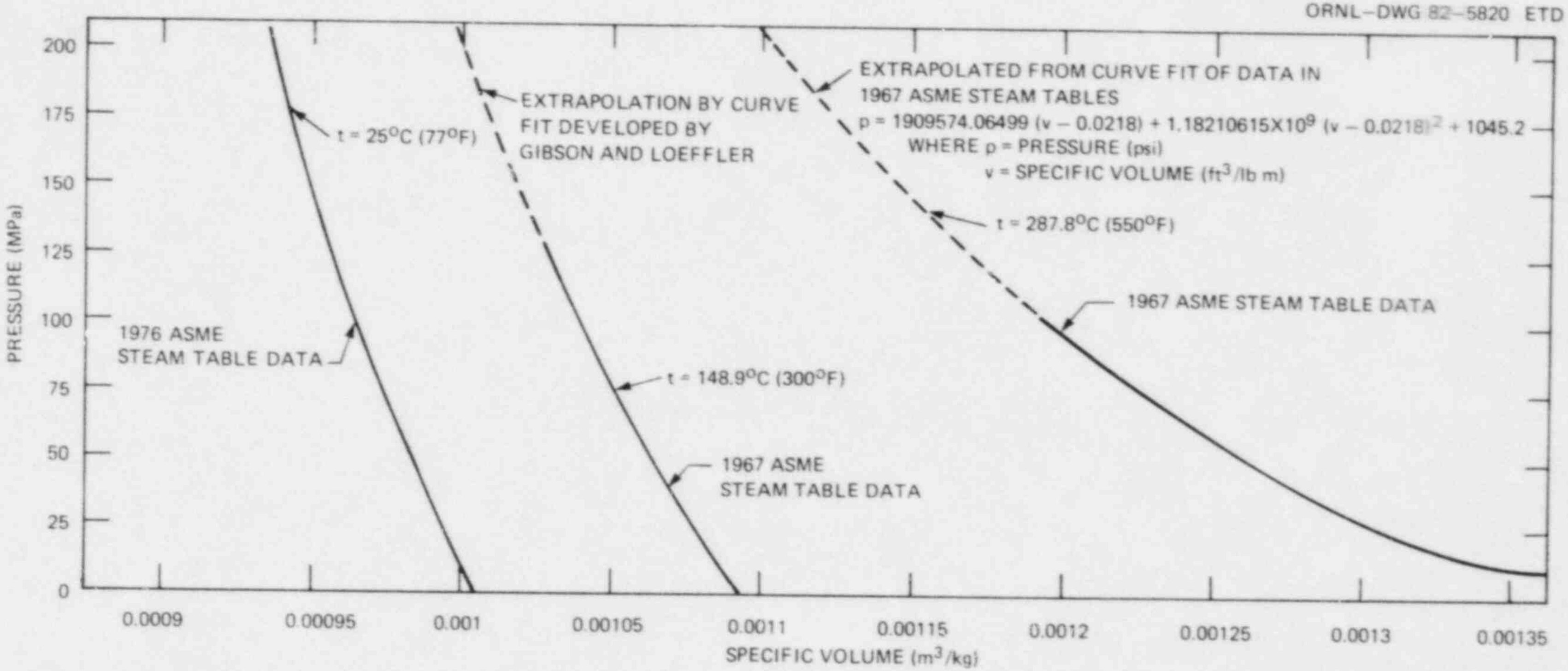

Fig. 5.28. Pressure vs specific volume for water.

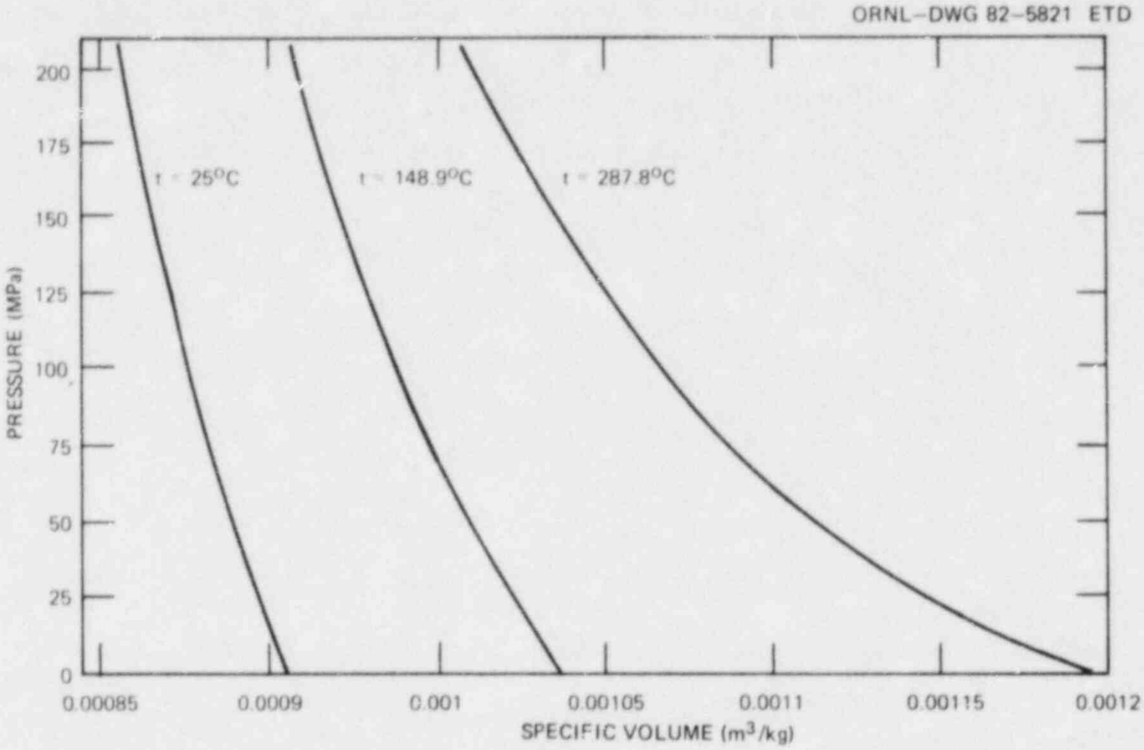

Fig. 5.29. Pressure vs specific volume for ethylene glycol.

the ethylene glycol and water to act independently. Thermodynamic properties for ethylene glycol were premised on the data collection of Curme et al.[27] An efficiency of 50% was considered to be representative of good reciprocating steam engine design[28] and to be a conservative upper bound for missile propulsion, because the fluid following vessel rupture is unconfined.

The total energy potentially available for missile propulsion was considered to be the summation of pressurization energy, heat energy, and strain energy. Strain energy as a function of pressure as calculated by Segaser[24] was used without revision. Figure 5.31 shows the summation of energy as a function of test pressure for the V-8A test, which will be performed at 148.7°C. The total available energy is far below the value of 7.81 x 10^6 J (5.761 x 10^6 ft-lb) calculated by Segaser[24] and validated by Union Carbide Corporation–Nuclear Division (UCC–ND) safety committees. Figure 5.32 correspondingly shows the total energy available at 287.8°C for the PTST tests. Again the total available energy for all test pressures is considerably less than the approved value of 7.81 x 10^6 J.

Validation of HSST and PCRV cell designs for missiles with energies up to 7.81 x 10^6 J as performed by Segaser[24] and as approved by the safety committees incorporated a conservatism not currently required in safety assessments.[29] Namely, no partitioning of energy was originally assumed to occur; contrariwise, although violating dynamics principles all available energy was assumed to be available to a single fragment for missile propulsion. Current UCC–ND safety standards[27] provide rules for the

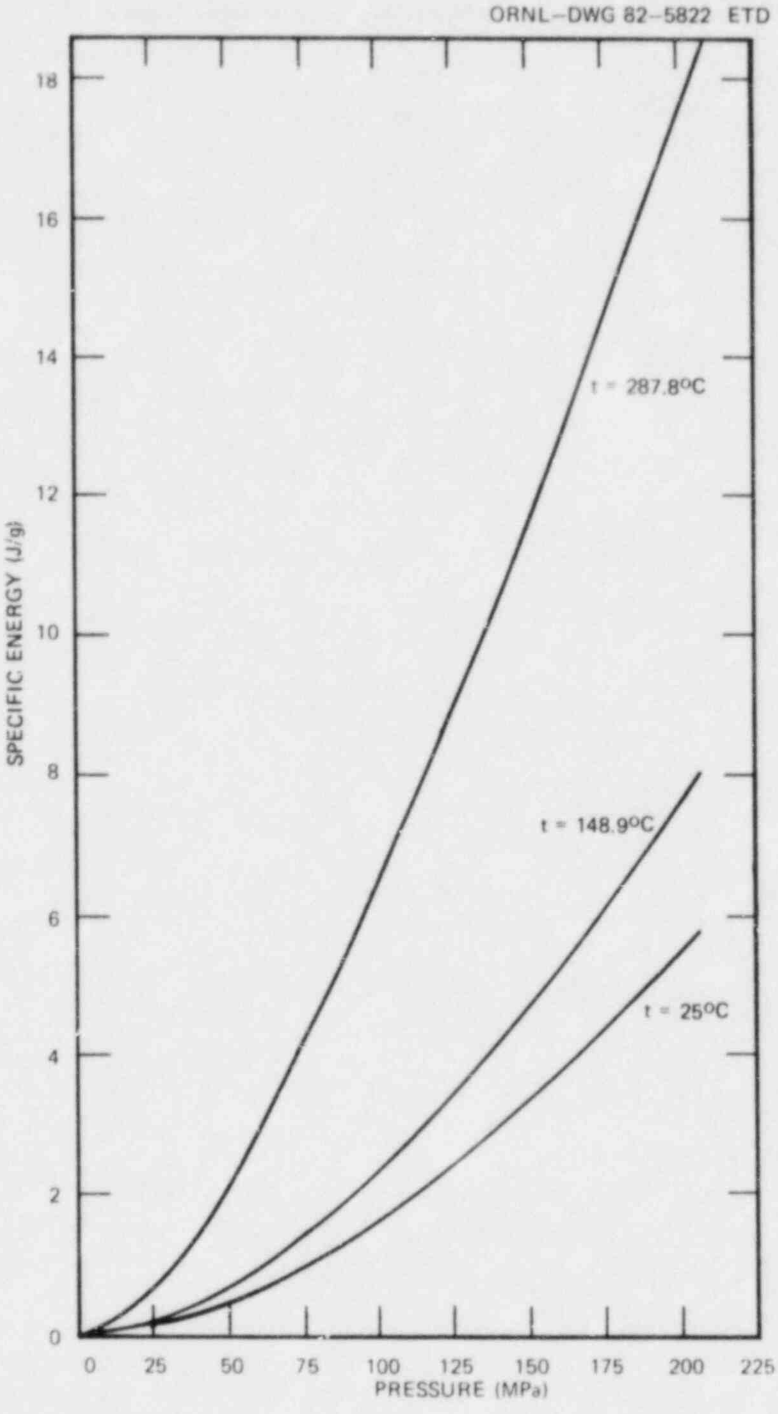

Fig. 5.30. Energy to compress 50% by weight ethylene glycol—water mixture.

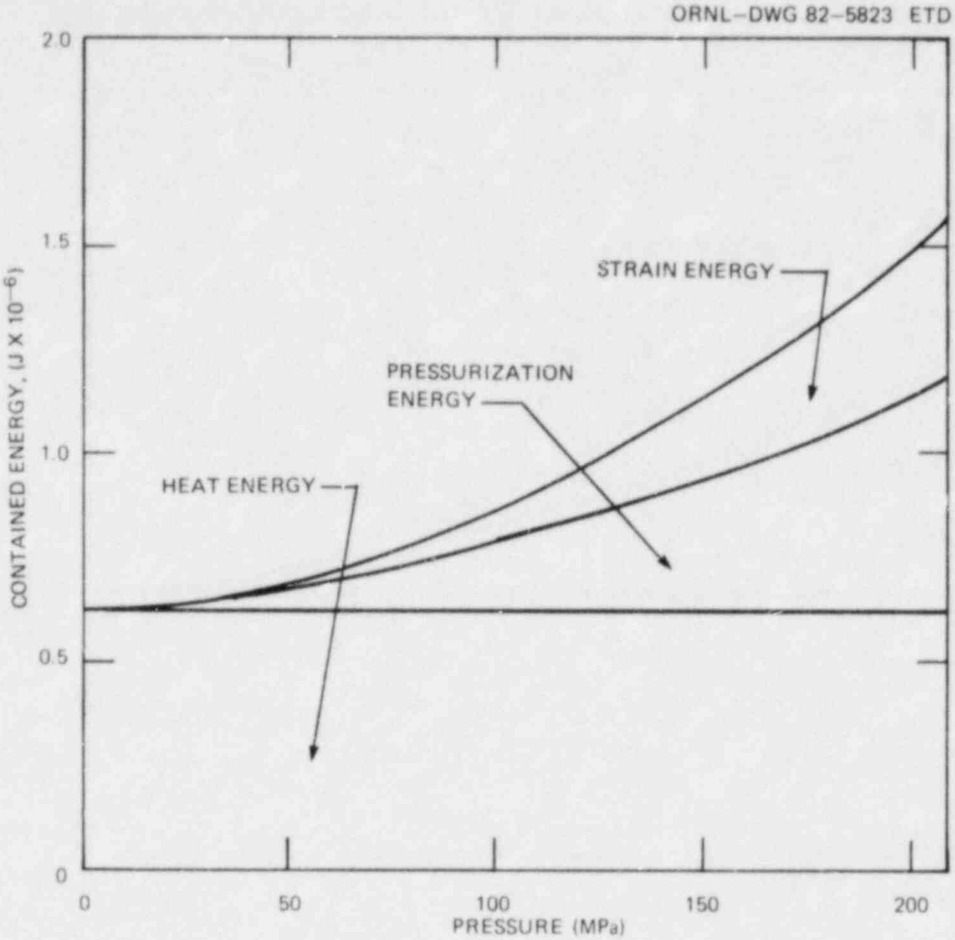

Fig. 5.31. Available energy to produce missiles in intermediate vessel test V-8A.

partitioning of energy to vessel fragments following a vessel rupture. It is concluded that the combination of the various conservatisms employed has provided an ample safety margin for missile resistance of the HSST and PCRV cells as employed for the V-8A test and for PTST tests.

5.2.4 Pressure-containing capability of HSST and PCRV cells as subjected to V-8A and PTS tests

Because of the elevated temperature of the V-8A and prospective PTST tests at 148.7 and 287.8°C, respectively, vessel failure will be accompanied with a considerable release of vapor with consequent pressure loading of the cells. The amount of vapor has been estimated by assuming an isenthalpic expansion of the 50% by weight mixture of ethylene glycol and water down to cell pressure. The fluids were considered to expand independently; thermodynamic properties for ethylene glycol were taken from Curme[27] and for water from the ASME Steam Tables.[28] The vapor released was assumed to fill the cell, and the total pressure was estimated by Dalton's law to be the sum of the partial pressures. Although

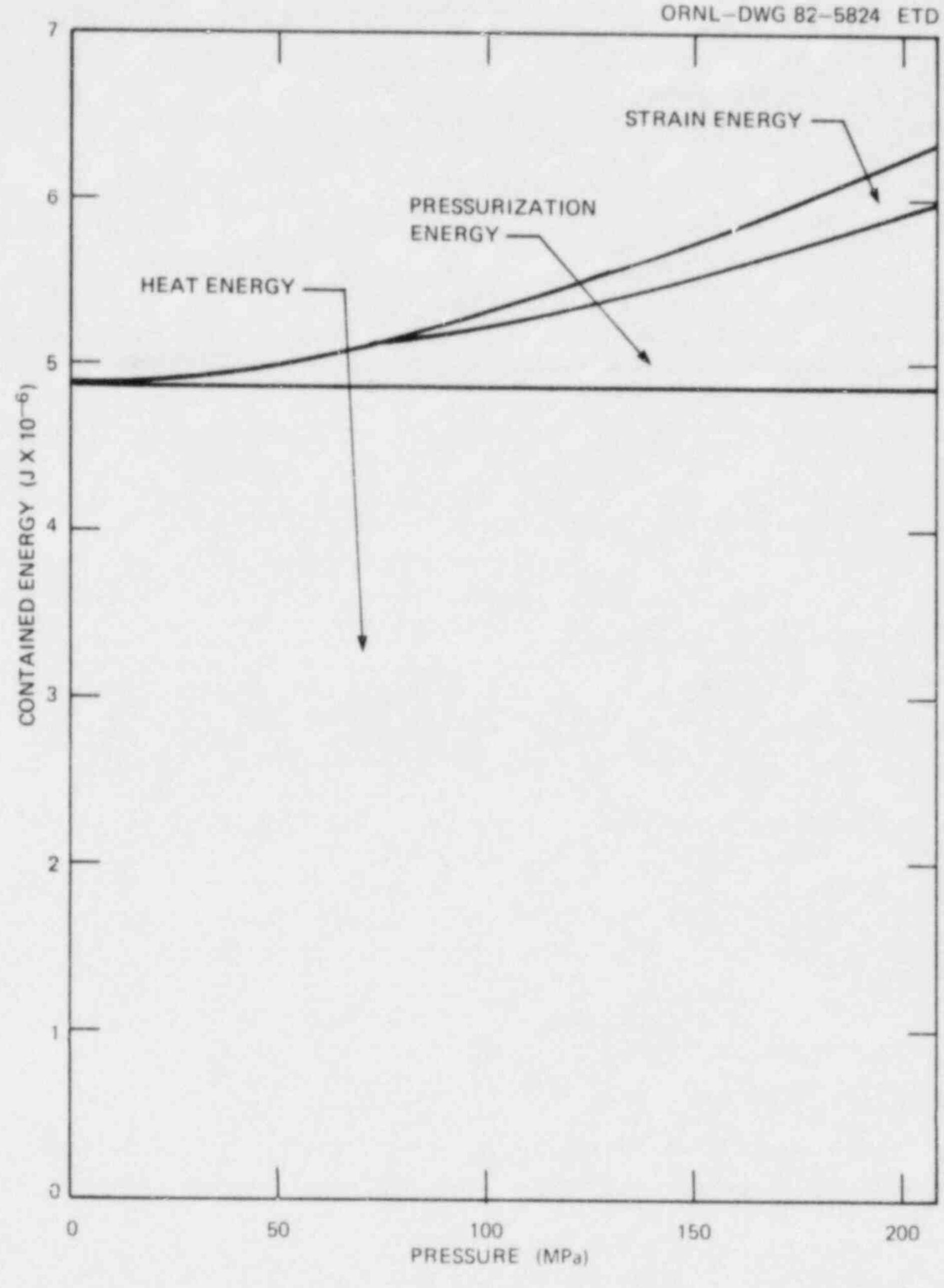

Fig. 5.32. Available energy to produce missiles in pressurized-thermal-shock experiments.

considerable leak paths exist around personnel and chase entries, for conservatism the cells were assumed to be leak tight.

The failure of the V-8A test vessel in the HSST cell under these assumptions results in a calculated wall loading of 13.23 kPa. Similarly, failure of a vessel in the PTST series in the PCRV cell results in calculated wall loading of 46.9 kPa.

The weakest section of the concrete walls of both the HSST and PCRV cells was analyzed by yield line theory.[30] Minimum load to failure was estimated to be 193.1 kPa. The HSST and PCRV cells for pressure loading therefore have a margin of safety exceeding a factor of 4.

REFERENCES

1. H. A. Domian, *Vessel V-8 Repair and Preparation of Low Upper-Shelf Weldment*, The Babcock & Wilcox Company, Alliance, Ohio (January 1982).

2. D. A. Canonico et al., "Investigation of Irradiated Materials," *Heavy-Section Steel Technology Program Quart. Prog. Rep. April–June 1980*, NUREG/CR-1627 (ORNL/NUREG/TM-401).

3. R. Johnson, *Resolution of the Reactor Vessel Materials Toughness Safety Issue*, U.S. Nuclear Regulatory Commission, NUREG-0744, Vol. 1 (September 1981).

4. *U.S. Code of Federal Regulations, Title 10, Energy, Part 50*, "Domestic Licensing of Production and Utilization Facilities."

5. C. E. Childress, *Fabrication and Mechanical Test Data for Four 6-in.-thick Intermediate Test Vessels Made from Steel Plate for the Heavy-Section Steel Technology Program*, ORNL/TM-5074 (January 1976).

6. R. H. Bryan et al., *Test of 6-in.-Thick Pressure Vessels, Series 3: Intermediate Test Vessel V-8*, ORNL/NUREG-58 (December 1979).

7. P. P. Holz and R. H. Bryan, "Intermediate Test Vessel V-8A," *Heavy-Section Steel Technology Program Quart. Prog. Rep. January–March 1981*, NUREG/CR-2141/V1 (ORNL/TM-7822).

8. P. P. Holz and R. H. Bryan, "Intermediate Test Vessel V-8A," *Heavy-Section Steel Technology Program Quart. Prog. Rep. April–June 1981*, NUREG/CR-2141, Vol. 2 (ORNL/TM-7955).

9. P. P. Holz and R. H. Bryan, "Intermediate Test Vessel V-8A," *Heavy-Section Steel Technology Program Quart. Prog. Rep. July–September 1981*, NUREG/CR-2141, Vol. 3 (ORNL/TM-8145).

10. R. H. Bryan, "ITV V-8A," *Heavy-Section Steel Technology Program Quart. Prog. Rep. October–December 1981*, NUREG/CR-2141, Vol. 4 (ORNL/TM-8252).

11. R. H. Bryan et al., *Test of 6-Inch-Thick Pressure Vessels, Series 2: Intermediate Test Vessels V-3, V-4, and V-6*, ORNL-5059 (November 1975).

12. R. H. Bryan et al., *Test of 6-in.-thick Pressure Vessels, Series 3: Intermediate Test Vessel V-7B*, NUREG/CR-0309 (ORNL/NUREG-38) (October 1978).

13. J. G. Merkle, "Explanation of Analytical Bases for Low Upper Shelf Vessel Toughness Evaluations," *Resolution of the Reactor Vessel Materials Toughness Safety Issue*, U.S. Nuclear Regulatory Commission, NUREG-0744, Vol. 2, Appendix C (September 1981).

14. J. G. Merkle, "Stress Intensity Factor Estimates for Part-Through Surface Cracks in Plates Under Combined Tension and Bending," *Quart. Prog. Rep. on Reactor Safety Programs Sponsored by the Division of Reactor Safety Research for July–September 1974*, ORNL-TM-4729, Vol. II.

15. F. W. Smith and M. J. Alavi, "Stress-Intensity Factors for a Part-Circular Surface Flaw," pp. 793–800 in Part III, *Proceedings of the First International Conference on Pressure Vessel Technology, Delft, The Netherlands*, ASME, New York, 1969.

16. C. F. Shih et al., *Methodology for Plastic Fracture, Fifth Quarterly Report, May 1, 1977 to August 31, 1977*, General Electric Company, Schenectady, NY (November 1, 1977).

17. W. J. Stelzman and R. K. Nanstad, "Prolongation V-10P Studies," *Heavy-Section Steel Technology Program Quart. Prog. Rep. October–December 1981*, NUREG/CR-2141, Vol. 4 (ORNL/TM-8252).

18. R. H. Bryan, "Fracture Analysis," *Heavy-Section Steel Technology Program Quart. Prog. Rep. October–December 1981*, NUREG/CR-2141, Vol. 4 (ORNL/TM-8252).

19. J. W. Bryson and B. R. Bass, "Computer Program Development," *Heavy-Section Steel Technology Program Quart. Prog. Rep. April–June 1981*, NUREG/CR-2141, Vol. 2 (ORNL/TM-7955).

20. P. P. Holz, "Flawing Practice," *Heavy-Section Steel Technology Program Quart. Prog. Rep. October–December 1981*, NUREG/CR-2141, Vol. 4 (ORNL/TM-8252).

21. G. C. Robinson, "Pressurized Thermal Shock," *Heavy-Section Steel Technology Program Quart. Prog. Rep. April–June, 1981*, NUREG/CR-2141, Vol. 2 (ORNL/TM-7955).

22. G. C. Robinson et al., "Pressurized Thermal-Shock Test Studies," *Heavy-Section Steel Technology Program Quart. Prog. Rep. July–September 1981*, NUREG/CR-2141, Vol. 3 (ORNL/TM-8145).

23. R. H. Bryan et al., "PTS Test Studies," *Heavy-Section Steel Technology Program Quart. Prog. Rep. October–December 1981*, NUREG/CR-2141, Vol. 4 (ORNL/TM-8252).

24. C. L. Segaser, *System Design Description of the Intermediate Vessel Tests for the Heavy-Section Steel Technology Program*, ORNL-TM-2849, (Revised July 1973).

25. R. E. Gibson and O. H. Loeffler, "Pressure-Volume-Temperature Relations In Solution. V. The Energy-Volume Coefficients of Carbon Tetrachloride, Water and Ethylene Glycol," *J. Am. Chem. Soc.* 64, 898–906 (April 1941).

26. C. A. Meyer et al., "Thermodynamic and Transport Properties of Steam," *ASME Steam Tables, 4th ed., The American Society of Mechanical Engineering*, New York, 1979.

27. George O. Curme (Ed.), *Glycols*, Reinhold Publishing Co., New York, New York, 1952.

28. R. T. Kent, *Kent's Mechanical Engineering Handbook*, 11th Edition, Table 7, pp. 7–26, John Wiley & Sons, New York, New York, 1945.

29. The Ad Hoc Committee for High Pressure Safety, *Safety Standards for High Pressure System Facilities*, Union Carbide Corporation for DOE, Y/GA-23, April 1981.

30. George Winter et al., *Design of Concrete Structures*, 7th ed., p. 239, McGraw-Hill, New York, 1964.

6. STAINLESS STEEL CLADDING INVESTIGATIONS

6.1 Task Planning

G. C. Robinson P. P. Holz
J. G. Merkle

The overriding objective of obtaining substantive data on the interaction of stainless cladding with propagating base-metal flaws as early as possible in 1983 has required simultaneous parallel implementation of several interdependent activities, including the following:

1. development of welding procedures to produce stainless cladding representative of that produced by commercial shops;
2. development of welding and heat-treating procedures to produce stainless cladding with degraded toughness to simulate the potential effect of radiation;
3. development of flawing procedures using the electron-beam-welding/hydrogen-charging techniques to produce surface and buried flaws in specimens having no cladding, representative commercial cladding, or degraded cladding;
4. planning of test matrix and requisite materials characterization utilizing HSST Plate 07B, a plate conforming to ASTM A5333 grade B class 1 requirements having dimensions of 254-mm thickness by 2.42-m length by 0.933-m width; and
5. design of loading components or modification of an existing testing machine to permit four-point constant moment loading of the wide plate specimens and design of heat transfer and hydrogen-charging equipment.

Specimen dimensions were reduced from those previously reported[1] to permit expeditious usage of HSST Plate 07B, thereby increasing the number of specimens and test parameters, and to reduce fabrication and testing time of the specimens. Current nominal specimen dimensions are 50.8-mm thickness by 406.4-mm width by 914.4-mm length. To achieve the same stress state with the smaller specimen required the use of a higher capacity loading machine, a 0.98-MN Instron servo-hydraulic testing machine located in the Metals and Ceramics Division Mechanical Testing Laboratory. Table 6.1 shows the cladding and flaw dimensions and cladding parameters projected for 14 specimens to be taken from HSST Plate 07B. Figure 6.1 shows the relative location of the specimens, CP-1 through CP-14, and plate section "F" for the characterization of the material. Figure 6.2 shows a section elevation of a typical specimen housed within the loading components of the Instron testing machine.

The loading components for the Instron testing machine (Fig. 6.2) have been designed, are being fabricated by a lump sum contractor, and are scheduled for delivery the first week of April. Sectioning of HSST Plate 07B and slabbing to form two-specimen-thick slabs for welding on each side of the slab has been accomplished. Stainless clad test coupons are being electron-beam-weld flawed and hydrogen-charged over a range of temperatures from 20 to −15.6°C to establish flaw parameters. Difficulty has

Table 6.1. Clad plate task specimen test matrix

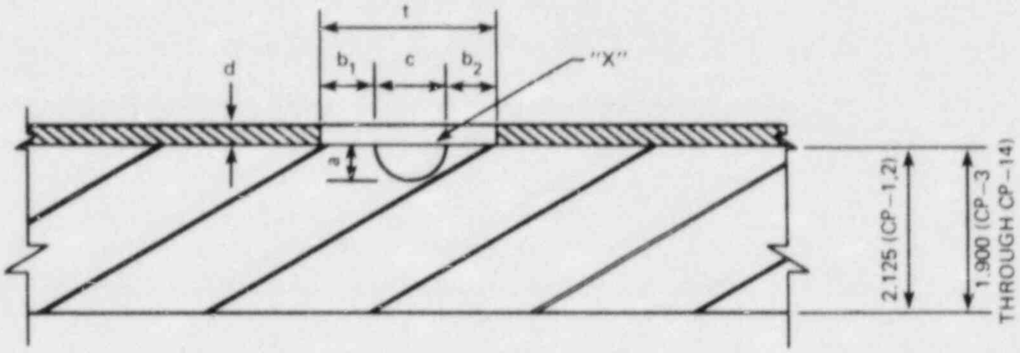

Specimen No.	Specimen clad		"x" Cladding over flaw		Sigma-phase treatment		Dimensions (cm)						Dimensions "as built"	
	Yes	No	Yes	No	Yes	No	a	b_1	b_2	c	d	t	Yes	No
CP-1A		X		X		X	1.40			7.62			X	
CP-2		X		X		X	1.02			7.62			X	
CP-4	X			X		X	1.40	0.64	0.64	9.53	0.40	10.81	X	
CP-5	X			X		X	1.14	0	0.16	9.21	0.40	9.37	X	
CP-3	X			X		X	1.27	1.27	1.27	7.62	0.56	10.16		X
CP-6	X			X		X	1.02	0	0	7.62	0.56	7.62		X
CP-7	X			X	X		1.27	1.27	1.27	7.62	0.40	10.16		X
CP-8	X		X			X	1.27	0	0	7.62	0.40			X
CP-9	X			X		X	1.27	2.54	2.54	7.62	0.40	12.70		X
CP-10	X				X		1.02	0.64	0.64	7.62	0.40	8.90		X
CP-11	X			X		X	1.27	1.27	1.27	7.62	0.40	10.16		X
CP-12	X		X		X		1.02	0	0	7.62	0.40			X
CP-13	X			X		X	1.27	2.54	2.54	7.62	0.40	12.70		X
CP-14	X				X		1.02	0	0	7.62	0.40	7.62		X

been experienced with hydrogen-charging of flaws that have been prepared by machining to the nominal base-metal/clad interface prior to welding, apparently because of contamination of residual stainless material at the uneven interface. Undercutting of the base metal by 0.08 mm has given favorable results on several test coupons. Two dummy specimens, fabricated from ASTM A572 grade 70 material, designated as PVT-D1 and PVT-D2, have been machined and flawed. These dummy specimens will be used to validate the loading, cooling, and hydrogen-charging procedures.

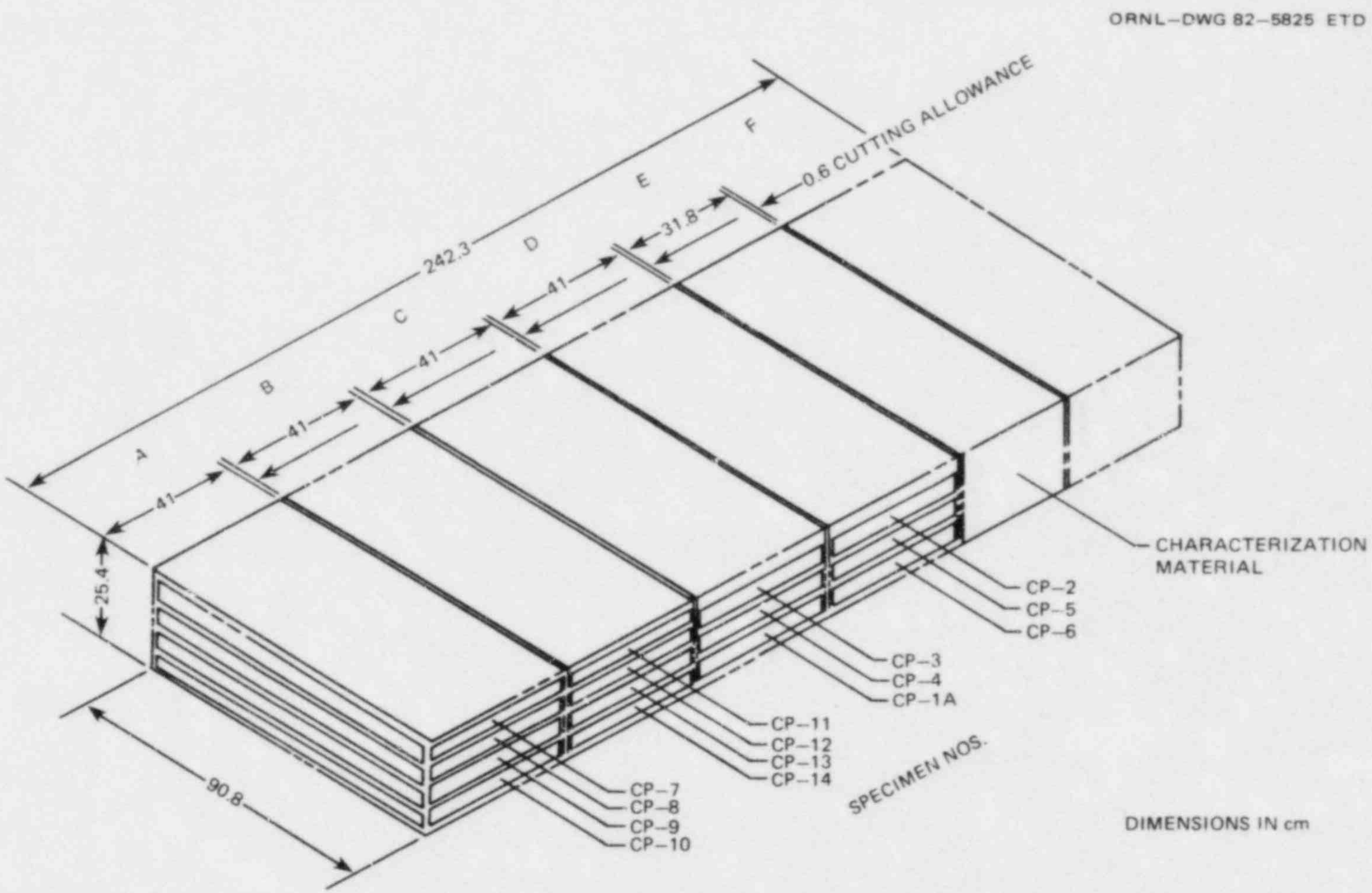

Fig. 6.1. Cutup of HSST plate 07B for clad plate specimens and characterization material.

ORNL-DWG 82-5826 ETD

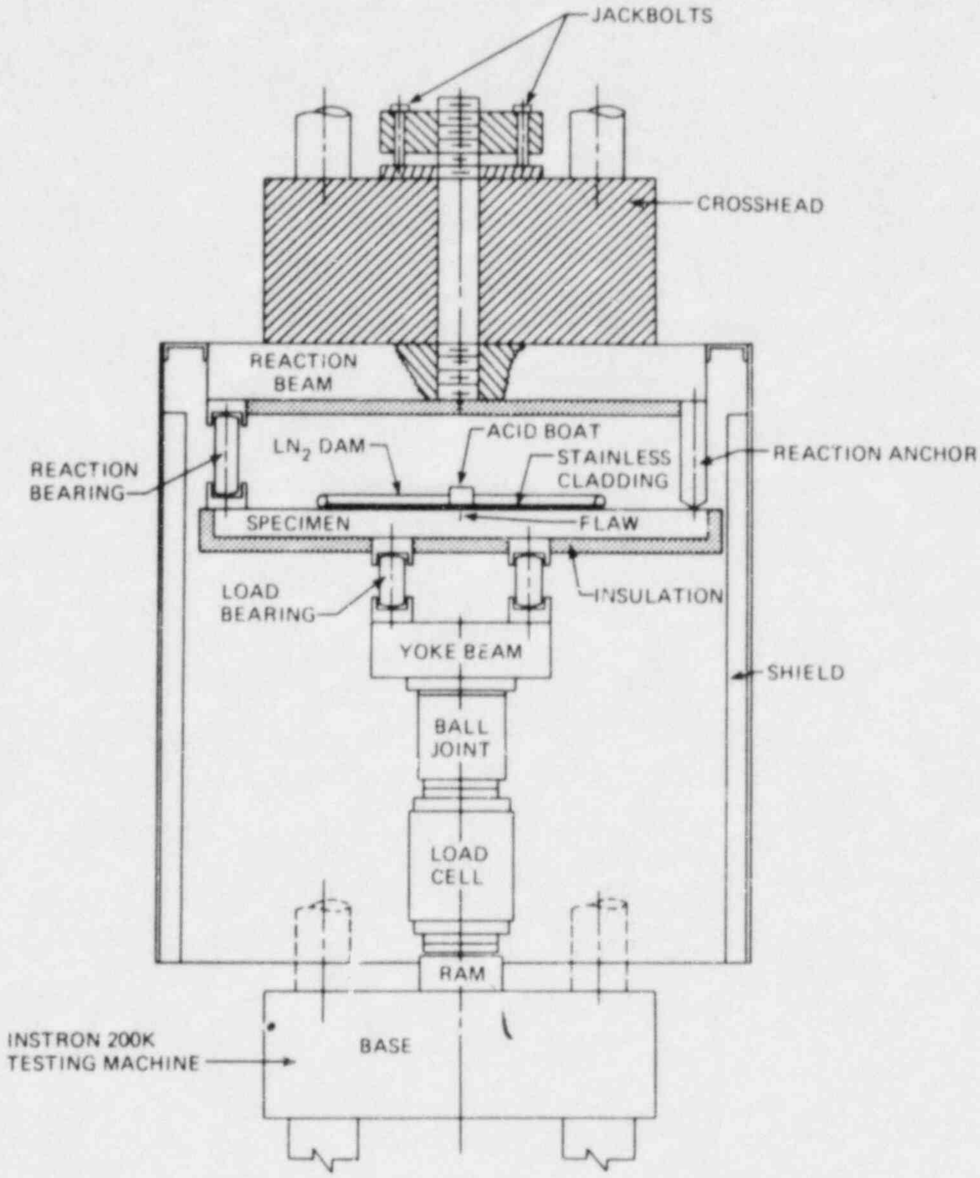

Fig. 6.2. Section elevation of clad plate task test setup.

6.2 Weld Cladding and Material Characterization

R. K. Nanstad   R. G. Berggren
W. J. Stelzman   J. F. King
G. M. Goodwin

Cladding operations have been planned and conducted with a view toward a reasonable representation of cladding in older operating commercial reactor pressure vessels. Contacts made with knowledgeable people within the NRC and industry indicated that a wide variety of cladding procedures, such as three-wire, six-wire, two-wire with cold feed, strip clad, etc., have been used for application of weld cladding to nuclear pressure vessels. Automatic submerged-arc welding equipment in the Welding and Brazing Laboratory at ORNL is being utilized to apply stainless steel cladding by a single-wire oscillating process. Stainless steel types 309 and 308 weld wires (5/32-in. diameter) were procured to represent cladding as applied in the field. Stainless steel type 312 was procured to provide a means of representing the embrittled cladding that may exist in operating reactors following extended neutron irradiation. Sandvik WF34 flux is being used in both cases.

To minimize distortion and provide a suitable heat sink during cladding, plates at least 4-1/2 in. thick, 16 in. wide, and 36 in. long are being used. The 308/309 cladding is applied on plate surfaces representing material far from the original plate surfaces, while the 312 cladding is applied on original plate surfaces. The objective of this procedure is to maximize the number of test specimens for cladding evaluation. To eliminate the gradient in properties near the original plate surface, the specimens clad with type 312 will be heat-treated at 849°C and air-cooled to reaustenitize the plate material as well as to transform some of the ferrite in the type 312 to the brittle sigma phase. The test specimens clad with 308/309 are given a postweld heat treatment (PWHT) at 621°C for 40 h to represent commercial practice.

The single-wire oscillating submerged-arc welding process being used involves a preheat temperature of 121°C and an interpass temperature below 288°C. Practice plates were utilized to optimize the welding parameters with the following results:

1. wire extension, 27.0 mm (1-1/16 in.);
2. oscillation width, 19.0 mm (3/4 in.);
3. frequency, 0.3 Hz (18 cpm);
4. dc amps, 500;
5. dc volts, 36; and
6. travel speed, 2.1 mm/s (5 in./min).

For the 308/309 case, a layer of type 309 is applied to the plate, followed by a layer of type 308. For the 312 case, two layers of type 312 are applied. Plates for material characterization have been prepared as well so that mechanical properties can be determined for the base plates and the stainless steel cladding. For those plates, weld metal was applied in three layers to provide sufficient clad thickness for removal of up to 1/2-in.-thick compact specimens (1/2 T CS). A test specimen matrix has been prepared for both plate and weld metal. Test specimens for plate characterization include Charpy V-notch impact, tensile, precracked Charpy, 1T CS, 2T CS, drop-weight, and crack arrest. Properties will be determined for both the longitudinal and through-thickness orientations in the plate. Heat-affected zone (HAZ) and weld metal will be characterized with tensile, Charpy V-notch, precracked Charpy, and 1/2T CS.

To accommodate the welding and heat-treating of the large plates, a special portable fixture (Fig. 6.3) was constructed that holds the plates under the welding head and allows for relatively easy turning of the plate so that layers can be applied alternately to both surfaces to minimize

M&C PHOTO–184479A

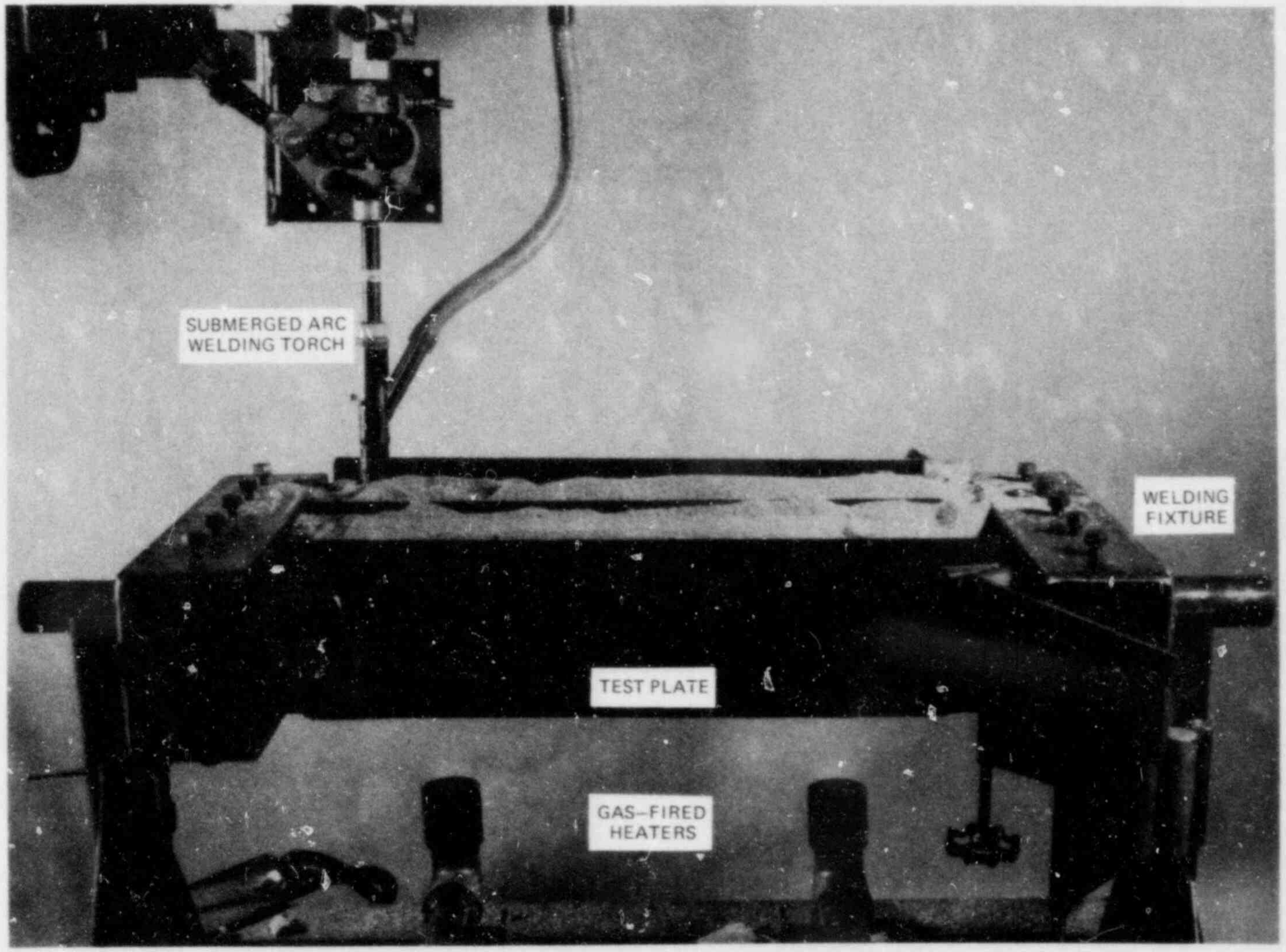

Fig. 6.3. Portable fixture for submerged-arc weld cladding.

distortion. The fixture also incorporates removable gas burners for preheating. Additionally, the side-beam carriage of the welding machine was modified to accommodate two coils of weld wire so that 308/309 and 312 layers can be applied alternately without the cumbersome and time-consuming changing of coils. The floor of the heat-treating furnace was reinforced, and lifting devices were modified to handle the large plates. One test plate each with 308/309 and 312 have been clad and heat-treated, while one characterization plate with each clad type has also been welded and heat-treated.

Reference

1. G. C. Robinson and J. G. Merkle, "Scoping Studies," *Heavy-Section Steel Technology Program Quart. Prog. Rep. October–December 1981*, NUREG/CR-2141, Vol. 4 (ORNL/TM-8252), p. 118.

CONVERSION FACTORS[a]

SI unit	English unit	Factor
mm	in.	0.0393701
cm	in.	0.393701
m	ft	3.28084
m/s	ft/s	3.28084
kN	lb_f	224.809
kPa	psi	0.145038
MPa	ksi	0.145038
$MPa \cdot \sqrt{m}$	ksi $\sqrt{in.}$	0.910048
J	ft-lb	0.737562
K	°F or °R	1.8
kJ/m^2	in.-lb/in.^{2}	5.71015
$W \cdot m^{-2} \cdot K^{-1}$	Btu/h-ft^2-°F	0.176110
kg	lb	2.20462
kg/m^3	lb/in.^{3}	3.61273×10^{-5}
mm/N	in./lb_f	0.175127
T(°F) = 1.8 T(°C) + 32		

[a]Multiply SI quantity by given factor to obtain English quantity.

NUREG/CR-2751
Volume 1
ORNL/TM-8369/V1
Dist. Category RF

Internal Distribution

1. B. R. Bass
2. R. G. Berggren
3. S. E. Bolt
4-8. R. H. Bryan
9. J. W. Bryson
10. R. D. Cheverton
11. J. M. Corum
12. W. R. Corwin
13. J. R. Dougan
14. R. C. Gwaltney
15. P. P. Holz
16. S. K. Iskander
17. K. K. Klindt
18. Yung-Lo Lin
19. A. L. Lotts
20. S. S. Manson
21. R. W. McCulloch
22. J. G. Merkle
23. R. K. Nanstad
24. D. J. Naus
25. G. C. Robinson
26-27. T. W. Robinson, Jr.
28. G. M. Slaughter
29. W. J. Stelzman
30. H. E. Trammell
31. J. D. White
32-36. G. D. Whitman
37. ORNL Patent Office
38. Central Research Library
39. Document Reference Section
40-41. Laboratory Records Department
42. Laboratory Records (RC)

External Distribution

43. C. Z. Serpan, Division of Engineering Technology, Nuclear Regulatory Commission, Washington, DC 20555
44. M. Vagins, Division of Engineering Technology, Nuclear Regulatory Commission, Washington, DC 20555
45. Office of Assistant Manager for Energy Research and Development, DOE, ORO, Oak Ridge, TN 37830
46-47. Technical Information Center, DOE, Oak Ridge, TN 37830
48-337. Given distribution as shown in category RF (NTIS – 10)

©U.S. GOVERNMENT PRINTING OFFICE: 1982-546-067/109

120555078877 1 ANRF
US NRC
ADM DIV OF TIDC
POLICY & PUBLICATIONS MGT BR
PDR NUREG COPY
LA 212
WASHINGTON DC 20555